Automatic Distributed Load Temperature Control Strategies for a Rectified Continuous Flow Loop Interfaced with a Regenerative Cryocooler

by

Harrison M. Skye

A thesis submitted in partial fulfillment of the requirements for the degree of

Master of Science

(Mechanical Engineering)

at the

UNIVERSITY OF WISCONSIN-MADISON

2007

Approved:

Professor Greg Nellis
Department of Mechanical Engineering
University of Wisconsin – Madison

Professor Sanford Klein
Department of Mechanical Engineering
University of Wisconsin - Madison

Automatic Distributed Load Temperature Control Strategies for A Rectified Continuous Flow Loop Interfaced with a Regenerative Cryocooler

Harrison M. Skye

Under the supervision of Professors Greg Nellis and Sanford Klein
and the University of Wisconsin - Madison

Abstract

Distributed loads are frequently encountered in large deployable structures used in space applications such as optical mirrors, actively cooled sunshades, and on focal plane electronics. One mechanism for providing distributed cooling is via an oscillatory cryocooler such as a pulse-tube that is integrated with a fluid rectification system consisting of check-valves and buffer volumes in order to extract a small amount of continuous flow. This continuous flow allows relatively large loads to be accepted over a long distance with a small temperature difference and has advantages relative to vibration and electrical isolation. Also, it is possible to provide rapid and precise temperature control via modulation of the flow rate. The same working fluid, helium, can be used throughout the entire system, reducing complexity and simplifying the contamination control process.

This thesis discusses an experimental setup that is used to demonstrate this concept; steady state and uncontrolled transient behavior is characterized and used to create a non-linear empirically based thermal model of the system. Further, the ability of the rectifying interface to precisely control the temperature of a distributed load under dynamically changing conditions is investigated both analytically and experimentally. Precise and rapid temperature regulation is enabled by applying temperature feedback control to a throttle valve that is placed in the

distribution loop. Flow modulation using the throttle valve is governed by a Proportional-Integral (PI) controller with gains that are selected to meet design temperature control criteria; specifically, maximum temperature fluctuation and settling time for a step change in distributed load. A linearized thermal model, based on a non-linear empirical model, allows the use of linear control theory to develop the controller algorithm. Agreement between the modeled and experimental controlled temperature behavior validates the use of the linear model for selecting the controller gains.

Acknowledgements

I would like to give thanks to:

My advisors, professors Klein and Nellis for their continual support and guidance in research and coursework. It has been a pleasure to work with these two professors; I look forward to continue working with them during my PhD work. I've enjoyed the time spend with my colleagues in the SEL, particularly, my office mates Ryan Taylor, Kurt Englebrecht, Steve Meitner, and Mike White. Thanks to my family, Dad, Mom, Weston, and Jenny for their encouragement in my work and always providing a place to call home. Special thanks to my future wife Naomi, for her patience, support, and ability to give me something to talk about besides engineering. Special thanks also to John Dyreby, for being a great friend, roommate, and somehow always leading a life oddly parallel to my own.

Thanks to Steve Meitner and Dan Hoch for sharing their expertise in the lab.

Support from the WSGC for this research is gratefully acknowledged.

Table of Contents

Abstract ..... **i**

Acknowledgements ..... **iii**

Table of Contents ..... **iv**

List of Figures ..... **vii**

List of Tables ..... **xi**

List of Variables ..... **xii**

1 Introduction **1**

1.1 Future Goals of NASA Space Program 1
1.1.1 Single Aperture Far-Infrared (SAFIR) Telescope 2

1.2 Description of Application and Current Methodologies 4
1.2.1 Current Methodology 1 - Conductive Strap 5
1.2.2 Current Methodology 2 - Capillary and Mechanical Pumped Loop 5

1.3 Pulse Tube Rectified Interface Concept 6

1.4 Thesis Outline 8

1.5 References 10

2 Experimental Setup – Pulse Tube Rectifying Interface, Automatic Control Hardware, and Data Acquisition **11**

2.1 Pulse Tube Rectifying Interface 11

2.2 Motorized Cooling Loop Flow Control Valve 15

2.3 LabVIEW Data Acquisition and Control Program 20

2.4 Signal Conditioning 21

2.5 Automatic Control Hardware 22

2.6 Computer controlled heater circuit 25

2.7 References 28

3 Experimental Data - Steady State and Uncontrolled Transient Behavior **29**

3.1 Cool Down Curve 29

3.2 Calculation of Stroke 30

3.3 Steady State Data – Cooling Loop Valve Closed 31

3.4 Steady State Data – Cooling Loop Valve Open 33

3.5 Transient Data 36

3.6 Calculation of Mass Flow Rate and Parasitic Loss 42

3.7 Dimensionless Interface Valve Resistance 44

4 Steady State and Transient PT\RI Thermal Model: Development and Verification ... 48

4.1 Governing Equations for Transient PT/RI Model 49

4.2 Parasitic Heat, Mass Flow, and Refrigeration Power Empirical Models 52

4.3 Comparison of Transient Model Steady State Load Curves and Experimental Data Steady State Load Curves 60

4.4 Comparison of Experimentally Measured and Predicted Transient Response 61

4.5 References 65

5 Operating Point Linear PT/RI Thermal Model Development and Verification 66

5.1 Interface and Cold Head Operating Point Thermal Models 66

5.2 Pulse Tube Refrigeration and Mass Flow Operating Point Models 69

5.3 State Block Diagram of Complete Operating Point PT/RI Thermal Model and Discussion of Time Constants 71

6 Automatic Temperature Control Law Development 74

6.1 Simplified Operating Point PT/RI Thermal Model 74

6.2 Analog Temperature Control Algorithm Development 79

6.2.1 Interface temperature control 80

6.2.2 Cold head temperature control 89

6.3 Interface digital model development and comparison with analog model 92

6.4 Interface settling time selection 96

6.5 References 100

7 Comparison of Modeled and Experimental Controlled Temperature Response 101

7.1 Uncontrolled and Baseline Control Experimental Results 102

7.2 Full Control Experimental Results 105

7.3 Comparison of Experimental Results 106

7.4 Comparison of Predicted and Experimentally Measured Controlled Temperature Response 113

7.5 References 115

8 Conclusions 116

8.1 Experimental Verification of Pulse Tube Rectified Interface Concept 116

8.2 Controller Design Process 117

8.3 Future Recommendations 119
8.4 References 121

Appendix A – Mass Flow Data Point Omission 122

Appendix B - Matlab Script for Digital and Analog Simplified Linear Interface Model .. 124

List of Figures

Figure 1-1: Conceptual image of the SAFIR telescope, planned for launch in 2015-2020 3

Figure 1-2: Temperature and wavelength dependence of IR detector sensitivity for the SAFIR telescope. ...4

Figure 1-3: Schematic of a single-stage, Stirling-type pulse-tube integrated with multiple, distributed loads using a rectifying interface.....7

Figure 2-1: Schematic of the PT/RI experimental apparatus showing the location of key measurements of pressure and temperature.....12

Figure 2-2: (a) Schematic of the reed-type check-valves that are used within the rectifying interface and (b) photographs of the reed sub-component during the development process showing the improvement in the fabrication process. 12

Figure 2-3: Differential pressure transducer (P4) used to infer the compressor stroke.....14

Figure 2-4: Photograph of the components within the vacuum vessel (flow control valve not shown).....15

Figure 2-5: (a) top view and (b) side view of: the motorized cooling loop valve setup highlighting the shaft coupling which accommodates the axial translation of the valve stem while providing a torque linkage from the motor to the valve. 17

Figure 2-6: Detailed schematic of the motorized valve assembly shown in inches. In this figure, the gap between the coupling key and the coupling (0.36 in.) represents the gap when the valve is completely closed. The gap when the valve is fully open is approximately 0.11 in. Figure 2-7 shows the detailed sections (a) and (b). 18

Figure 2-7: Detailed sections (all measurements in inches) of the motorized valve assembly. (a) Components inside the bell jar including the cooling loop valve step. (b) Components outside the bell jar including the coupling, coupling key and motor connection. 18

Figure 2-8: Coupling for motorized valve shaft assembly which allows axial motion and provides torsional support for valve stem rotation: (a) side view of schematic, (b) side view of fabricated coupling assembly, and (c) front view of fabricated coupling assembly.....19

Figure 2-9: Detailed schematics of several of the motorized valve assembly including: (a) coupling key, (b) valve stem, and (c) coupling.....20

Figure 2-10: Conceptual diagram of Labview VI used to acquire the system data and implement the temperature control algorithms 21

Figure 2-11: LabVIEW implantation of digital Infinite Impulse Response (IIR) temperature signal filtering….. 22

Figure 2-12: Distributed load temperature feedback control hardware and software components. 24

Figure 2-13: Cold head temperature feedback control hardware and software components. 24

Figure 2-14: Motor controlled variac output voltage vs. input 0-3.5 DCV.....25

Figure 2-15: Picture of the motor controlled variac. The variac outputs 0-115 VAC to the compressor based on a 0-3.5 VDC command from the LabVIEW VI. 25

Figure 2-16: Op-amp schematic for providing computer controlled dissipative heat load.....26

Figure 2-17: Calculated power supplied to the resistance heater vs. input voltage for the op-amp power supply circuit.....27

Figure 3-1: Typical cool down from room temperature for the PT/RI system. The components in the loop are at nearly the same temperature during the cool down process.....30

Figure 3-2: Compressor backside pressure measured as a function of time at 80% and 100% stroke (valve ¼ open, 5.0 W distributed load).....31

Figure 3-3: Load curve measured for the PT/RI system with the flow control valve closed and 80% and 100% stroke. 32

Figure 3-4: Pressure waveforms in the pulse tube and high and low pressure buffer volumes for three different valve settings: ½ open, ¼ open, and closed. 34

Figure 3-5: Load curves for the PTRI system with heat applied at the cold head. Three valve settings (¼ open, ½ open, and closed) are compared at (a) 80% stroke and (b) 100% stroke.....35

Figure 3-6: Load curves for the interface heater comparing settings of stroke (80% and 100%) and valve setting (½ open and ¼ open). 36

Figure 3-7: Transient temperature data for a step change in stroke from 80% to 100% (interface valve= ¼ open, interface heat = 2.64 W) in terms of (a) time and (b) cold head dimensionless time 38

Figure 3-8: Transient response of PT/RI system to a step change in interface load from 7.95 W to 2.32 W (stroke = 100%, valve = ¼ open) in terms of (a) time, (b1) interface dimensionless time (first 150s), and (b2) cold head dimensionless time (complete response). 40

Figure 3-9: Transient response of PT/RI system for a step change in interface resistance. (Stroke=100%, interface distributed thermal load =2.42 W).....42

Figure 3-10: Interface load curves plotted vs. $c_p(T_{B,LP}-T_{B,HP})$ for two stroke and valve settings (stroke 80%, 100% and valve ½ open, ¼ open). 44

Figure 4-1: Schematic of the transient model of the PT/RI system. The buffer volumes and check valves are not part of the model, but are shown for clarity. 49

Figure 4-2: The cold head of the pulse tube with its energy transfers including refrigeration power, thermal capacitance, and enthalpy flows. 50

Figure 4-3: SIMULINK subsystem code for the differential equation that governs the cold head temperature, Eq. (4-1). 51

Figure 4-4: Model components for the distributed load interface including heat load, thermal capacitance, and enthalpy flows. 51

Figure 4-5: SIMULINK subsystem code for the differential equation that governs the interface temperature, Eq. (4-2). 52

Figure 4-6: Parasitic heat load as a function of non-dimensional interface resistance at two values of stroke (80% and 100%). The results have been fit to linear equations (shown on graph) for use in the transient model. 54

Figure 4-7: **Mass flow as a function of non-dimensional interface resistance at two values of stroke. The results have been fit to linear equations for use in the transient model. The coefficients *g* and *h* are calculated using these equations. 56**

Figure 4-8: **Load curves for the PT\RI system with heat applied at the cold head and the cooling loop valve open. The linear fit functions are shown for two valve settings (¼ open, ½ open) and two stroke settings (80% stroke and 100% stroke). This figure is used in part to calculate the coefficients *a* and *b*....57**

Figure 4-9: **(a) Slope and (b) Intercept of the load curve as a function of the non-dimensional interface resistance at 80% and 100% stroke. The linear functions used to determine the coefficients *c, d, e, and n* are shown....59**

Figure 4-10: **Comparison of interface load curves for the experimental data and the experimentally driven model for both stroke and valve settings. 61**

Figure 4-11: **Comparison between the model and the experimental data for a step change in stroke (80% to 100%)....63**

Figure 4-12: **Comparison between the model and the experimental data of short long-term transient response to a step change in heat load (8-3 W). 64**

Figure 5-1: **State block diagram of the complete operating point, transient thermal model of the PT/RI system. 72**

Figure 6-1: **State block diagram for the simplified transient thermal model for PT/RI system....79**

Figure 6-2: **State block diagram for the interface with a PI controller. The effective interface refrigeration is assumed to be equal to the commanded effective refrigeration for the controller gain selection process....81**

Figure 6-3: **Thermal response of interface to step increase in thermal load which shows the important transient response parameters. The damping ratio is set relatively low to highlight the oscillatory behavior. 83**

Figure 6-4: **Maximum interface temperature fluctuation as a function of settling time with a fixed damping ratio of 0.707....86**

Figure 6-5: **Dimensionless interface temperature fluctuation as a function of the damping ratio. 88**

Figure 6-6: **Linear and non-linear model prediction of the controlled interface temperature response for a step increase in interface load....89**

Figure 6-7: **State block diagram for the cold head with a PI controller. The pulse tube refrigeration is assumed to be equal to the commanded refrigeration for the controller gain selection process. 90**

Figure 6-8: **State block diagram of the interface with digital control implementation. 94**

Figure 6-9: **Comparison of the controlled interface temperature response using the digital and analog models. Both models use the controller gains listed in Table 6-1 and a step increase in interface load. The digital model uses a 0.3 s sample period....95**

Figure 6-10: **Comparison of the digital controlled interface temperature response using varied controller sample period where model uses the controller gains listed in Table 6-1 and a step increase in**

interface load. The 0.3 s sample period was chosen for the experimental tests. A 12 s sample period yields an unstable system. 96

Figure 6-11: Interface response to signal noise with a settling time of 50 s. The interface valve (a) and interface temperature response (b) are shown. 98

Figure 6-12: State block diagrams for the (a) cold head and (b) interface showing the detailed relationships between the hardware physical parameters such as effective interface refrigeration, mass flow, and valve flow coefficient for the interface, and pulse tube refrigeration, compressor stroke, and variac voltage for the cold head. 99

Figure 7-1: Interface and cold head temperature response to a 0.5 W step increase in interface load with no temperature control.....102

Figure 7-2: Interface (a) and cold head (b) temperature response to a 0.5 W step increase in interface load with pulse tube refrigeration control using cold head temperature feedback.....103

Figure 7-3: Interface (a) and cold head (b) temperature response to a 0.5 W step increase in interface load with pulse tube refrigeration control using interface temperature feedback. 104

Figure 7-4: Effective interface refrigeration for the controlled 0.5 W step response shown in Figure 7-3 where the pulse tube refrigeration is adjusted using the interface temperature feedback. 105

Figure 7-5: Interface (a) and cold head (b) temperature response to a 0.5 W step increase in interface load with a cold head and interface temperature control.....106

Figure 7-6: Interface temperature response to a 0.5 W step increase in interface load with: (a) no control, pulse tube refrigeration control using the cold head temperature feedback or interface temperature feedback, and both cold head and interface control and (b) cold head control only and both cold head and interface control. 107

Figure 7-7: Manipulated cooling rate for the controller 2 (pulse tube refrigeration control using interface temperature feedback), and controller 3 (pulse tube refrigeration control using cold head temperature feedback and cooling loop mass flow control using interface temperature feedback). 109

Figure 7-8: State block diagrams for the baseline control case where the pulse tube refrigeration is regulated using (a) the cold head temperature feedback and (b) interface temperature feedback.....112

Figure 7-9: Comparison of the predicted and measured interface temperature response to a 0.5 W step change in interface load. 114

Figure A-1: Load curve for 80% stroke, valve ¼ open highlighting the change of excluding the no load data point from the mass flow and parasitic load calculation. 123

List of Tables

Table 3-1: Experimental Data - Steady State and Uncontrolled Transient Behavior: Summary of mass flow and parasitic heat loss calculations using Eq. (3-3) and Figure 3-10. 44

Table 3-2: Summary of average dimensionless interface flow resistance for nominal operation points. 46

Table 3-3: Parameters used to calculate the interface resistance and cold head/interface dimensionless times. 46

Table 3-4: Interface resistance calculations for all interface load data 47

Table 4-1: Summary of data for calculating the distribution of the parasitic load. 55

Table 4-2: Constants used in linear equations describing pulse tube refrigeration power and mass flow...60

Table 4-3: Nominal values of PT/RI parameters used in the transient thermal model. 64

Table 5-1: PT/RI parameters for a nominal operating point corresponding to an experimental data set. These parameter values are used in Section 5.3 to calculate time constants of the cold head and interface. 67

Table 5-2: Summary of coefficients from the Taylor expansion of the interface temperature state equation. 68

Table 5-3: Summary of coefficients from the Taylor expansion of the cold head temperature state equation. 69

Table 5-4: Summary of coefficients from the Taylor expansion of the pulse tube refrigeration model. 70

Table 6-1: Nominal interface controller parameters used in the experimental tests. 89

Table 6-2: Nominal cold head controller parameters used in the experimental tests. 92

Table A-1: Mass flow and parasitic load data for 80% stroke, ¼ open valve setting showing the difference when the no load data point is cut out. 123

List of Variables

Nomenclature

a	Coefficient relating interface valve resistance, stroke, and cold head temperature to refrigeration power (W K^{-1})
b	Coefficient relating interface valve resistance and stroke to refrigeration power (W)
c	Slope coefficient relating interface valve resistance and the coefficient "a" (W K^{-1})
C	Capacity (J kg^{-1} K^{-1})
c_p	Constant pressure specific heat of Helium (J kg^{-1} K^{-1})
C_{PI}	Proportional Integral controller
C_v	Valve flow coefficient
d	Offset coefficient used to calculate the "a" coefficient (W $K^{-1)}$
e	Slope coefficient relating interface valve resistance to the coefficient "b" (W)
e_T	Temperature error
f	Fraction of full compressor stroke
g	Coefficient relating stroke and interface valve resistance to interface mass flow (kg s^{-1})
h	Coefficient relating stroke to interface loop mass flow (kg s^{-1})
$H.O.T$	Higher Order Terms, referring to terms higher than 1st order in a Taylor expansion
j	Coefficient relating stroke and interface valve resistance to parasitic heat (W)
k	Coefficient relating stroke to parasitic heat (W)
k_i	Integral controller gain
k_p	Proportional controller gain
$\dot{m}$	Mass flow (g s^{-1})
n	Offset coefficient relating interface valve resistance to the coefficient "b" (W)
P	Pressure
$\dot{q}$	Heat transfer (W)
r	Fluid flow resistance (kPa s kg^{-1})
R	Non-dimensional interface valve fluid flow resistance
Rg	Ideal gas constant for helium (kJ kg^{-1} K^{-1})
s	Analog domain Laplace operator
t	Time (s)

t_p	Time to temperature fluctuation peak
T	Temperature (K)
V	Volume (m^3)
z	Z-transform operator used for digital model
*	Commanded value

Greek symbols

β	Function of ζ defined for convenience
Δ	Change, or change away from nominal operating point
ϕ	Function of ζ, β defined for convenience
ρ	Density (kg m^{-3})
τ_{comp}	Compressor period (s)
τ	Time constant (s)
ω_n	natural frequency
Ψ	Non-dimensional time
ζ	Damping Ratio

Subscripts

B	Buffer volume
C	Cold head
C,d-eff	Effective cold head thermal disturbance
des	Desired value
DL	Distributed load or Interface
elec	Electric
H	Hot heat exchanger temperature
HP	High pressure
I	Interface or distributed load
$I,r\text{-}eff,\dot{m}$	Effective interface refrigeration resulting from changing the cooling loop mass flow
$I,r\text{-}eff,T_C$	Effective interface refrigeration resulting from changing the cold head temperature
LP	Low pressure
max	Maximum

nom	Nominal
p	Parasitic
pt	Pulse tube
s	Settling time
swept	Amount of volume displaced by compressor piston during cycle
0	Nominal, operating point
80	80% compressor stroke
100	100% compressor stroke

1 Introduction

1.1 Future Goals of NASA Space Program

NASA is continuously evolving its technology–driven and ambitious goal of understanding our solar system as well as galaxies far beyond our own. Early missions such as Voyagers 1 and 2 were launched in the late 1970's and were intended to be unmanned explorations of our surrounding solar system, specifically, Jupiter, Saturn, Uranus, and Neptune. The unexpected durability of these satellites has allowed them to be used for exploration beyond our solar system; these satellites have been used to capture impressive images and information about our own solar system by "looking back" at the planets that they had traveled beyond [1]

Inspired by the success of such missions, NASA is moving onward with a focus on manned missions, including missions to mars and the international space station. Tools are being developed in order to test for the essential, life-sustaining molecular building blocks on Mars. Additional efforts underway at NASA include satellite missions to study distant galaxies; for example, galaxies in early stages of formation will be observed to deepen our understanding of how our own galaxy and planets might have formed.

A common critical component for all of these missions is cryogenic technologies; for example, the manned mission to mars requires active cooling to maintain liquid propellant supplies [2] for the 180 day transit time and 500 day surface stays. Additionally, the mars mission will involve multiple launches; sections of the spacecraft, including the propellant tanks, will be launched separately and stored in Low Earth Orbit (LEO) where they will be assembled before the voyage to mars. The propellants must be actively cooled during this Earth-orbit period. Another NASA application which requires active cryogenic refrigeration is the Single Aperture Far-Infrared

(SAFIR) [3] telescope which would be used for capturing images of distant galaxies. Radiation noise reduction is important when using the ultra-sensitive infrared (IR) detectors on SAFIR; therefore, the satellite components in view of the detectors must be cooled to reduce the incident parasitic radiation.

1.1.1 Single Aperture Far-Infrared (SAFIR) Telescope

Clues to the formation mechanics of our galaxy and planets can be found by observing other galaxies in their early stages of development. Many forming galactic bodies, including planets and stars, are enshrouded with "galactic dust" [3]. The dust is most emissive in the infrared wavelengths as the dust temperature is typically in the range of 30 K to 50 K. The distant galaxies are therefore best observed by capturing the infrared emissions of this dust. These IR light wavelengths are largely absorbed by the moisture in the earth's atmosphere; therefore an IR detecting orbital satellite is an appropriate solution for capturing the maximum amount of IR light.

The SAFIR telescope is scheduled for launch in 2015 to 2020 and is meant to capture the infrared radiation emitted from the forming galactic bodies. SAFIR will use a large system of mirrors to focus the light onto an array of sensitive IR detectors. A conceptual image of the SAFIR telescope in shown in Figure 1-1.

http://safir.jpl.nasa.gov/technologies.shtml

Figure 1-1: Conceptual image of the SAFIR telescope, planned for launch in 2015-2020

The components of the satellite itself (including the mirrors used to direct the light) are a source of radiative noise for the IR detectors. Passive and active cryogenic cooling can be employed to cool the satellite components which radiate to the detectors. Typical methods for providing passive radiative cooling (by exposure to deep space) can achieve temperatures in the range of 30 K to 60 K [3]. Detector sensitivity can be increased by orders of magnitude by using active cooling technologies which can achieve temperatures as low as 4 K. Figure 1-2 shows the temperature and wavelength dependence of detector sensitivity. NASA's website offers an explanation of the detector sensitivity:

> "To put SAFIR's sensitivity into perspective, suppose you turned on a small flashlight, powered by two AA batteries, sealed it inside a basketball, and launched it into the frigid depths of space. The little light bulb would raise the temperature of the ball's surface to 115 Kelvin (115 degrees Celsius above absolute zero, or around -253° F), and this tiny amount of heat would radiate at far-infrared wavelengths. SAFIR would be able to detect it at a distance of nearly four million miles, or 15 times the distance to the moon."

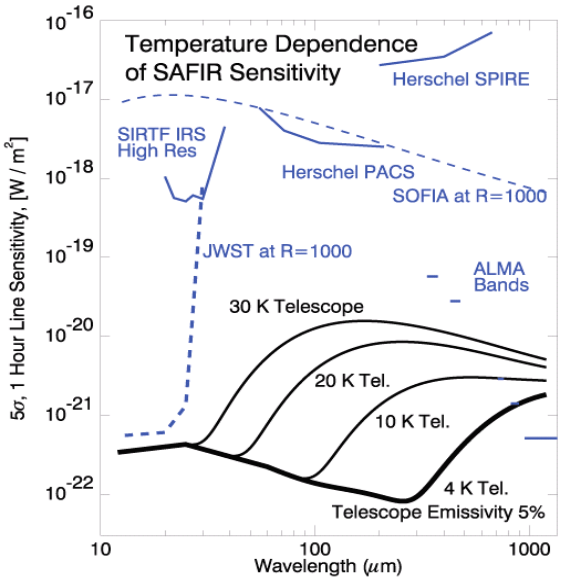

http://safir.jpl.nasa.gov/technologies.shtml

Figure 1-2: Temperature and wavelength dependence of IR detector sensitivity for the SAFIR telescope.

A major technological difficulty with implementing actively cooled components is the distribution of the cooling power produced by the mechanical cryocooler. The SAFIR mirrors will be approximately 8-10 m across [3] and therefore present large areas that must be cooled uniformly as well as a significant distance over which the cooling must be transported efficiently. One method of providing this distributed cooling using a central cryocooler interfaced with multiple cryogen distribution loops is investigated in this research.

1.2 Description of Application and Current Methodologies

Future instruments and platforms for NASA space applications, such as the manned mission to mars and the SAFIR telescope, will require increasingly sophisticated thermal control technology, and cryogenic space applications will become increasingly more common. These technologies must provide distributed cooling and multiple heat lift. In many cases, the source of the cooling (the cryocooler) must be thermally decoupled from the load during periods where the cooler is not operating. While a number of mechanical cryogenic refrigeration systems may

be considered for such applications, none offers the same potential for low vibration, reliability, and efficiency as the pulse tube.

1.2.1 Current Methodology 1 - Conductive Strap

Regenerative coolers such as pulse tubes typically have small cold heads that must be conductively coupled to heat loads [4]. Thermal integration via conductive coupling is not ideal for distributed loads such as those represented by large, deployable structures. The thermally conductive strap that can transport even a small refrigeration load over a large difference with a reasonable temperature drop quickly becomes unacceptably large for a flight cryocooler. Also, in order to achieve the levels of electrical and vibration isolation that are often required for a space-based detector, the thermal link must simultaneously have high thermal conductivity, low electrical conductivity, and a large amount of mechanical compliance – a combination that is not simple or economical to achieve.

1.2.2 Current Methodology 2 - Capillary and Mechanical Pumped Loop

Alternative technologies for thermal distributed load integration based on fluid flow include the capillary pumped loop (CPL), which is gravity dependent and therefore restricts ground test configurations. The CPL also suffers from thermal losses that are related to the thermal interface that must exist between the refrigeration system and the fluid in the CPL. Flow through the CPL cannot be controlled via an active throttle valve and therefore this temperature control option is not available. The behavior of the CPL is typically gravity dependent which makes ground testing difficult. A mechanically pumped loop suffers from the same interface loss as the CPL as well as the parasitic power that is required to run the pump. Both the CPL and the mechanically pumped loop options represent additional complexity in the system and thus present reliability issues.

1.3 Pulse Tube Rectified Interface Concept

Figure 1-3 illustrates the technique that is considered in the remainder of this report for thermally integrating a pulse-tube (or any regenerative cryocooler) with a distributed load, such as the SAFIR telescope. A rectifying interface composed of check-valves [5] and buffer volumes converts the oscillating pressure within the cryocooler to a quasi-steady pressure difference between the two buffer volumes; this pressure difference is used to provide a small, steady flow of cold gas that is capable of transporting the refrigeration capacity much more efficiently than a conductive strap. The Pulse Tube Rectifying (PT\RI) interface methodology could be extended to include multiple distributed loads as shown in Figure 1-3. Cryocooler efficiency in general increases with capacity [6]; it is therefore more practical to use a large, centrally located cryocooler with distribution capability as opposed to multiple, smaller cryocoolers.

To illustrate the potential performance of the PT/RI system, consider the following situation. The small mass flow rate of 75 mg/s can be obtained from a rectifying interface without substantially affecting the performance of the pulse-tube and easily transport 1 W over 1 m with a temperature rise of only 2.5 K. In contrast, a conductive thermal link composed of oxygen-free, high-conductivity (OFHC) copper would require a cross-sectional area of 8.7 cm2 which results in a large mass (7.8 kg). In addition to this mass penalty, the use of a conductive link limits the mechanical and electrical flexibility of the interface whereas the cooling loop can be made both mechanically compliant and electrically non-conductive in order to provide vibration as well as voltage isolation. The rectified flow loop relies on a pressure-driven, single-phase flow and therefore will be gravity independent; this characteristic greatly facilitates ground-test and flight qualification. The interface loop mass flow can be controlled using a throttle valve as shown in Figure 1-3; the system therefore has the secondary benefit of rapid and therefore

precise load temperature regulation through actively controlled flow modulation. Taylor [7] describes a cryogenic piezoelectric valve which in the future, could be integrated with temperature sensors and heat exchangers to provide temperature control for multiple loads.

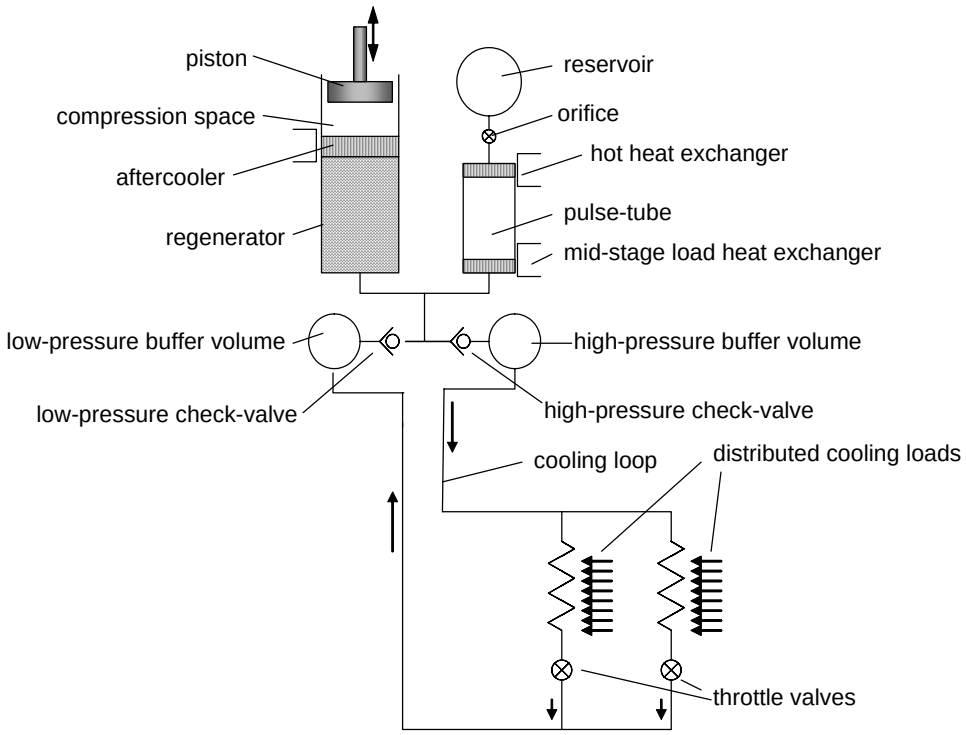

Figure 1-3: Schematic of a single-stage, Stirling-type pulse-tube integrated with multiple, distributed loads using a rectifying interface.

This report presents steady-state and transient experimental testing which characterize the refrigeration performance of the system relative to the controlled inputs (i.e. compressor stroke and interface loop mass flow), as well as the thermal and fluid dynamics which govern the dynamic behavior of the cooling loop. The steady-state results show how the integration of the rectifying interface and cooling loop affect the efficiency of the system. The transient results are used to develop a system thermal model, which is subsequently used to develop the temperature control algorithms. The control algorithms have been experimentally implemented, and demonstrate the rapid temperature control authority associated the interface throttle valve.

This primary goal of this research is to demonstrate the dynamic control available with the PT/RI system, so the steady state internal pulse tube fluid and thermodynamic modeling efforts are not described exhaustively here. A quasi-steady model of the system has been developed and compared [8] with the empirical steady state performance presented in Chapter 3. The model is essentially equivalent to the existing system models that have been developed at the UW-Madison for the design of pulse-tube [9] and hybrid cryocoolers [10]; readers are referred to [11, 12, 13] for the details of these models.

1.4 Thesis Outline

The primary purpose of this thesis is to demonstrate the ability PT/RI to actively control the temperature of a single distributed load. The system is verified experimentally by varying the distributed load using a heater interfaced with the interface distribution tubing. The temperature response at the distributed load characterizes the performance of the system; important performance parameters include the maximum temperature fluctuation at the load.

Chapter 2 describes the experimental apparatus used to test the PT/RI system including a description of the rectifying interface and the hardware used to implement the control algorithms. Chapter 3 presents experimental results which characterize the steady state and transient performance of the uncontrolled system. Empirical relationships are developed between important system inputs such as compressor power, cooling loop throttle valve restriction, heater power, and system outputs such as temperatures, pressures, cooling loop mass flow, pulse tube refrigeration power. These empirical relationships are used to create a thermal model of the system which is discussed in Chapter 4. Chapter 5 describes a linear model of the complete, non-linear model developed in Chapter 4. The linear model is further simplified in Chapter 6, and used with linear control theory to develop a closed form design process for a Proportional-

Integral (PI) controller. The desired temperature performance characteristics in terms of maximum temperature fluctuation and settling time for a step increase in load can be used to directly select the PI controller gains. Chapter 8 shows the experimental verification of the control strategy, and discusses the advantages of using the cooling loop throttle valve as a means of temperature control. Finally, Chapter 8 summarizes the key conclusions that were obtained from the research and includes a step-by-step process for selecting controller gains, as well as recommendations for future work.

1.5 References

1. NASA, "Missions", http://www.nasa.gov/, Ed. Yvette Smith, updated 3/28/2007
2. Salerno, L.J., Kittle, P., "Cryogenics and the human exploration of Mars", *Cryogenics*, Vol. 39, pp. 381-388, 1999
3. SAFIR, "Single Aperture Far-Infrared (SAFIR) Observatory", Jet Propulsion Lab – California Institute of Technology, http://safir.jpl.nasa.gov/technologies/index.asp, updated March 28, 2007
4. Nellis, G.F. Lachner, B.F., Jr.; Lokken, O.D.; Stahl, B.L.; Crawford, L.D., "Thermal resistance measurements for flexible straps at cryogenic temperatures", AIP Conference Proceedings, n 710, pt.1, 2004, 651-8
5. Diab, A. K., Nellis, G. F., Maddocks, J. R., and Yarbrough, S., "Development of a Rectifying Interface for a Hybrid Pulse-Tube/Reverse-Brayton Cryocooler," in *Advances in Cryogenic Engineering* 49B, edited by J. Waynert et al., American Institute of Physics, New York, 2004, pp. 1777-1782
6. Radebaugh, Ray., "Cryocooler Technology", *A 3-Day Short Course,* February 13-15, 2001
7. Taylor, R.P., "A Micromachined Cryogenic Valve for Distributed Cooling Applications", M.S. Thesis from the University of Wisconsin, Madison, USA, 2005
8. Skye, H.M., Hoch, D.W., Nellis, G.F., Klein, S.A., Maddocks, J.R., Roberts, T. and Davis, T., "Rectified Continuous flow loop for the thermal management of large structures", 2005 Cryogenic Engineering Conference, Paper # C3-M-07
9. Potratz S., Nellis, G., Maddocks, J. and Pfotenhauer, J,. "Design and Test of a 300 W Pulse Tube Refrigerator," in *Proceedings of the ASME Advanced Energy Systems Division*, 2004, Paper IMECE2004-60806
10. Nellis, G. F. and Maddocks, J. R., "An isothermal model of a hybrid Stirling reverse-Brayton cryocooler", *Cryogenics* 43, pp. 31-43, (2003).
11. Diab, A. K., *Modeling and Optimization of a Hybrid Cryocooler,* University of Wisconsin Mech. Eng. Dept., Wisconsin, 2004.
12. Potratz, S., *Development of Large Capacity Pulse Tube Cryocoolers*, University of Wisconsin Mech. Eng. Dept.,Wisconsin, 2005.
13. Gary J., O'Gallagher, A., Radebaugh, R., and Marquardt, E., "Regen 3.2: User Manual", NIST, 2001.

2 Experimental Setup – Pulse Tube Rectifying Interface, Automatic Control Hardware, and Data Acquisition

2.1 Pulse Tube Rectifying Interface

The experimental apparatus shown in Figure 2-1 was designed and fabricated in order to demonstrate the rectified cooling loop concept and automatic temperature control. Additionally, the experimental apparatus was used to verify an analytic, quasi-steady state model of the pulse tube rectifying interface (PT\RI). These results are discussed in [1]. A Stirling-type pulse-tube consisting of a linear compressor, water-cooled aftercooler, regenerator, pulse-tube, hot heat exchanger, inertance tube, and reservoir was integrated with a rectifying interface. The rectifying interface consists of two check-valves (shown in Figure 2-2) constructed of spring steel and two buffer volumes. The check-valves design is discussed in [2]; the design procedure used to specify the geometry of the check valve limits the stresses induced in the spring steel to a value that is below the endurance limit of the material, provides a dynamic response that is much faster than the 60 Hz operating frequency, and results in an open valve resistance that is sufficiently small.

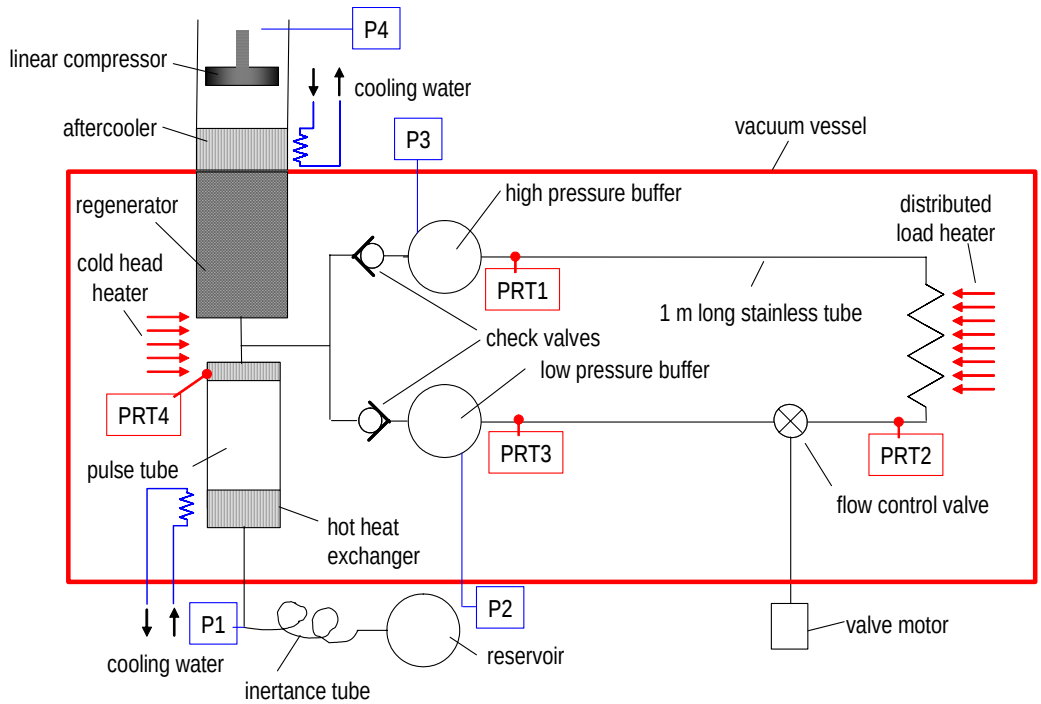

Figure 2-1: **Schematic of the PT/RI experimental apparatus showing the location of key measurements of pressure and temperature.**

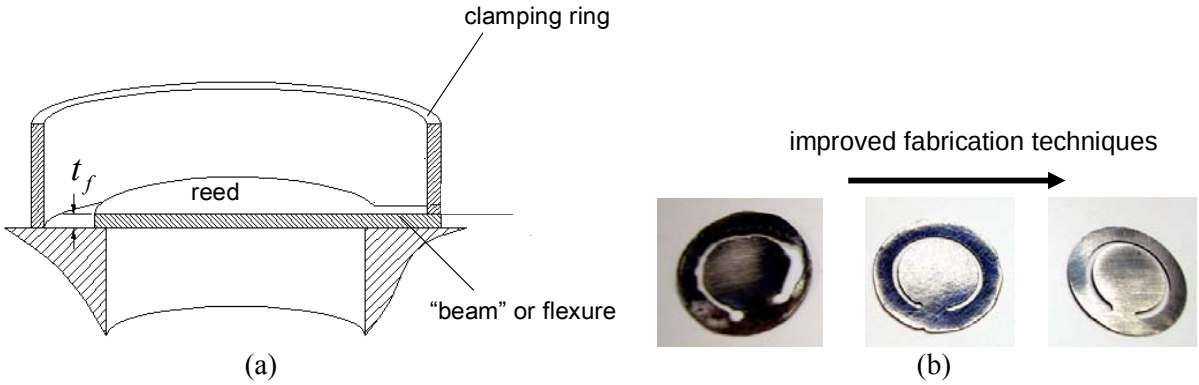

Figure 2-2: **(a) Schematic of the reed-type check-valves that are used within the rectifying interface and (b) photographs of the reed sub-component during the development process showing the improvement in the fabrication process.**

The high and low pressure buffer volumes are connected by a 1.0 m long, 1.6 mm inner diameter thin-walled stainless steel tube that represents the cooling loop; the cooling loop dimensions were selected in order to demonstrate the ability of the system to transport cooling capacity over a large distance. The flow rate between the buffer volumes is controlled using a cryogenic flow control valve; the original grease on the valve actuation threads was removed and replaced with

Apiezon™ "N" grease which maintains its lubrication properties at the low temperatures (110-160 K) used in this experiment. The actuation motor for the valve is located outside the vacuum vessel and is linked to the valve stem via a stainless steel tube in order to control the heat leak. The regenerator, rectifying interface, cooling loop with the control valve, pulse-tube, and hot heat exchanger are covered with aluminized mylar radiation shielding and enclosed within a vacuum vessel that is evacuated using a turbomolecular pump. The vacuum levels used in the experiment are less than $1x10^{-4}$ torr and therefore parasitic convective and conductive heat transfers are effectively eliminated.

Electrical heaters used to simulate thermal loads are attached directly to the pulse tube cold head (referred to as the cold head heater) and also at the mid-point of the cooling loop (referred to as the distributed load heater); the electrical input power to the heaters is calculated from measurements of the DC current and voltage. The compressor stroke is measured indirectly using an omegadyne PX1006K1-015DV 0-15 Psi differential pressure transducer that is installed on the back-side of the compressor (shown schematically as P4 in Figure 2-1, and identified in the photograph in Figure 2-3). The amplitude of the pressure oscillation is compared with the amplitude at full stroke to calculate a stroke percentage; section 3 further discusses the stroke calculation process. Additional pressure measurements were obtained using Endevco™ 8510B-500 pressure transducers. These additional pressure measurements include the high and low pressure buffer volume pressure (P3 $P_{B,HP}$ and P2 $P_{B,LP}$) and the pressure in the hot heat exchanger (P1). A Lakeshore™ PT-102 platinum resistor temperature (PRT) sensor is mounted on the cold head (PRT4, referred to as T_C). Additional PRTs are mounted within the cooling loop tube immediately upstream of the high pressure buffer (PRT1, referred to as

$T_{B,HP}$), after the interface distributed load heater (PRT2 , referred to interchangeably as distributed load temperature - T_{DL} and interface temperature - T_I), and before the low pressure buffer (PRT3 referred to as $T_{B,LP}$). The components within the vacuum vessel (excluding the control valve) are shown in Figure 2-4. The flow control valve and motor actuator are shown in Figure 2-5.

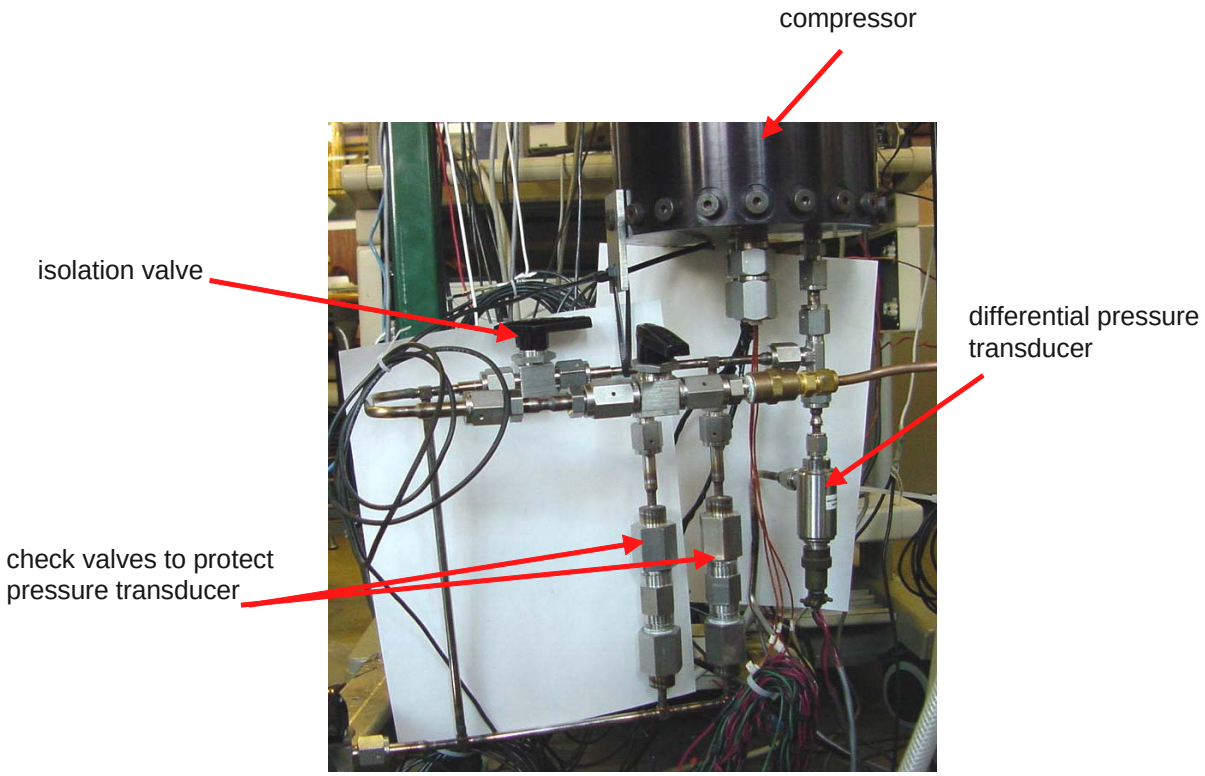

Figure 2-3: Differential pressure transducer (P4) used to infer the compressor stroke.

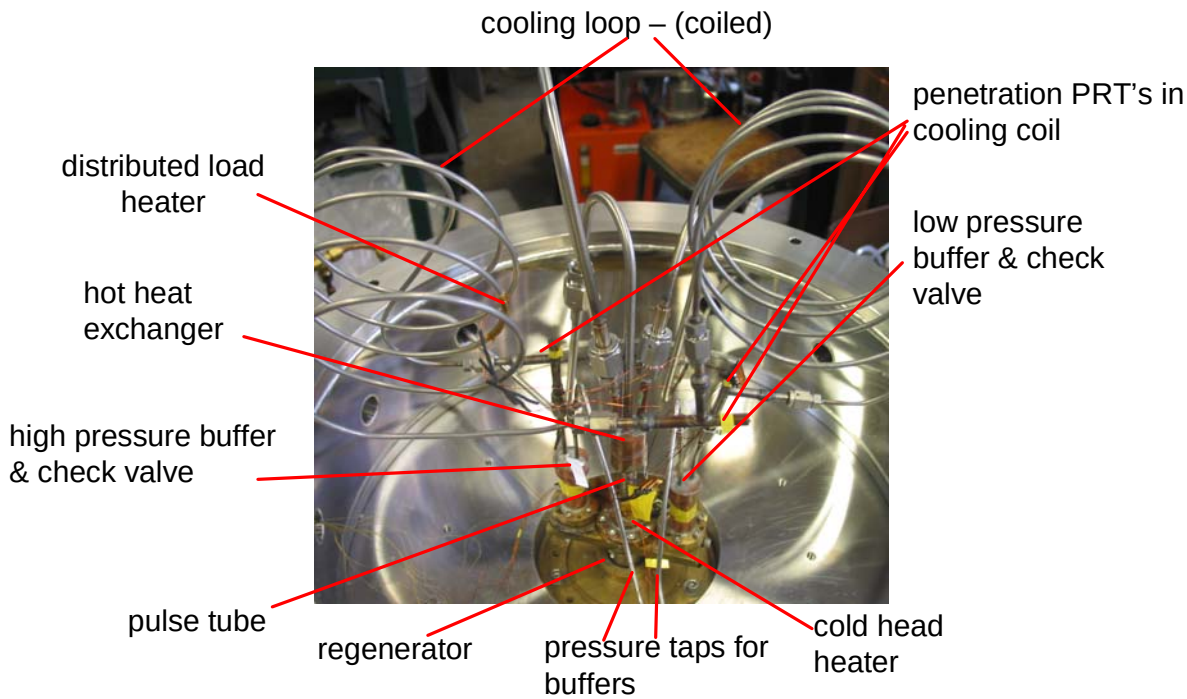

Figure 2-4: Photograph of the components within the vacuum vessel (flow control valve not shown).

2.2 Motorized Cooling Loop Flow Control Valve

The cryogenic flow control valve (Swagelok™ SS-4BMG-VCR metering stem tip, bellows sealed) which regulates the flow in the cooling loop is actuated by a Vexta PK246PA 2-phase stepping motor that is mounted outside the vacuum vessel. The valve actuation handle (valve stem) is connected to the motor by the assembly shown in Figure 2-5. Figure 2-6, Figure 2-7 and Figure 2-9 show detailed geometric drawings of the motorized valve assembly and individual components. The assembly components include:

1. A 7.94 mm (5/16") OD stainless steel (SS) tube with 0.089 mm (0.035") wall thickness that passes through the vacuum vessel. The vacuum vessel pass-through for the shaft is sealed with an o-ring connector.

2. A coupling/coupling key assembly – both components are machined from 303 SS. The coupling is welded to the end of the SS shaft outside the vacuum vessel. The coupling key is connected to the stepping motor via a flexible motor coupling.

3. Two flexible motor couplings (Oriental Motor model #'s MC1605F03C and MC2008F05C) connect the valve stem to the SS shaft and the coupling key to the motor shaft, as shown in Figure 2-5.

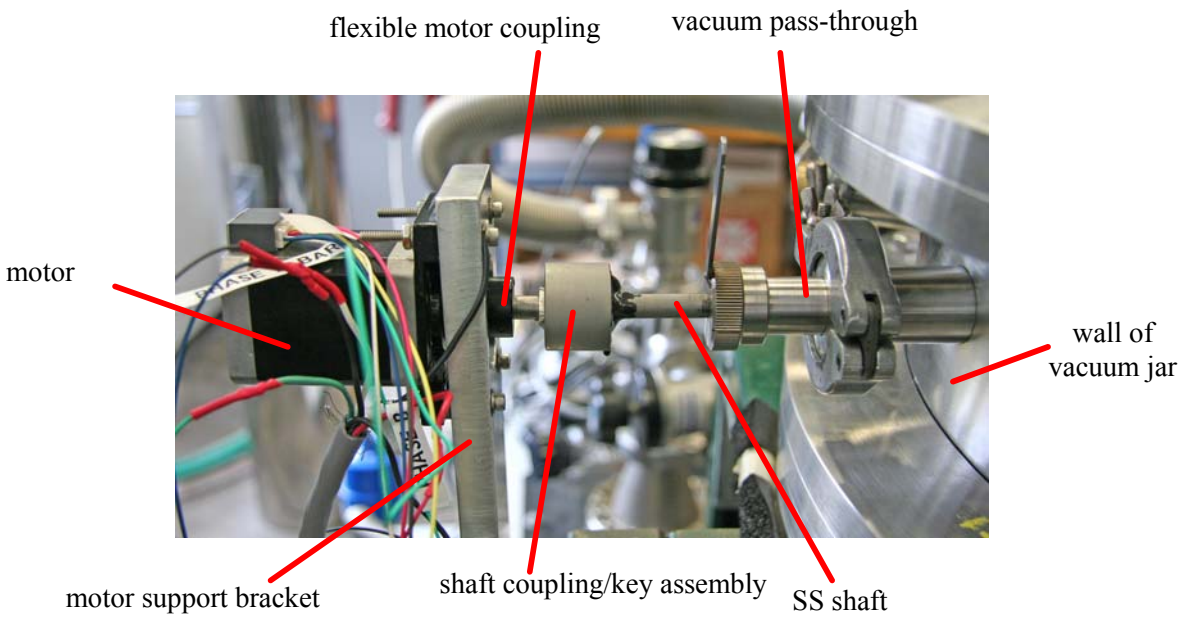

(b)

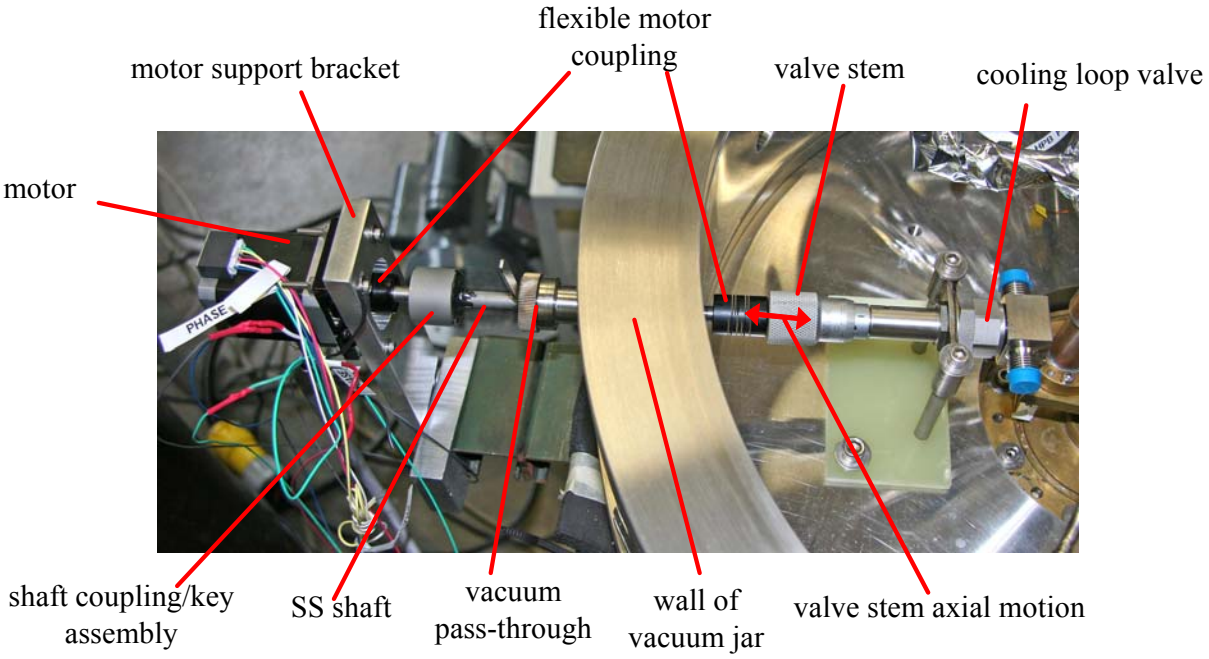

(a)

Figure 2-5: **(a) top view and (b) side view of: the motorized cooling loop valve setup highlighting the shaft coupling which accommodates the axial translation of the valve stem while providing a torque linkage from the motor to the valve.**

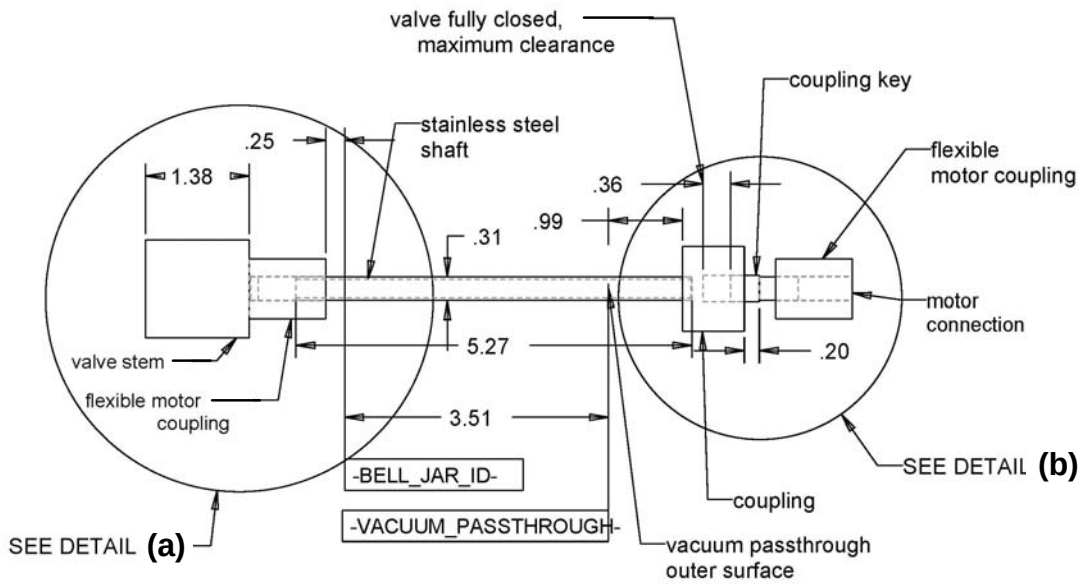

Figure 2-6: **Detailed schematic of the motorized valve assembly shown in inches. In this figure, the gap between the coupling key and the coupling (0.36 in.) represents the gap when the valve is completely closed. The gap when the valve is fully open is approximately 0.11 in. Figure 2-7 shows the detailed sections (a) and (b).**

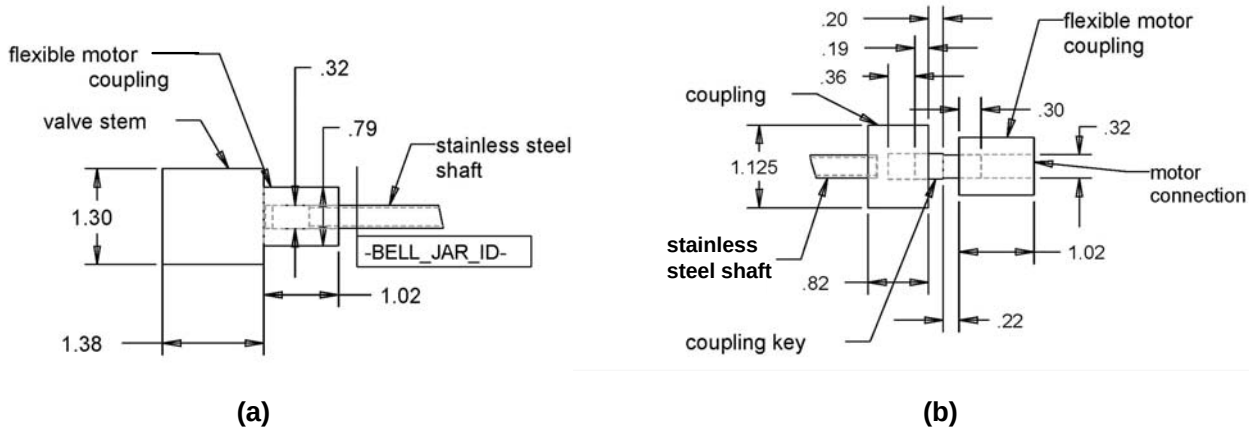

Figure 2-7: **Detailed sections (all measurements in inches) of the motorized valve assembly. (a) Components inside the bell jar including the cooling loop valve step. (b) Components outside the bell jar including the coupling, coupling key and motor connection.**

The cooling loop valve handle translates axially as it turns. The coupling and coupling key were therefore fabricated for integration with the fixed position motor outside the vacuum vessel. The coupling/coupling key assembly allows free axial motion but is torsionally rigid in order to

support valve rotation. The coupling/coupling key assembly is located outside of the bell jar, as indicated in Figure 2-5.

The tolerance between the shaft connected to the motor and the coupling is 50 μm (0.002 inch), which allows for very little rotational play in the connection and therefore eliminates potential control issues related to dead zones. The coupling and coupling key are shown schematically and pictorially in Figure 2-8. Detailed geometric drawings of the coupling, coupling key, and valve stem are shown in Figure 2-9.

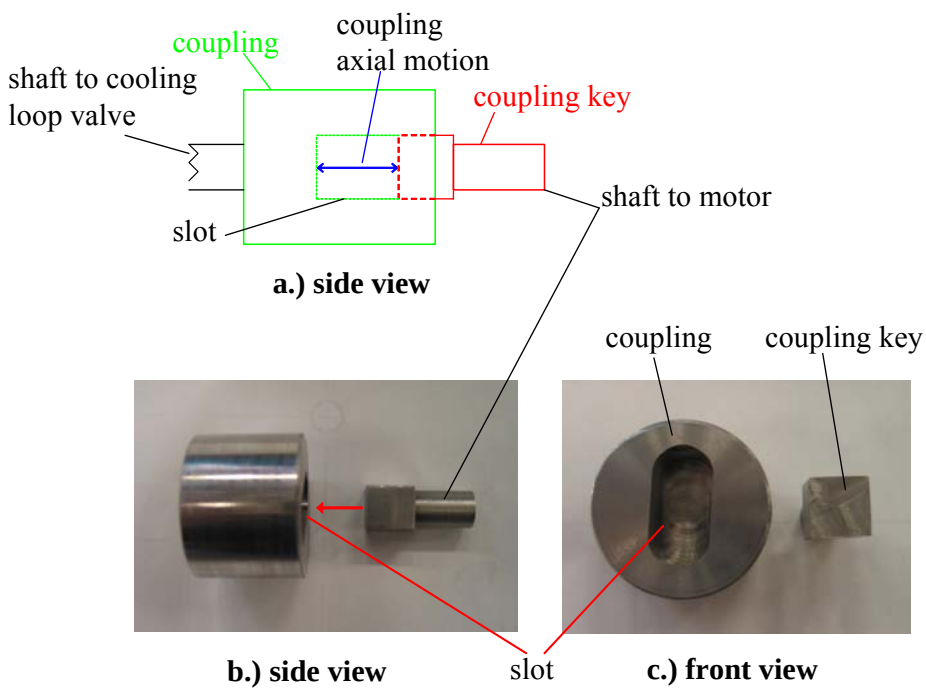

Figure 2-8: **Coupling for motorized valve shaft assembly which allows axial motion and provides torsional support for valve stem rotation: (a) side view of schematic, (b) side view of fabricated coupling assembly, and (c) front view of fabricated coupling assembly.**

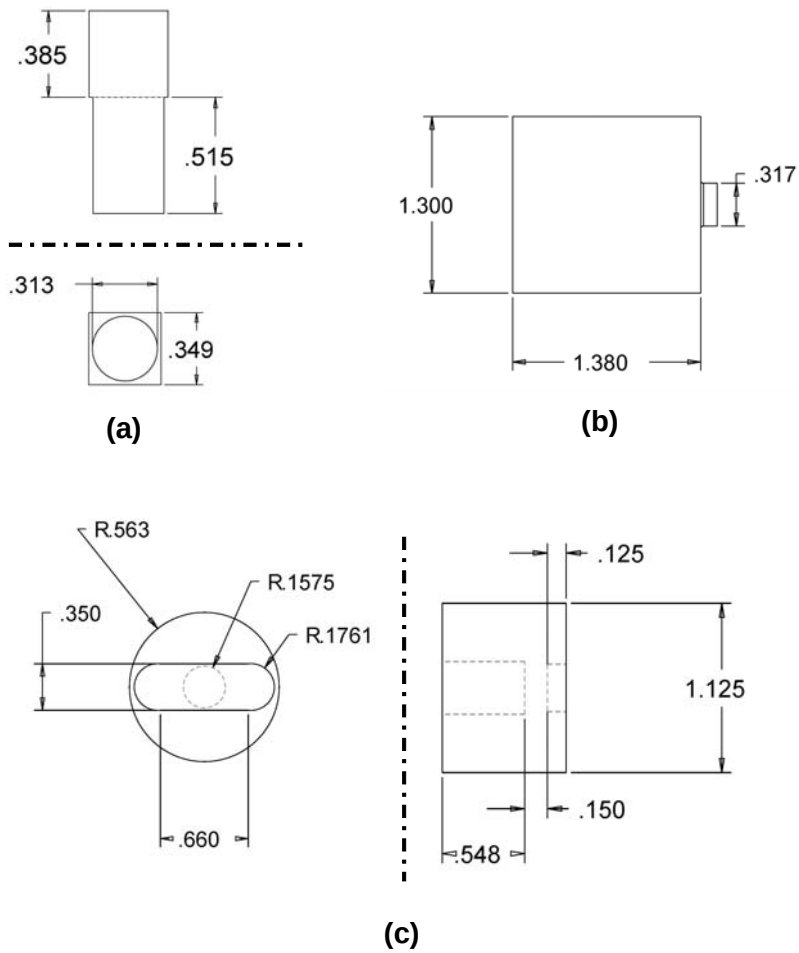

Figure 2-9: Detailed schematics of several of the motorized valve assembly including: (a) coupling key, (b) valve stem, and (c) coupling.

2.3 LabVIEW Data Acquisition and Control Program

A LabVIEW^{TM} Virtual Instrument (VI) program was used to acquire the system data including: temperatures, pressures, and measured heater power. The program implements the control algorithms developed in chapter 6 by computing and supplying the appropriate commands for the variac voltage, cooling loop valve flow resistance, and heater power. Figure 2-10 shows a simplified conceptual diagram of the VI, the complete program including the appropriate sub-VI's is included electronically with this document.

First, the program acquires a set of 1000 raw signal data points at a rate of 17.5 kHz. Note that the temperature signals are pre-filtered with 15 Hz low-pass analog filters. The program processes the 1000 data points using a digital low pass filter. Each filtered signal is then averaged to produce a single value; it is this value which is used to compute the control algorithms. The process repeats every 0.3 s, so the control loop has an effective 3.33 Hz sample rate. Note that the 1000 data points recorded at 17.5 kHz each control loop cycle are discarded every cycle to avoid unnecessarily large data files.

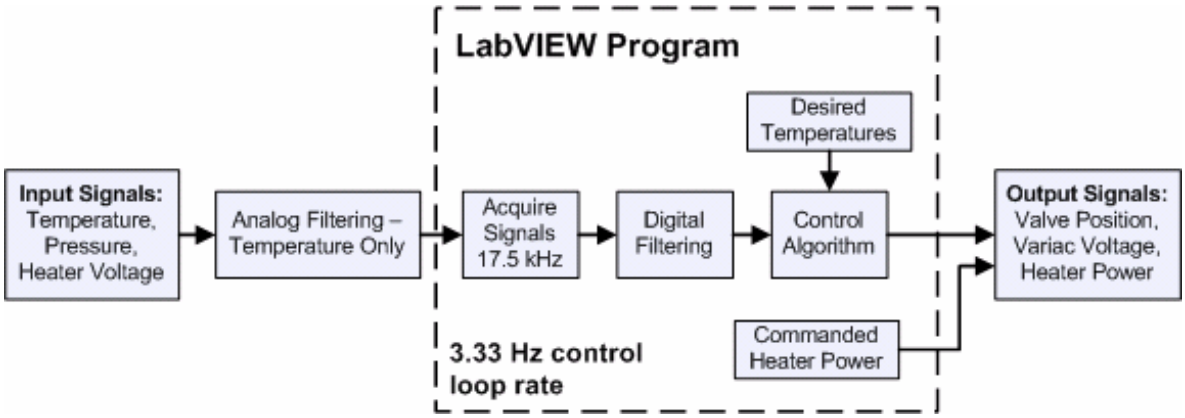

Figure 2-10: Conceptual diagram of Labview VI used to acquire the system data and implement the temperature control algorithms

2.4 Signal Conditioning

Control systems in general are sensitive to noise within feedback signals. Large signal to noise ratios are problematic in that the control hardware will respond to noise, reducing performance and even causing instability. The PT/RI system relies on temperature sensor signals for regulating the cold head and interface temperatures, therefore passive filtering methods were used to condition these signals.

The interface has the smallest thermal mass of interest in the system and therefore has the shortest time scale. Chapter 3 shows that the interface time scale is about 20 s, or 0.05 Hz. The

low bass bandwidth frequency should be at least an order of magnitude greater than dynamic signals of interest. A frequency analysis of the temperature signals showed significant noise levels in the kHz range, so a cutoff frequency well below this range is used. Two filters were used for each of the feedback temperature signals. A 100 Hz low-pass digital Infinite Impulse Response (IIR) 5th order Bessel filter is used in combination with an analog 15 Hz low-pass RC filter. The digital filtering is accomplished using LabVIEW™ software as shown in Figure 2-10 and Figure 2-11, as well as the VI program included with this document.

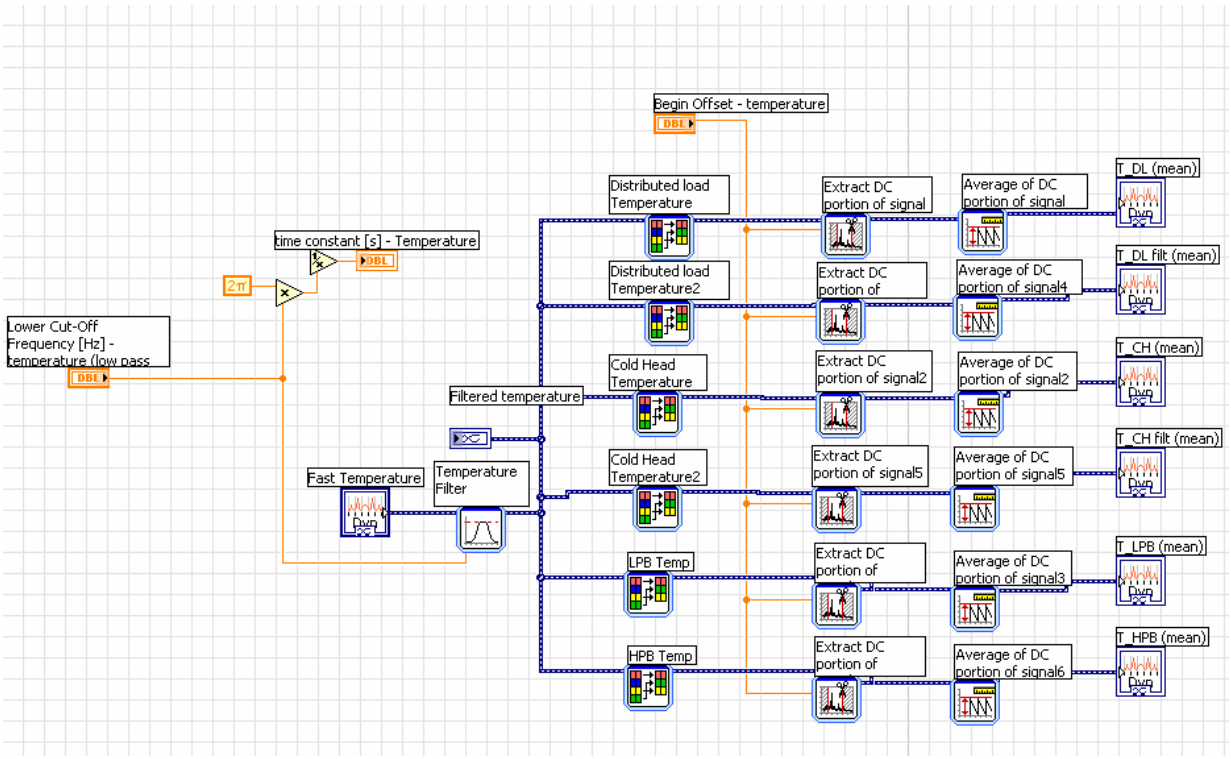

Figure 2-11: LabVIEW implantation of digital Infinite Impulse Response (IIR) temperature signal filtering

2.5 Automatic Control Hardware

The PTRI system uses automatic feedback control based on the cold head and distributed load temperatures in order to minimize the temperature fluctuation induced by heat load disturbances The cold head is a relatively large thermal mass and it therefore has a long time constant (1000's

of seconds) and responds slowly to load disturbances. Adjusting the compressor stroke changes the refrigeration delivered at the cold head on a similarly long time scale. Therefore, the control system makes adjustments to the compressor stroke in order to control the cold head temperature. The distributed load temperature fluctuates with load changes on a much shorter scale (10's of seconds) because of its relatively small thermal mass. The distributed load temperature can be controlled with the same short time scale by adjusting the cooling loop mass flow rate; therefore, the control system adjusts the cooling loop valve in order to regulate the distributed load temperature. Chapter 3 includes a more detailed discussion of the cold head and distributed load response.

The hardware and software used to control the distributed load temperature are shown schematically in Figure 2-12. The LabVIEW™ interface records the distributed load temperature using a NI PCI-6229 Multifunction (Analog input/output) data acquisition (DAQ) card and uses the control law to calculate the required corrective cooling loop mass flow adjustment. A NI PCI-7332 stepper motor motion control card then commands the NI MID-7602 stepper motor driver to make appropriate adjustments to the motorized cooling loop valve.

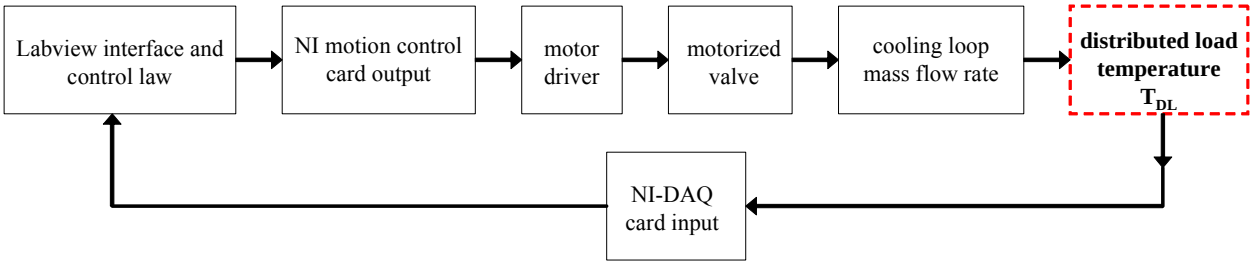

Figure 2-12: Distributed load temperature feedback control hardware and software components.

The cold head temperature is controlled using a similar feedback loop. The LabVIEW control algorithm calculates the required compressor adjustment based on cold head temperature fluctuations. An ISE 5-M1010-BCT single phase 60 Hz 0-115 VAC motor controlled variac provides power for the compressor. The variac output voltage (and subsequent power) to the compressor is controlled by a 0-3.5 DCV signal from the NI PCI-6229 DAQ card. Figure 2-13 schematically shows the software and hardware in the cold head temperature feedback loop. Additionally, Figure 2-14 shows the relationship between the 0-3.5 DCV input and the 0-115 VAC output for the motor controlled variac. Figure 2-15 shows a picture of the motor controlled variac.

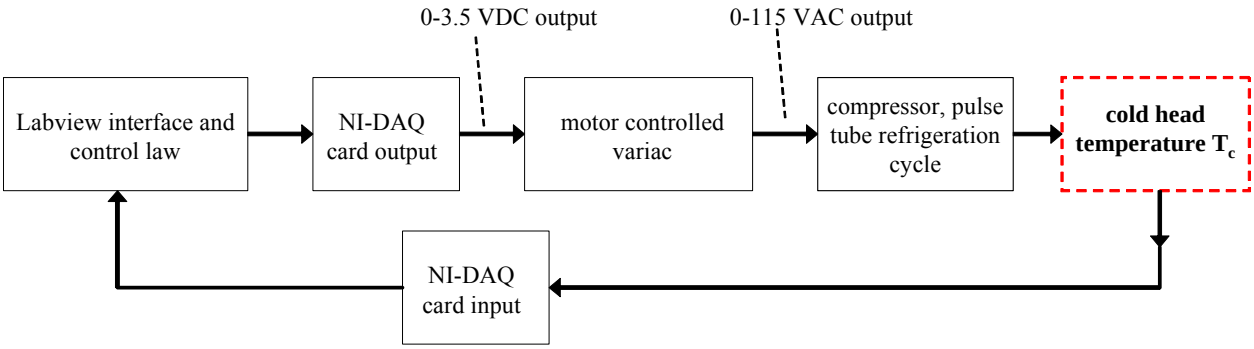

Figure 2-13: Cold head temperature feedback control hardware and software components.

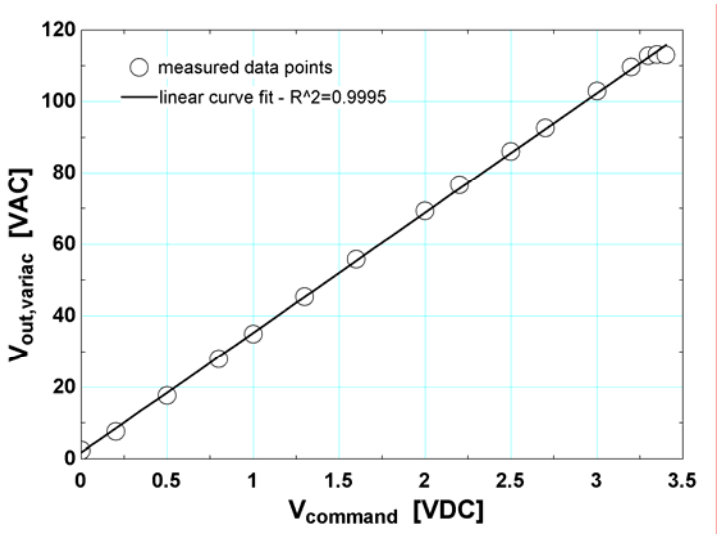

Figure 2-14: Motor controlled variac output voltage vs. input 0-3.5 DCV.

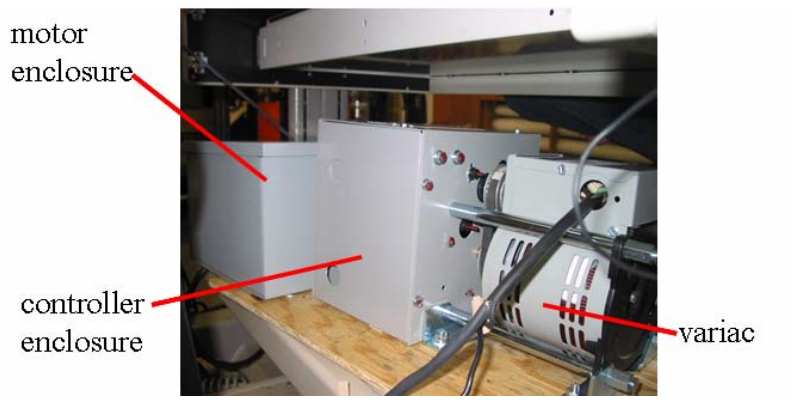

Figure 2-15: Picture of the motor controlled variac. The variac outputs 0-115 VAC to the compressor based on a 0-3.5 VDC command from the LabVIEW VI.

2.6 Computer controlled heater circuit

The experimental verification of the temperature control system includes an investigation of the temperature response to various disturbance heat load schemes. The control parameters are selected based on the modeled performance for a step change, sinusoidal, as well as stochastic heat load variations. A convenient method to provide these types of load variations is a computer controlled voltage applied to a resistance heater. However, the voltage and power that can be applied directly from the computer's data acquisition is limited. Therefore, an external

source of power is needed. A National Semiconductor™ non-inverting LM675 operational amplifier (op-amp) used in the circuit [3] shown in Figure 2-16 takes the voltage from the computer as an input and controls the power supplied by a regulated 20 V power supply in order to provide a precisely controlled signal at power levels up to 8 W to the resistance heater.

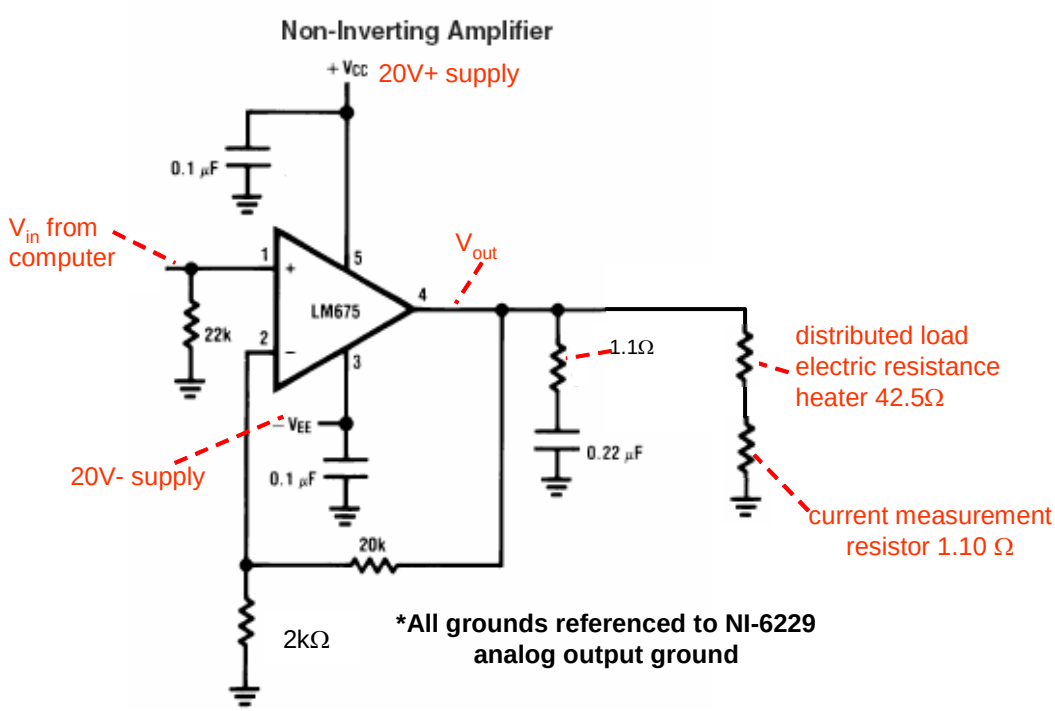

Figure 2-16: Op-amp schematic for providing computer controlled dissipative heat load.

A fan cooled op-amp circuit was constructed for the distributed load heaters; the dissipated power for the heater ($\dot{q}_{DL}$) is calculated as:

$$\dot{q}_{DL} = I^2 R_{heater} \tag{2.1}$$

where I is the current through the heater (calculated by measuring the voltage across the relatively small shunt resistor), and R_{heater} is the measured heater resistance. The distributed load heater resistance is calculated as 42.5 ± 0.1 Ω, and the current can be measured with approximately 1.5% accuracy, therefore the dissipated power is known within ± 3%. Figure

2-17 shows the calculated heater dissipated power as a function of the input voltage from the DAQ card.

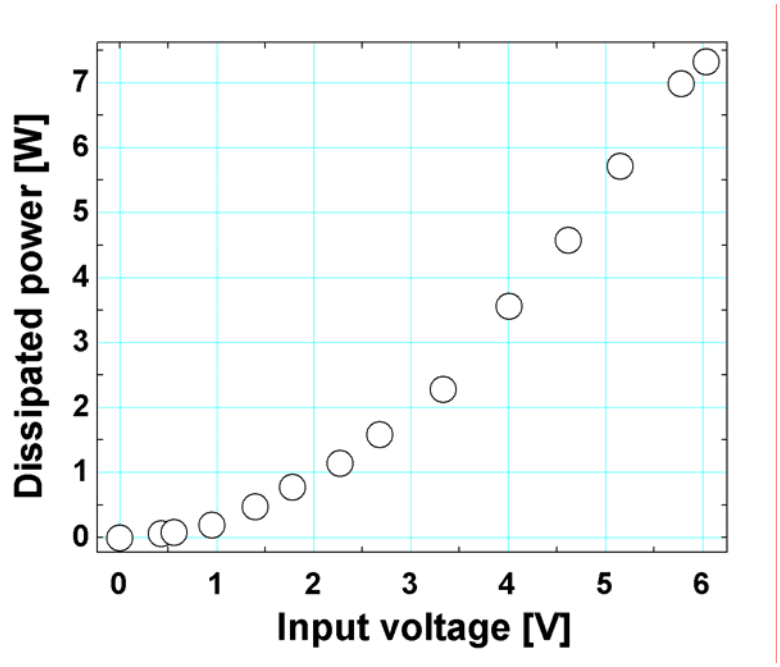

Figure 2-17: Calculated power supplied to the resistance heater vs. input voltage for the op-amp power supply circuit

2.7 References

1. Skye, H.M., Hoch, D.W., Nellis, G.F., Klein, S.A, Maddocks, J.R., Roberts, T. and Davis, T., “Rectified Continuous flow loop for the thermal management of large structures”, in *Advances in Cryogenic Engineering* 51B, edited by J.G. Weisland, II, et al, American Institute of Physics, New York, 2006, pp 1809-1816.

2. Diab, A. K., Nellis, G. F., Maddocks, J. R., and Yarbrough, S., "Development of a Rectifying Interface for a Hybrid Pulse-Tube/Reverse-Brayton Cryocooler," in *Advances in Cryogenic Engineering* 49B, edited by J. Waynert et al., American Institute of Physics, New York, 2004, pp. 1777-1782.

3. National semiconductor http://www.national.com/pf/LM/LM675.html#datasheet

3 Experimental Data - Steady State and Uncontrolled Transient Behavior

The steady state performance and transient behavior of the Pulse Tube Rectifying Interface (PT/RI) were characterized using the experimental apparatus described in Section 2. The steady state performance is quantified with load curves, which show the cold head and interface temperatures relative to thermal load applied via the electric heaters. A parametric study of the PT/RI system compares system performance relative to the primary control variables: compressor stroke and cooling loop mass flow. This study shows that the refrigeration performance of the system decreases with decreased compressor stroke and increased cooling loop mass flow. The results from the parametric study are used in part to develop the thermal model discussed in Sections 4 and 5.

Transient dynamics of the PT/RI system are also characterized through a series of tests including rapid changes in stroke, cooling loop mass flow, and thermal load. These tests are used to refine estimates of the interface and cold head thermal capacitances, and also to demonstrate the additional interface temperature control capability afforded with the addition of the cooling loop valve.

3.1 Cool Down Curve

During cool down from room temperature, the flow valve is adjusted to its nominal ½ open position in order to provide a substantial flow through the interface loop and therefore cool down the distributed components. The compressor stroke is set to 100% in order to accelerate the cool down process. The temperature of the PT/RI system exhibits an approximately exponential approach to a steady state temperature; cool down near room temperature is rapid as the cooling power greatly exceeds the system losses while the eventual approach to a steady state, no-load

condition is quite slow. During the entire cool down process, the system temperatures at the high and low pressure buffers, the cold head, and the interface (distributed load) remain within a few degrees of one another. The cool down from room temperature to a nominal operation temperature (140 K) typically requires between two and three hours. Figure 3-1 shows the measured temperatures as a function of time for a typical cool down process.

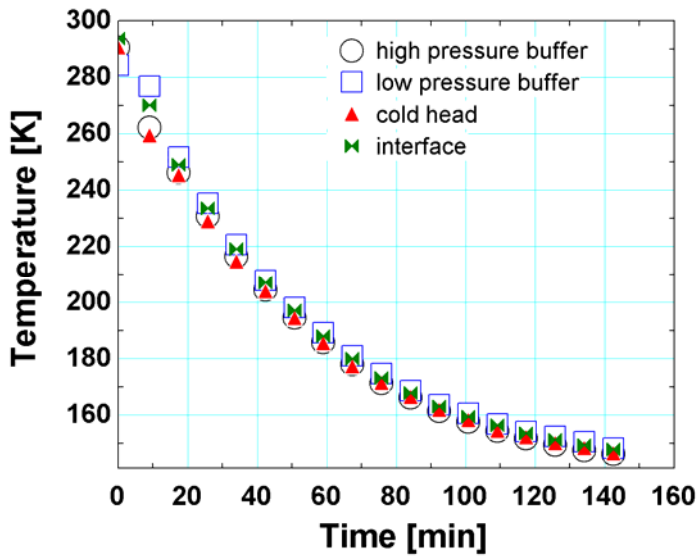

Figure 3-1: **Typical cool down from room temperature for the PT/RI system. The components in the loop are at nearly the same temperature during the cool down process.**

3.2 Calculation of Stroke

The compressor backside pressure is measured using the differential pressure gage shown in Figure 2-3 and used to infer the compressor stroke. The compressor is at full stroke when the piston hits the stops, a condition that can be determined with some precision due to the associated noise. The peak-to-peak pressure is measured at this full stroke condition. The stroke at other conditions is calculated by assuming that stroke and peak-to-peak pressure are linearly related. Figure 3-2 shows an example of the compressor backside pressure as a function of time at 100% and 80% stroke. Note that during typical operation, the compressor gradually increases

the PT/RI internal pressure (on the order of a few 50 kPa [3 psi] per hour) while the pressure after the isolation valve remains constant as it is isolated from any compression/heating. Therefore, the differential pressure measurement, which compares the PT/RI internal pressure just behind the compressor piston to the pressure in the isolated section, exhibits a gradual increase in DC offset.

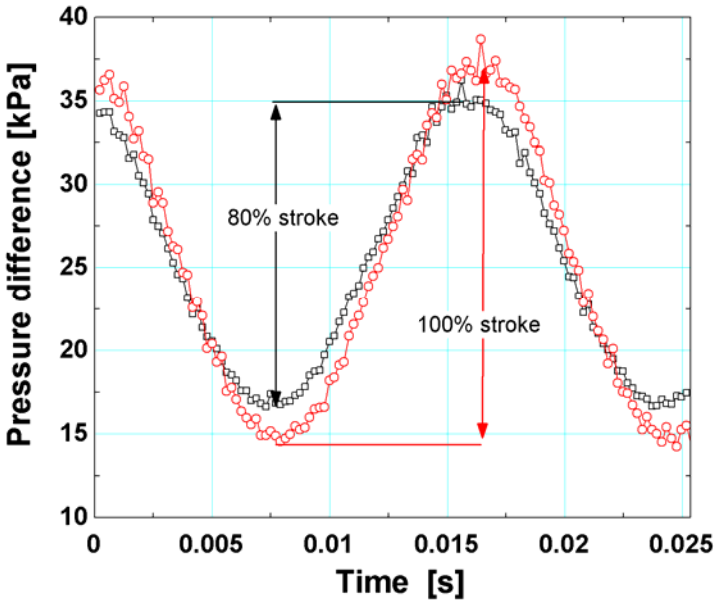

Figure 3-2: Compressor backside pressure measured as a function of time at 80% and 100% stroke (valve ¼ open, 5.0 W distributed load).

3.3 Steady State Data – Cooling Loop Valve Closed

Pulse tube refrigerators without a rectifying cooling loop will typically provide cooling through direct thermal contact with the cold end of the pulse tube (i.e., the cold head). For distributed or spatially separated loads, a secondary fluid flowing through a heat exchanger that is thermally interfaced with the cold head can be used. Alternatively, copper straps may be used to conduct heat between the loaded component and the pulse tube cold head. In order to compare the PT/RI system to pulse tube cryocoolers that are interfaced using these more conventional techniques, the flow valve was completely closed to eliminate the flow of helium through the cooling loop.

The performance of the system with the valve closed is subsequently compared to the performance of the system when the valve is opened (allowing flow through the loop) in order to quantify the performance reduction of the pulse tube due to the presence of the interface and its effect on the pulse tube flow and pressure. Performance is defined as the temperature of either the cold head or the interface for a given load; lower temperatures correspond to a higher performance.

Heat is applied to the cold head of the pulse tube using electrical energy dissipated in a resistor (the cold head heater) in order to simulate a cooling load; Figure 3-3 shows the load curves (the cold head heater power as a function of cold head temperature) for the closed valve condition with 80% and 100% compressor stroke. At 80% compressor stroke, the cold head is 7-10 K warmer than at 100% stroke for a given cold head thermal load.

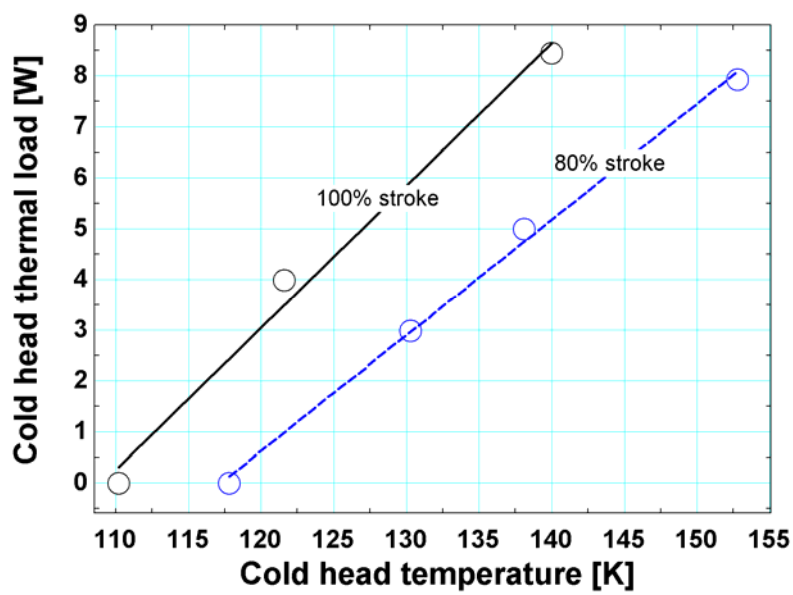

Figure 3-3: **Load curve measured for the PT/RI system with the flow control valve closed and 80% and 100% stroke.**

3.4 Steady State Data – Cooling Loop Valve Open

The flow resistance of the cooling loop is changed using the cooling loop valve shown in Figure 2-5. Decreasing the flow resistance (i.e., opening the valve) increases the mass flow through the cooling loop and also results in an increase in the pressure variation that is observed within the buffer volumes during each cycle as more mass is transferred from the high pressure to the low pressure volumes.

Figure 3-4 shows the semi-sinusoidal pressure waveforms measured in the pulse tube and high and low pressure buffer volumes for three valve settings (closed, ½ open, and ¼ open). Note that the higher frequency fluctuations observed in the measured pressure within the buffer volumes during a cycle is related to the dynamics of the small stainless steel tube that connects the pressure sensor to the buffers. The tube length is such that small compression and expansion waves travel through the tube; these waves distort the signal measured by the pressure sensor. Therefore, these fluctuations are not actual phenomena experienced within the buffer volumes; the actual pressure waveforms would be better represented by a straight line drawn through the midline of the buffer volume pressure trace (as shown in Figure 3-4).

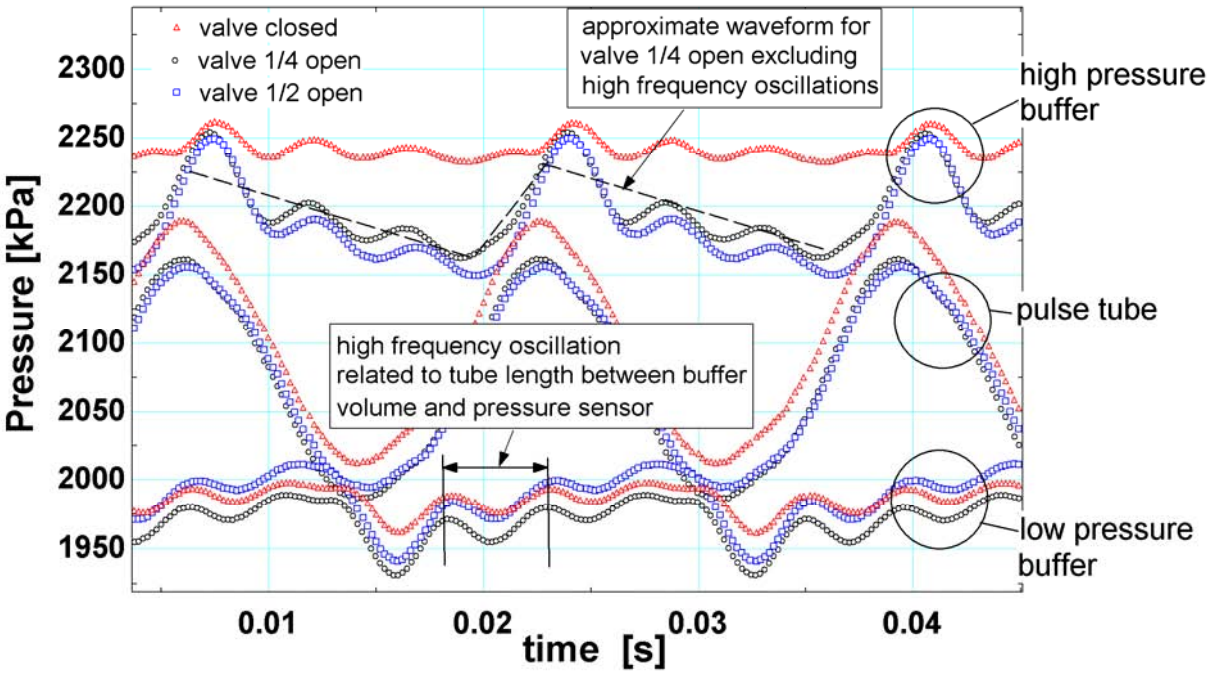

Figure 3-4: Pressure waveforms in the pulse tube and high and low pressure buffer volumes for three different valve settings: ½ open, ¼ open, and closed.

Figure 3-5 (a) and (b) illustrate the cold head heater power as a function of the cold head temperature for the three valve settings (½ open, ¼ open, and closed) at 100% and 80% stroke, respectively. Figure 3-5 shows that the performance of the pulse tube refrigerator at both 80% and 100% stroke settings is degraded as the cooling loop valve is opened. This degradation is related to the mass flow that is processed by the regenerator and compressor, but diverted from the system at the cold end to flow through the cooling loop without contributing to the cooling effect. Furthermore, the amplitude of the pressure oscillation is reduced by the diversion of this mass flow rate through the cooling loop. Note that because the heat is applied to the cold head for all three valve settings, these figures represent a direct performance comparison of conventional, closed cycle pulse tube cryocooler (i.e. the cooling loop valve is closed to prevent helium flow in the cooling loop), and the PT\RI system with helium flowing through the cooling loop shown in Figure 3-6.

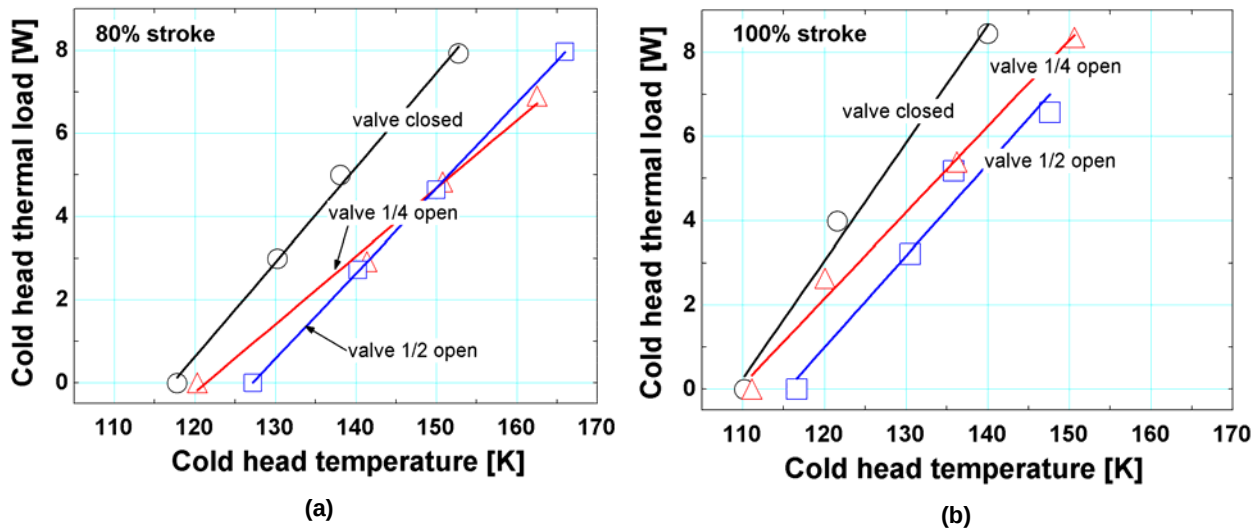

Figure 3-5: **Load curves for the PTRI system with heat applied at the cold head. Three valve settings (¼ open, ½ open, and closed) are compared at (a) 80% stroke and (b) 100% stroke.**

The distributed load heater was also used to create a set of load curves showing the distributed cooling power as a function of the distributed load temperature under several stroke and cooling loop valve operating points. In an applied setting, the PT/RI system would accept a load at the distributed load interface. Therefore, the distributed load curves are more meaningful than the cold head heater load curves for the design and demonstration of the PT/RI system. The data from the distributed load curves are used to create the PT/RI transient model described subsequently in section 4.

Figure 3-6 compares the load curves (distributed load as a function of distributed load temperature) for (a) 80% and (b) 100% stroke with ½ and ¼ open valve settings. The distributed load curves are also compared to the cold head thermal load curves with the cooling loop valve closed (from Figure 3-3) in order to show the performance penalty that is associated with the use of the rectifying interface for thermal integration. Figure 3-6 shows the temperature difference between the cold head and the distributed load, which represents the temperature rise of the

helium as it accepts the distributed thermal load at the interface. At 80% compressor stroke, the helium temperature rises 8 K and 15 K for the ½ and ¼ open valve settings at 4W distributed load. Similarly, the helium temperature in the loop rises 10 K and 17 K for the ½ and ¼ open valve settings at 4W distributed load with 100 % stroke.

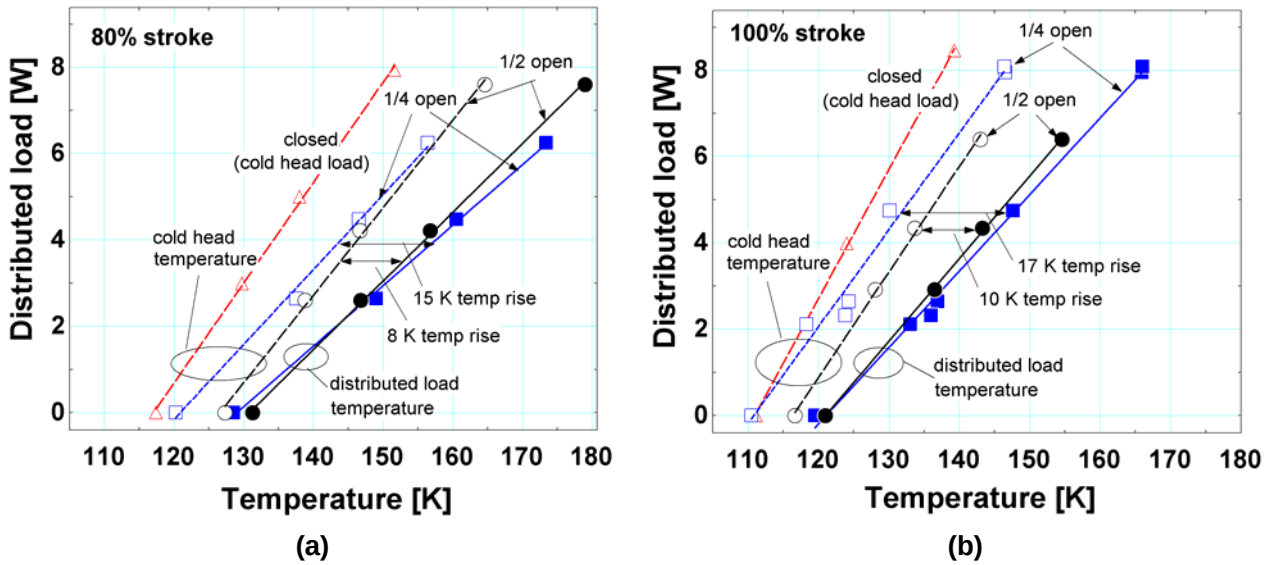

Figure 3-6: Load curves for the interface heater comparing settings of stroke (80% and 100%) and valve setting (½ open and ¼ open).

3.5 Transient Data

The transient system response shows how the temperature in the system changes as control variables, such as stroke and valve resistance, and external variables, such as heat load are adjusted. Temperature data for the PT/RI system were recorded for step changes in stroke, cooling loop valve resistance, and interface load. Once the change was made, the system was allowed to reach a steady state.

Figure 3-7 (a) shows measured response of the system with respect to time when the compressor stroke is adjusted approximately instantaneously from 80% to 100% stroke. As expected, the temperature of the cold head decreases due to the increase in refrigeration capacity associated

with the increased stroke. The disturbance is applied directly to the relatively massive cold head and therefore the response is slow; the response can be characterized by a time constant of several thousand seconds due to the large thermal mass of the cold head. The interface temperature follows the cold head and is almost exactly offset, indicating that the flow through the distributed load was not changed significantly. Figure 3-7 (b) shows the same transient response for an increase in compressor stroke expressed in terms of a dimensionless time ΨC which characterizes the cold head in terms of the specific parameters that govern its thermal behavior.

$$\psi_C = \frac{t}{C_C \Big/ \left(V_{swept} \frac{1}{\tau_{comp}} \rho_{comp} c_{p,comp} \right)} \tag{3.1}$$

where t is time, C_C is the cold head thermal mass, V_{swept} is the compressor swept volume, τ_{comp} is the compressor period, ρcomp is the average density of helium in the compressor, and cp,comp is the average specific heat of helium at a nominal compressor temperature. The specific values of the parameters used in Eq. (3.1) to calculate the cold head dimensionless time are listed in Table 3-3. The calculation of the cold head thermal mass value is discussed in the transient model section (section 4.4).

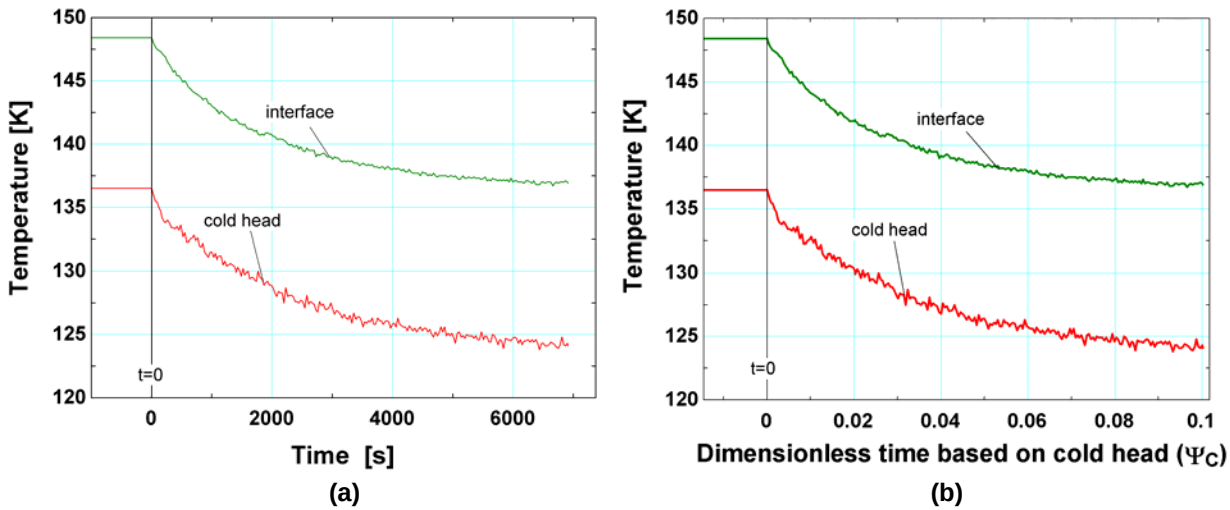

Figure 3-7: Transient temperature data for a step change in stroke from 80% to 100% (interface valve= ¼ open, interface heat = 2.64 W) in terms of (a) time and (b) cold head dimensionless time

Figure 3-8 (a), (b1), and (b2) show the system response when the distributed load is decreased dramatically (at time = 0, the distributed load at the interface is adjusted from 8 W to 3 W). The disturbance that drives Figure 3-8 is applied directly to the distributed load interface; the short and long term responses of the system are very different (note the broken time axis in Figure 3-8 (a)). In the short term, the interface temperature drops rapidly (in a few 10's of seconds) while the cold head temperature remains essentially unchanged. In the long term, the cold head temperature eventually decreases (in 1000's of seconds). The different time scale temperature behaviors are caused by the relatively small and large thermal masses of the interface and cold head, respectively. It is useful to characterize the distributed load temperature change in terms of an appropriately defined dimensionless time, Ψ_I.

$$\Psi_I = \frac{t}{C_I / \dot{m}_{I,nom}\, c_p} \tag{3.2}$$

where C_I is the interface thermal mass, $\dot{m}_{I,nom}$ is a nominal interface mass flow, and c_p is the constant pressure specific heat of helium at nominal loop temperatures. Parameters used to calculate the interface dimensionless time using Eq. (3.2) are listed in

Table 3-3. Figure 3-8 (b1) and (b2) show the same transient response as Figure 3-8(a), but are expressed in terms of interface and cold head dimensionless times, respectively. The rapid distributed load interface temperature decrease in the first 150 seconds is characterized in terms of Ψ_I in Figure 3-8 (b1). The gradual temperature change of the cold head in terms of the cold head dimensionless time Ψ_I is shown in Figure 3-8 (b2). Note that discussion of the calculation of the C_I, value is found in transient model section (section 4.4).

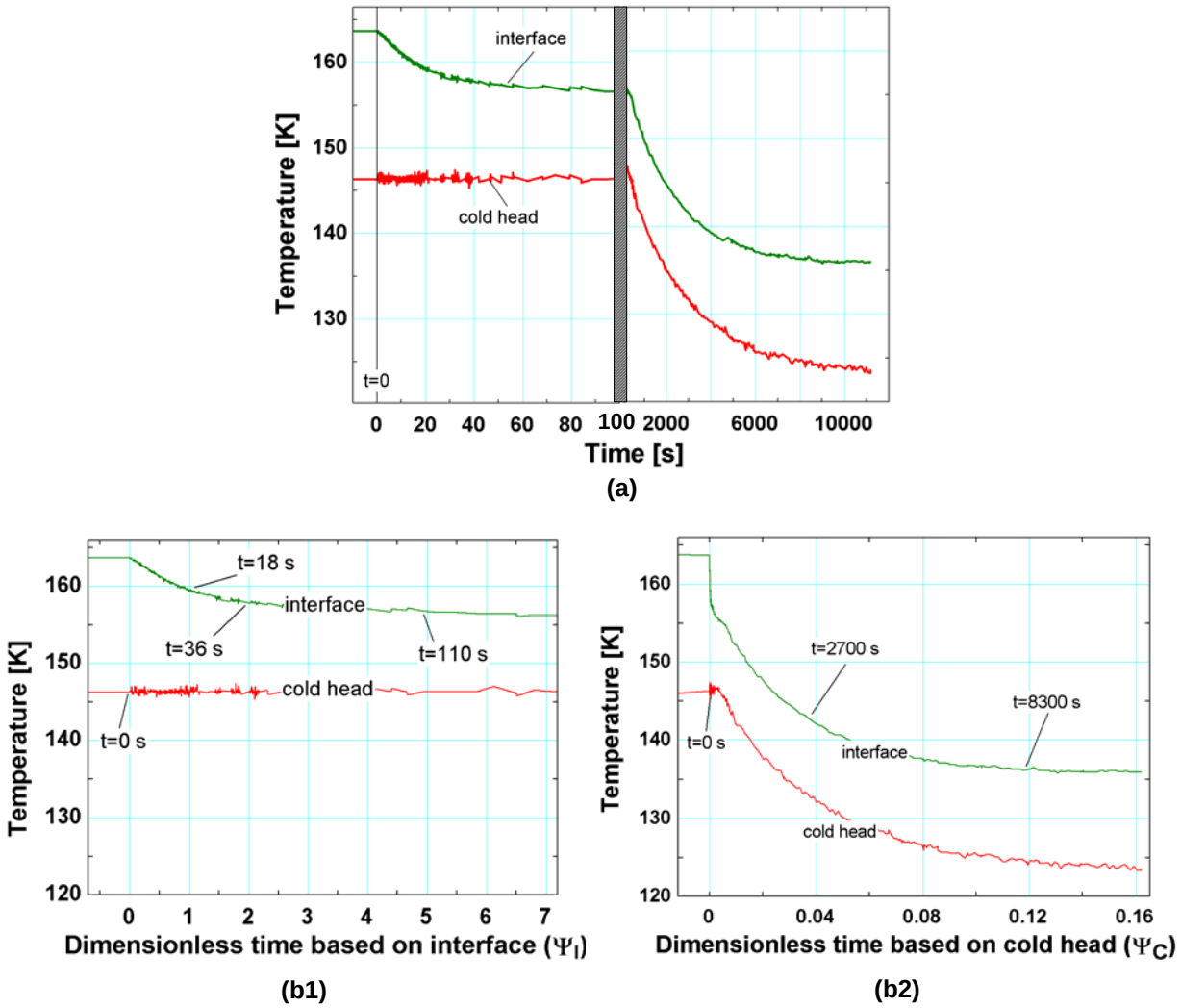

Figure 3-8: **Transient response of PT/RI system to a step change in interface load from 7.95 W to 2.32 W (stroke = 100%, valve = ¼ open) in terms of (a) time, (b1) interface dimensionless time (first 150s), and (b2) cold head dimensionless time (complete response).**

The transient response graphs (Figure 3-7 (b) and Figure 3-8 (b1) and (b2)) shown in terms of the dimensionless time illustrate that the key parameters that affect the PT/RI transient response are characterized by the dimensionless times Ψ_I and Ψ_{CH}. Figure 3-7 (b) and Figure 3-8 (b2), show similar long term responses to thermal perturbations (i.e refrigeration, distributed load) in terms of Ψ_{CH}. Therefore, the cold head dimensionless time defined in Eq. **Error! Reference source not found.** is an appropriate time variable for characterizing changes

which result in long-term temperature fluctuations. Figure 3-8 (b1) shows the short term transient response expressed in terms of Ψ_I dies out after $\Psi_I =$ 4 to 6. The interface dimensionless time is therefore based on a time constant that adequately captures the parameters governing the short-term, first-order thermal response.

Understanding the system in terms of these dimensionless times is useful from a design perspective in that the parameters which govern the short and long term temperature fluctuations have been identified and therefore can be selected in order to achieve a certain system performance. The thermal behavior of a different PT\RI system with different operating parameters can be predicted approximately based on the dimensionless temperature responses shown in Figure 3-7 and Figure 3-8. The designer can subsequently manipulate the design variables to make the different PT\RI system meet a set of desired transient temperature performance characteristics.

The most interesting transient measurements are shown in Figure 3-9; the valve is opened suddenly (from ¼ to ½ open at time = 0). In the short term, the interface temperature drops quickly because a larger flow of cold gas is pulled from the cold head. However, the increased flow ultimately causes the cold head temperature to rise (recall that opening the valve degrades the pulse tube performance, as shown previously by Figure 3-5 in section 3.4). Therefore, over a longer term (on the order of 1000's of seconds), both the interface and the cold head temperature rise. Figure 3-9 shows that by adjusting the valve it is possible to affect the interface temperature over a time scale that is on the same order as the time scale associated with the interface adjusting to changes in the distributed load. This is convenient, as it suggests that modulation of the flow control valve represents a more powerful lever for controlling the short-term

temperature fluctuations than would be available through control of the refrigeration system itself (e.g., through changing the stroke or frequency of the compressor).

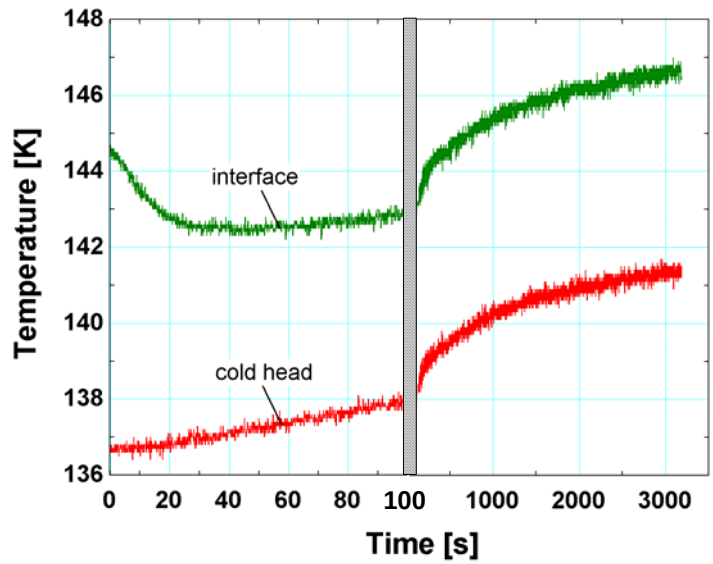

Figure 3-9: Transient response of PT/RI system for a step change in interface resistance. (Stroke=100%, interface distributed thermal load =2.42 W).

3.6 Calculation of Mass Flow Rate and Parasitic Loss

The mass flow rate through the rectified cooling loop is primarily controlled by the compressor stroke and cooling loop valve resistance. The interface valve resistance is governed by the position of the valve. The mass flow is not directly measured, but is calculated using an energy balance on the distribution loop as shown in Eq. (3-3). Helium enters the loop at the high pressure buffer temperature ($T_{B,HP}$) and exits at the low pressure buffer temperature ($T_{B,LP}$). These temperature measurements are made by sensors that are embedded in the flow stream and therefore the difference in these temperatures is the result of a combination of the heat added by the interface electric heater ($\dot{q}_I$) as well as any parasitic losses in the loop ($\dot{q}_p$).

$$\dot{q}_I = \dot{m}\left[c_p\left(T_{B,LP} - T_{B,HP}\right)\right] - \dot{q}_p \tag{3.3}$$

In Eq.(3.3), $\dot{m}$ is the helium mass flow rate in the loop, and c_p is the constant pressure specific heat of helium that is obtained at the nominal charge pressure of 2170 kPa (300 psig) and the average temperature between the buffer volumes. The specific heat of the helium is essentially constant in the temperature and pressure ranges used in this experiment, so a constant specific heat (5.2 kJ/kg-K) is used in the energy balance calculation. The helium mass flow is calculated by plotting the interface load as a function of $c_p\left(T_{LPB}\text{-}T_{LPB}\right)$, as shown in Figure 3-10; the data transformed in this manner are nearly linear and they can be fit using linear regression. The slope of the best-fit line is the mass flow rate and the intercept represents the negative value of the parasitic load. The results of this calculation for the various data sets are summarized in Table 3-1; the calculated parasitic ranges between 5 and 10 W.

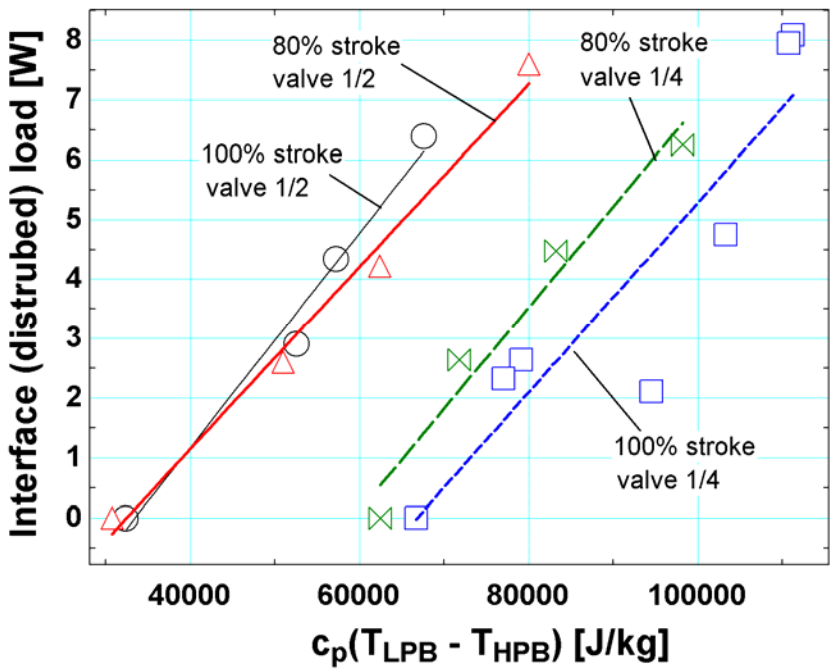

Figure 3-10: **Interface load curves plotted vs. $c_p(T_{B,LP}-T_{B,HP})$ for two stroke and valve settings (stroke 80%, 100% and valve ½ open, ¼ open).**

Table 3-1: **Experimental Data - Steady State and Uncontrolled Transient Behavior: Summary of mass flow and parasitic heat loss calculations using Eq. (3-3) and Figure 3-10.**

Stroke	Valve setting	Slope ($\dot{m}$)	Parasitic ($\dot{q}_p$)
100%	½ open	0.18 g/s	6.0 W
100%	¼ open	0.16 g/s	10.6 W
80%	½ open	0.15 g/s	5.0 W
80%	¼ open	0.14 g/s*	10.1 W

*Note: the no load data point was omitted for the 80% stroke ¼ open valve setting. See Appendix A for details.

3.7 Dimensionless Interface Valve Resistance

The modeling effort, described in Chapter 4, is used to predict the PT/RI performance as a function of several variables, including the non-dimensional interface resistance (R_I). The interface resistance characterizes the flow resistance through the cooling loop, and it is controlled

with the stainless steel bellows valve. The calculation of the dimensionless resistance (R_I) is based on the dimensional interface resistance (r_I), which is calculated using Eq. (3.4).

$$r_I = \frac{avg(p_{B,HP} - p_{B,LP})}{\dot{m}} \tag{3.4}$$

where $avg(p_{B,HP} - p_{B,LP})$ is the average difference between the buffer pressures during one compressor cycle. The non-dimensional interface resistance (R_I) is calculated according to:

$$R_I = \frac{r_I \, V_{swept}}{\tau \, Rg \, T_H} \tag{3-5}$$

where V_{swept} is the volume swept by the compressor piston at full stroke, τ is the compressor period, Rg is the ideal gas constant for helium, and T_H is the heat rejection temperature (hot heat exchanger temperature). The heat rejection temperature changes very little during the experiment and it is assumed to be constant at 293 K for these calculations.

The average non-dimensional interface resistance values for each valve and stroke setting are summarized in the first four rows of Table 3-2. Note that for modeling purposes the, the dimensionless valve resistance for a given valve position is assumed to be nominally equivalent at 80% and 100% stroke settings. Therefore, the model developed in Chapter 4 uses a dimensionless resistance for each valve setting calculated as the average resistance for the two stroke settings. These dimensionless valve resistances are shown in the last two rows of Table 3-2. The averages are computed using the complete set of experimental data shown in Table 3-4.

Table 3-2: Summary of average dimensionless interface flow resistance for nominal operation points.

Stroke [%]	Valve fraction open	Dimensionless interface flow resistance (R_I)
100	¼	**2.65**
100	½	**2.16**
80	¼	**2.78**
80	½	**2.29**
average (80, 100)	¼	**2.70**
average (80, 100)	½	**2.23**

Table 3-3: Parameters used to calculate the interface resistance and cold head/interface dimensionless times.

Parameter	Value
Compressor swept volume (V_{swept})	1.83×10^{-5} m^3
Compressor period (τ)	1/60 s
Ideal gas constant for helium (R_g)	2.077 kJ/kg-K
Heat rejection temperature (T_H)	285 K
Cold head thermal capacitance (C_C)	725 J/K
Interface thermal capacitance (C_I)	15 J/K
Helium density in compressor (ρ_{comp})	7.295 kg/m^3
Helium specific heat in compressor ($c_{p,comp}$)	5.191 kJ/kg-K
Helium specific heat in cooling loop (c_p)	5.202 kJ/kg-K
Nominal cooling loop mass flow ($\dot{m}_{I,nom}$)	0.16 g/s

Table 3-4: Interface resistance calculations for all interface load data

Stroke [%]	Valve	Distributed Load ($\dot{q}_I$)	Average pressure difference between buffers	Mass flow ($\dot{m}$)	Interface resistance (r_I)	Nondimensional interface flow resistance (R_I)
100	¼ open	0 W	231 kPa	0.16 g/s	1.46E+09 pa-s/kg	2.706
100	¼ open	3 W	235 kPa	0.16 g/s	1.48E+09 pa-s/kg	2.75
100	¼ open	5 W	231 kPa	0.16 g/s	1.46E+09 pa-s/kg	2.704
100	¼ open	8 W	217 kPa	0.16 g/s	1.37E+09 pa-s/kg	2.542
100	¼ open	3 W	228 kPa	0.16 g/s	1.44E+09 pa-s/kg	2.672
100	¼ open	3 W	225 kPa	0.16 g/s	1.42E+09 pa-s/kg	2.637
100	¼ open	8 W	220 kPa	0.16 g/s	1.39E+09 pa-s/kg	2.574
100	½ open	0 W	215 kPa	0.18 g/s	1.20E+09 pa-s/kg	2.233
100	½ open	3 W	211 kPa	0.18 g/s	1.18E+09 pa-s/kg	2.187
100	½ open	5 W	207 kPa	0.18 g/s	1.15E+09 pa-s/kg	2.144
100	½ open	7 W	203 kPa	0.18 g/s	1.13E+09 pa-s/kg	2.103
80	¼ open	0 W	213 kPa	0.14 g/s	1.57E+09 pa-s/kg	2.34
80	¼ open	3 W	204 kPa	0.14 g/s	1.51E+09 pa-s/kg	2.241
80	¼ open	5 W	198 kPa	0.14 g/s	1.47E+09 pa-s/kg	2.178
80	¼ open	8 W	195 kPa	0.14 g/s	1.44E+09 pa-s/kg	2.144
80	½ open	0 W	190 kPa	0.15 g/s	1.25E+09 pa-s/kg	1.856
80	½ open	3 W	189 kPa	0.15 g/s	1.24E+09 pa-s/kg	1.842
80	½ open	5 W	187 kPa	0.15 g/s	1.23E+09 pa-s/kg	1.825
80	½ open	8 W	1845 kPa	0.15 g/s	1.21E+09 pa-s/kg	1.795

4 Steady State and Transient PT\RI Thermal Model: Development and Verification

The transient model of the Pulse Tube Rectifying Interface (PT/RI) is shown schematically in Figure 4-1. The model includes the cold end of the pulse tube and the distributed cooling loop. The semi-empirical model is created in SIMULINK™ and it predicts the steady and transient thermal behavior of the PT/RI. The cold end of the pulse tube is modeled as a single thermal capacitance with an assumed uniform temperature equal to that of the cold head. Note that in the experimental setup, the buffer volumes have good thermal contact with the cold head, so all three components are lumped together as one thermal capacitance (C_C). The refrigeration power of the pulse tube ($\dot{q}_{pt}$) and mass flow rate through the distributed loop are a function of the resistance of the interface which is quantified by a dimensionless interface resistance (R_I) and related to the position of an active control valve in the loop (the position of the control valve determines the equivalent flow area of the valve), the cold head temperature (T_C), and the fraction of full stroke (f) that the compressor is operating at. The load interface represents the interface between the distributed load (e.g., a detector or structure) and the fluid in the cooling loop; the rate of heat transfer to the distributed loop is $\dot{q}_I$. The interface is modeled as a thermal capacitance (C_I) with a uniform temperature equal to the interface temperature (T_I). The heat transfer between the interface and the fluid is assumed to be sufficient such that the fluid exits the interface at the interface temperature.

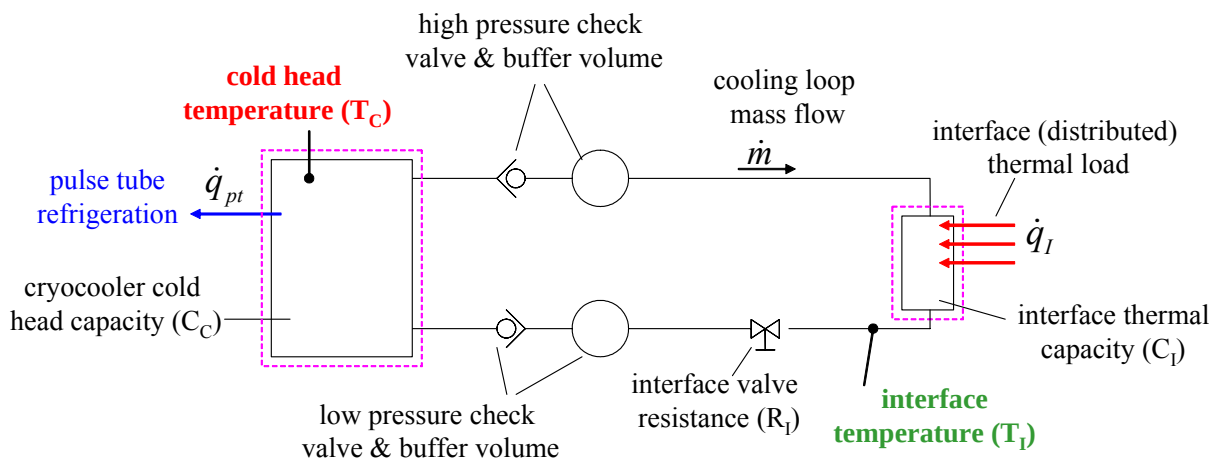

Figure 4-1: **Schematic of the transient model of the PT/RI system. The buffer volumes and check valves are not part of the model, but are shown for clarity.**

4.1 Governing Equations for Transient PT/RI Model

Energy balances on the systems that represent the cold end of the pulse tube and the interface are used to develop the state equations that define the system model. The state equations predict the rate of change of the temperatures (T_C and T_I) given their instantaneous values as well as other system inputs such as the current loads. Therefore, the transient behavior of the system can be predicted for a given initial state (i.e., initial interface and cold end temperature) together with the time variation of the system inputs (e.g., the stroke, interface resistance, heat loads, etc.) by integrating the state equations forward in time using a SIMULINK™ [1] model. Nominal parameter values used in the transient thermal model are listed in Table 4-3.

Figure 4-2 illustrates the cold end of the pulse tube and the associated energy transfers. The cold head system is exposed to the refrigeration potential of the pulse tube (i.e., its cooling capacity generated by the expansion of the gas in the pulse tube); note that $\dot{q}_{pt}$ is a net refrigeration potential that combines an applied heat load generated by an electric heater ($\dot{q}_{elec}$) with the parasitic losses on the cold head ($\dot{q}_p$). The development of the applied heat load and parasitic loss functions are discussed in Section 4.2.

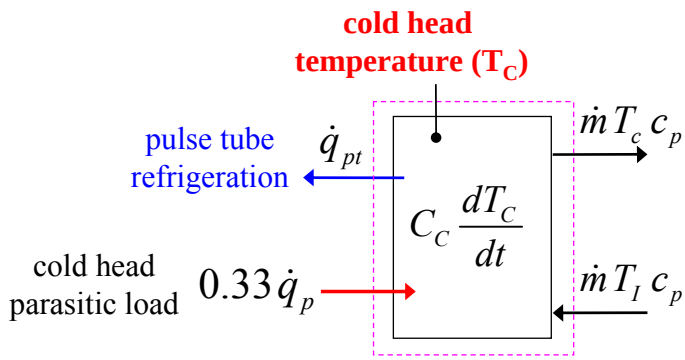

Figure 4-2: **The cold head of the pulse tube with its energy transfers including refrigeration power, thermal capacitance, and enthalpy flows.**

The energy balance on the cold end of the pulse tube provides the first state equation:

$$\frac{dT_C}{dt} = \frac{\dot{m}\,c_p\,(T_I - T_C) + 0.33\,\dot{q}_p - \dot{q}_{pt}}{C_C} \tag{4.1}$$

where t is time, c_P is the constant pressure specific heat capacity of helium, $\dot{m}$ is the mass flow through the cooling loop, and represents the fraction of the total parasitic heat load after the interface which effectively acts on the cold head. Further discussion of the parasitic load distribution is in Section 4.2. The value of C_C is determined based on comparing transient experimental data with the model in Section 4.4; this value is nominally consistent with computing the total thermal mass of the cold head based on its geometry and material properties. The SIMULINK™ cold head transient model that captures the thermal behavior predicted by Eq. (4.1) is shown in Figure 4-3.

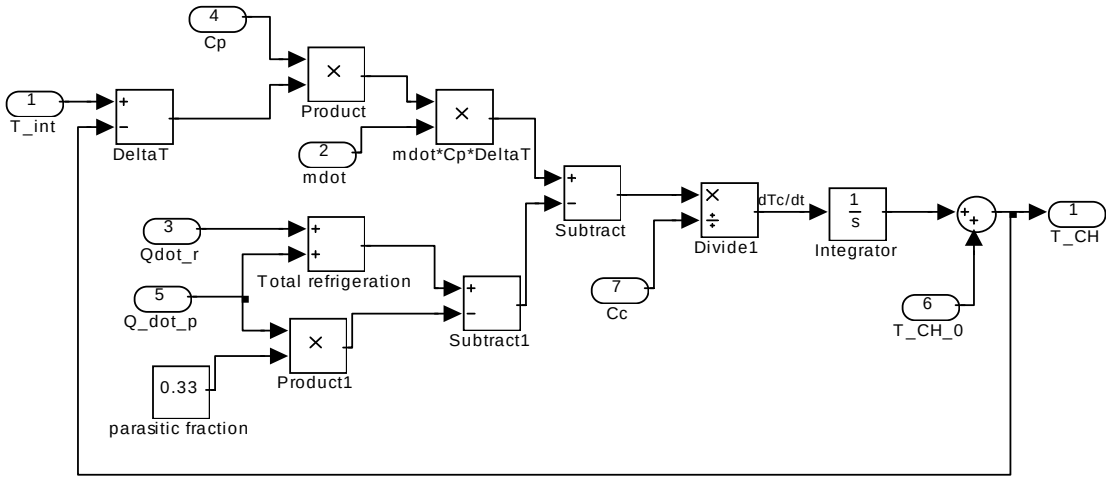

Figure 4-3: SIMULINK subsystem code for the differential equation that governs the cold head temperature, Eq. (4-1).

An energy balance on the interface is shown in Figure 4-4, with the associated energy and enthalpy flows. The transient thermal model combines the state equations governing the cold head and the interface, and integrates these equations forward in time to predict the steady state and transient thermal behavior of the PT/RI system.

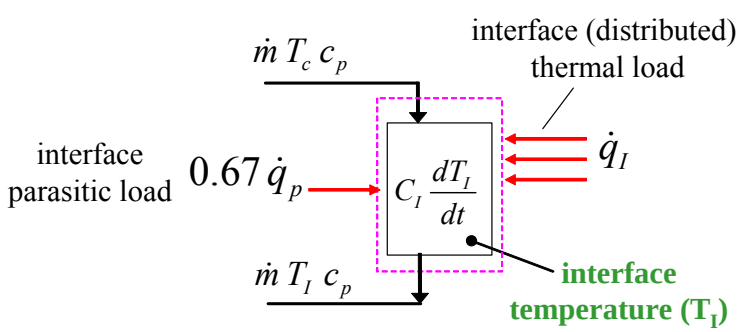

Figure 4-4: Model components for the distributed load interface including heat load, thermal capacitance, and enthalpy flows.

An energy balance on the interface provides the second state equation:

$$\frac{dT_I}{dt} = \frac{\dot{q}_I + 0.67\dot{q}_p - \dot{m}\, c_p (T_I - T_c)}{C_I} \qquad (4.2)$$

where $0.67\dot{q}_p$ represents fraction of the total parasitic heat load between the cold head and the interface, which effectively acts on the interface. Further discussion of the parasitic heat load distribution is in Section 4.2. The interface thermal capacitance is determined by comparing the transient experimental data with the model in Section 4.4. In the experimental setup, the interface thermal capacitance is much smaller than the cold head thermal capacitance. The model incorporates the largely differing thermal capacitances, and therefore is expected to show the experimentally observed (Section 3.5) time scale separation for temperature response to thermal disturbances at the cold head and interface. Figure 4-5 shows the SIMULINK™ code used to predict the interface (distributed load) temperature response.

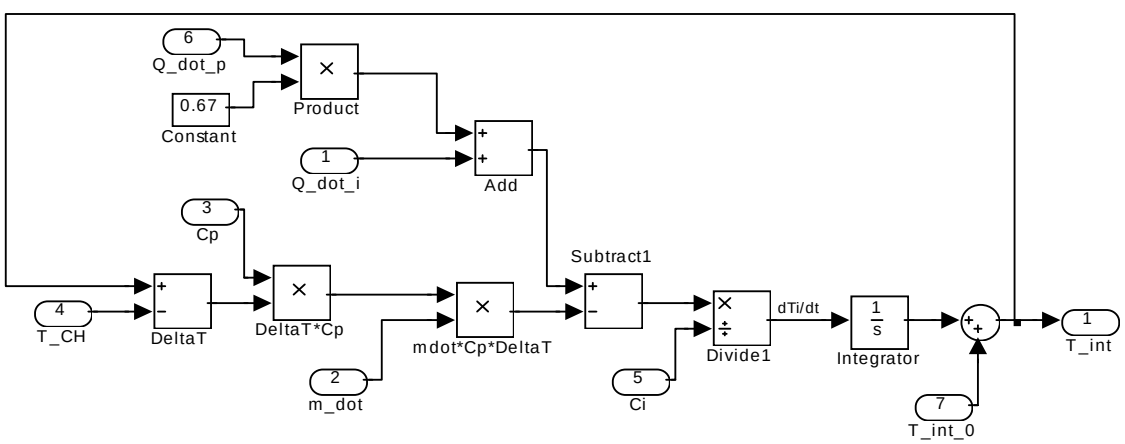

Figure 4-5: SIMULINK subsystem code for the differential equation that governs the interface temperature, Eq. (4-2).

4.2 Parasitic Heat, Mass Flow, and Refrigeration Power Empirical Models

Functional representations of the mass flow rate and pulse tube refrigeration potential are required for the transient model. Previously it was pointed out in Chapter 3.6 that there appears to be a 5-10 W parasitic heat input to the rectified cooling loop even in the absence of applied electrical power; this heat input cannot be explained completely and it may be an artifact of a

bias in the measurements. However, it is necessary to characterize this parasitic heat load in order to utilize the steady state experimental data to develop driving functions for the transient model.

Note that the resistance values for the ¼ and ½ open valve settings used to develop the mass flow, refrigeration, and parasitic heat functions are the average dimensionless resistance values at 80% and 100% stroke (from Table 3-3, average R_I with valve ¼ open = 2.70 , with valve ½ open R_I = 2.23).

The parasitic losses listed in Table 3-1 represent the average calculated parasitic loss for 80% and 100% stroke, as well as ½ and ¼ open cooling loop valve settings. These average parasitic losses have been fit to a linear function in order to facilitate calculation (via interpolation) of the parasitic load at stroke and valve settings other than those listed in Table 3-1. The calculated parasitic load dependence on stroke and valve resistance has no apparent physical explanation; however, it is characterized here so that the model captures all thermal phenomena associated with the experimental setup. The function is based on a linear best fit of the parasitic load as a function of interface resistance for both 80% and 100% stroke.

$$\dot{q}_p = j(f)R_I + k(f) \tag{4.3}$$

where j and k are coefficients with functional dependence on stroke (f), and are determined using a linear interpolation between the measured data points at 80% and 100% stroke. For example, the coefficient j is calculated according to:

$$j = j_{80} + \frac{\Delta j}{\Delta f}\,\Delta f \tag{4.4}$$

or:

$$j = j_{80} + \frac{j_{100} - j_{80}}{0.2}(f - 0.8) \tag{4.5}$$

where $\frac{\Delta j}{\Delta f}$ is the change in coefficient j as the stroke changes, Δf is the difference between the stroke and 80% stroke, and $j_{80\%}$ and $j_{100\%}$ are coefficients determined using experimental data at 80% and 100% stroke. Figure 4-6 and Table 4-1 summarize the results of the parasitic load function. The linear fit equations which are used to calculate the coefficients j and k for the parasitic are displayed in Figure 4-6. Note that the k coefficient as well as all other experimentally determined coefficients in this section with functional dependence on stroke (*c, d, e, n, g, h, j*) are calculated using the same method shown in Eqs. (4.4) and (4.5).

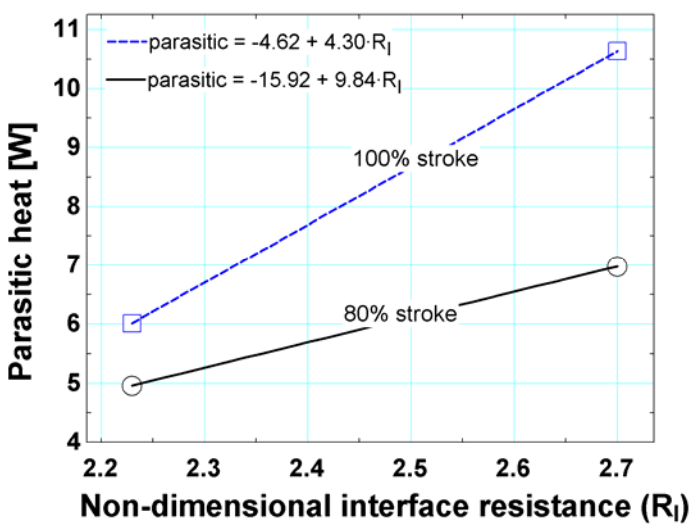

Figure 4-6: Parasitic heat load as a function of non-dimensional interface resistance at two values of stroke (80% and 100%). The results have been fit to linear equations (shown on graph) for use in the transient model.

The experimentally observed parasitic heat load occurs both prior to and after the interface (that is, the interface (distributed load) temperature under no load conditions lies between the low

pressure and high pressure buffer volumes temperatures). Therefore, the parasitic load is modeled by dividing it into two components; the distribution of the parasitic heat load is estimated using the temperature difference between the high pressure buffer and the interface at the no load condition in the experiment. The average parasitic distribution based on three no load operating points suggests that 67% of the parasitic is received prior to the interface and the remaining 33% occurs after the interface; Table 4-1 shows that this is fairly consistent among the no-load data points.

Table 4-1: Summary of data for calculating the distribution of the parasitic load.

Valve	Stroke (*f*)	Pre-interface load ($\dot{q}_1$)	Total parasitic ($\dot{q}_P$)	Parasitic before interface temperature measurement
¼	100 %	7.4 W	10.64 W	69.5 %
½	100 %	4.02 W	6.01 W	66.9 %
½	80 %	3.18 W	4.96 W	64.1 %

The mass flow rate through the distribution system also depends on stroke and interface resistance, but is not significantly influenced by the system temperature at nominal operating conditions. The mass flow rate (calculated based on experimental data as discussed previously) is also represented in the transient model by a linear best fit that is expressed in terms of the valve resistance. The coefficients to the linear regression (*g* and *h*) both depend on stroke. The coefficients have been computed for the two values of stroke that correspond to the experimental data and linear interpolation is used to estimate *g* and *h* at other values of the stroke.

$$\dot{m} = g(f)R_I + h(f) \tag{4.6}$$

Values for *g* and *h* for 80% and 100% stroke are summarized in Table 4-2; linear interpolation similar to the method used to calculate parasitic load is used to estimate the mass flow rates at other values of stroke. Figure 4-7 shows the mass flow rate as a function of non-dimensional

interface resistance for the two measured values of stroke. The values of the *g* and *h* coefficients at 80% and 100% stroke are shown in the figure.

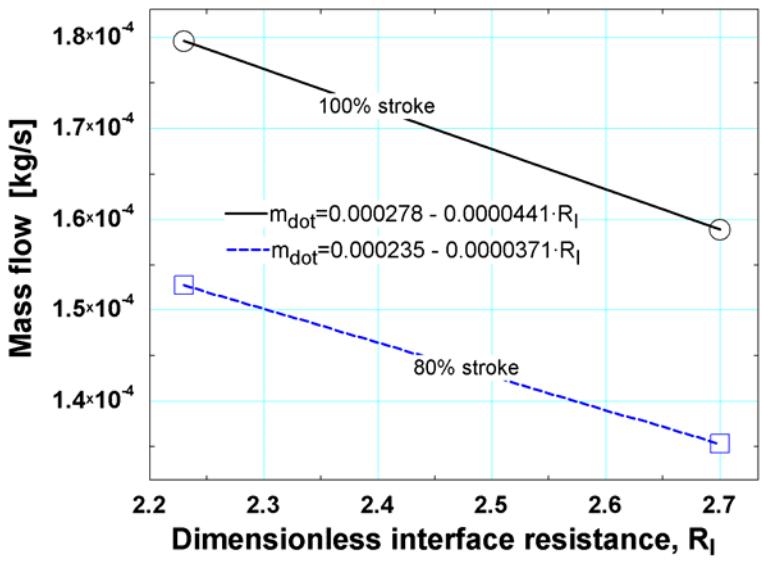

Figure 4-7: **Mass flow as a function of non-dimensional interface resistance at two values of stroke. The results have been fit to linear equations for use in the transient model. The coefficients *g* and *h* are calculated using these equations.**

The pulse tube refrigeration power as a function of cold head temperature was determined experimentally by applying heat to the cold head and allowing the system to reach a steady state. When the system reaches steady state, the refrigeration power provided by the pulse tube is taken to be equal to the sum of the electrical heat load applied to the cold head and the experimentally inferred parasitic load. Therefore, the calculation of the total pulse tube power ($\dot{q}_{pt}$) is the sum of the measured electrical input power ($\dot{q}_{elec}$) as well as the parasitic load ($\dot{q}_p$).

$$\dot{q}_{pt} = \dot{q}_{elec} + \dot{q}_P \tag{4.7}$$

At any given set of stroke and valve conditions, the applied electrical power is nearly linear with respect to the cold head temperature. Figure 4-8 shows the cold head load curves obtained with the cooling loop open (note that this includes the same data from Figure 3-5). Figure 4-8 also

includes the functions derived from a linear regression of the cold head load curves for each stroke and valve setting. Note that the cold head refrigeration curves will vary with other parameters, for example the charge pressure and frequency, however the effect of parameters other than stroke and valve resistance (which correspond to the two control parameters of interest) are beyond the scope of this study.

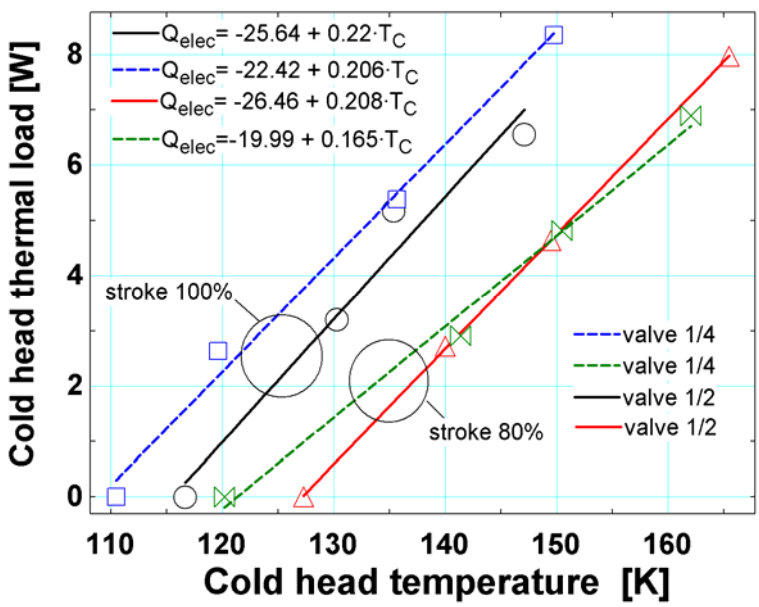

Figure 4-8: **Load curves for the PT\RI system with heat applied at the cold head and the cooling loop valve open. The linear fit functions are shown for two valve settings (¼ open, ½ open) and two stroke settings (80% stroke and 100% stroke). This figure is used in part to calculate the coefficients *a* and *b*.**

While each load curve shown in Figure 4-8 is nearly linear with respect to temperature, the refrigeration potential does depend on the stroke and non-dimensional interface resistance. Therefore, a general expression which describes the measured electrical input power to the cold head load as a function of cold head temperature is defined using a linear equation whose coefficients are dependant on stroke and valve resistance.

$$\dot{q}_{elec} = a\left(R_1, f\right)T_c + b\left(R_1, f\right) \tag{4.8}$$

where the coefficients a and b are determined as a function of R_I for 80% and 100% stroke; values of a and b for other values of stroke are linearly interpolated from these two.

The data points from the two stroke (80% and 100%) and two average dimensionless valve resistances (2.23 with valve ½ open and 2.70 with valve ¼ open) were used to evaluate the functional form of a and b in Eq. (4.8). Each stroke value has only two data points (which represent the ¼ and ½ open valve conditions), so a linear best fit is used to describe a and b as functions of stroke and dimensionless interface resistance. The values of a and b, as well as the corresponding refrigeration potential can be calculated at any value of stroke and valve resistance using a linear interpolation. For example, a is calculated according to:

$$a = a_{80} + \frac{\Delta a}{\Delta f}\,\Delta f \tag{4.9}$$

$$\text{or } a = a_{80} + \frac{a_{100} - a_{80}}{0.2}(f - 0.8) \tag{4.10}$$

where

$$a_{80} = c_{80} R_I + d_{80} \tag{4.11}$$

and

$$a_{100} = c_{100} R_I + d_{100} \tag{4.12}$$

where $\frac{\Delta a}{\Delta f}$ is the change in coefficient a as the stroke changes, Δf is the difference between the stroke and the 80% stroke, and a_{80}, a_{100}, c_{80}, c_{100}, d_{80}, and d_{100} are coefficients that are determined using experimental data at 80% and 100% stroke. The functional form for the intercept b is computed in a similar way using:

$$b_{80} = e_{80} R_I + n_{80} \tag{4.13}$$

$$b_{100} = e_{100} R_I + n_{100} \tag{4.14}$$

Figure 4-9 (a) and (b) illustrate the experimentally determined slope *a* and intercept *b* of the cold head load curves shown in Figure 4-8 as a function of the valve resistance for the two different values of stroke. All constants from the refrigeration and electric heater power linear equations shown in Figure 4-9 are listed in Table 4-2.

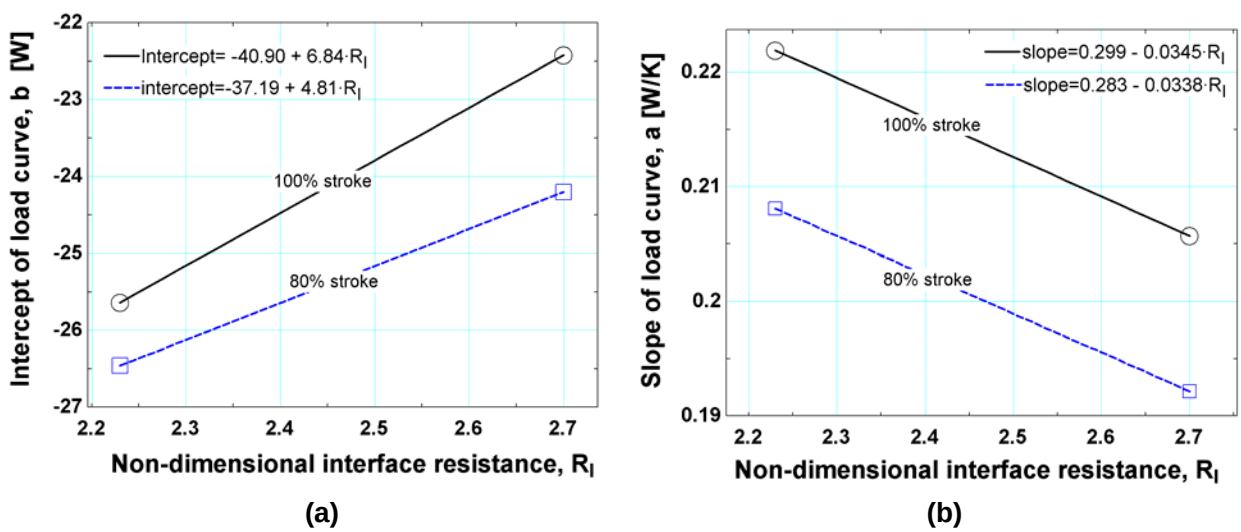

Figure 4-9: **(a) Slope and (b) Intercept of the load curve as a function of the non-dimensional interface resistance at 80% and 100% stroke. The linear functions used to determine the coefficients *c, d, e, and n* are shown.**

Table 4-2: Constants used in linear equations describing pulse tube refrigeration power and mass flow.

Parameter	Value	Parameter	Value
c_{80}	-0.0339 W/K	g_{80}	-3.706 E-5 kg/s
c_{100}	-0.0345 W/K	g_{100}	-4.408 E-5 kg/s
d_{80}	0.284 W/K	h_{80}	2.354 E-4 kg/s
d_{100}	0.299 W/K	h_{100}	2.779 E-4 kg/s
e_{80}	4.81 W	j_{80}	4.296 W
e_{100}	6.84 W	j_{100}	9.84 W
n_{80}	-37.19 W	k_{80}	-4.62 W
n_{100}	-40.90 W	k_{100}	-15.92 W

4.3 Comparison of Transient Model Steady State Load Curves and Experimental Data Steady State Load Curves

The transient thermal model of the PT\RI can be used to predict the quasi-steady performance using the empirical parasitic load, total refrigeration power and mass flow functions defined in Section 4.2. These functions are based on fits to experimental steady state data; therefore the model should predict the steady state performance with a relatively high degree of accuracy. The predicted and experimentally measured distributed (interface) load curves are compared in Figure 4-10 to demonstrate the models ability to qualitatively and quantitatively predict the interface load curves for both stroke and cooling loop valve settings.

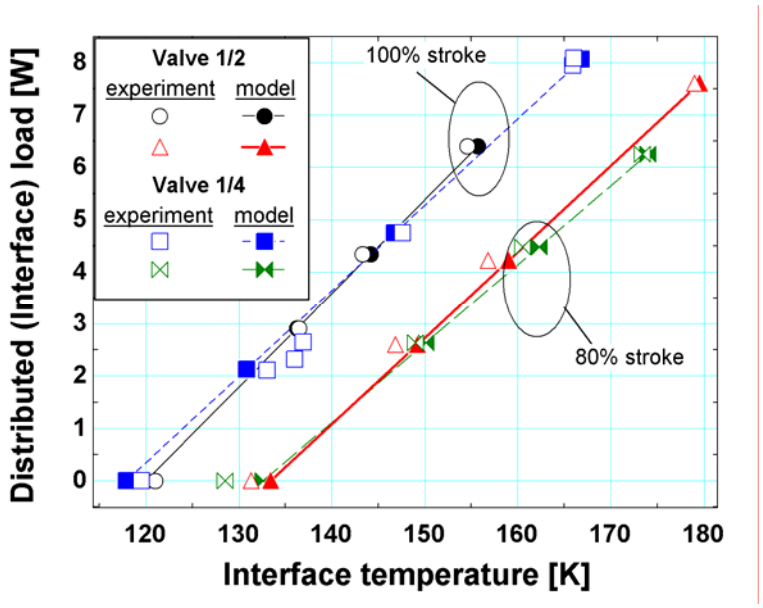

Figure 4-10: **Comparison of interface load curves for the experimental data and the experimentally driven model for both stroke and valve settings.**

4.4 Comparison of Experimentally Measured and Predicted Transient Response

While the thermal capacities of the cold head and the interface do not affect the steady state performance of the system, they do play a primary role in the prediction of the transient behavior of the system. Because of the difficulties associated with measuring the thermal capacitances of complex parts directly, the capacities based on mass measurements and thermal properties are used only as an initial estimate of these quantities. The thermal capacity values used in the model are inferred by matching the predicted and measured transient thermal response of the system at a few, baseline conditions. Transient experimental data were recorded following a step change in stroke, interface thermal load, and interface valve resistance. The transient model is compared with the experimental data by specifying initial conditions and step changes in stroke and distributed interface load that correspond to the imposed experimental conditions.

Figure 4-11 shows the model predictions and the experimental data that correspond to a step change in stroke. The model adequately predicts the measured response, using a cold head

thermal capacitance of 650 J/K, which was selected to best match the temperature rate of change. The primary purpose of the transient model is to capture the transient behavior of the system in order to identify an optimal control scheme; therefore, the cold head thermal capacitance is chosen to best represent the temperature change rather than the absolute temperature values.

Note that there is some offset between the predicted and experimentally measured temperatures during the transient response. The temperature offset near the beginning and end of the transient response (i.e. when the system is at steady state) can be explained by the differences in experimentally measured and modeled steady state temperatures as shown in Figure 4-10. The steady state temperatures from the model, which are a linear fit from the experimental data, are slightly offset from the actual experimental steady data points. Additionally, by selecting a thermal capacitance to best match the temperature rate of change (i.e. the slope of the temperature response shown in Figure 4-11), it is expected that the offset will propagate throughout the duration of the transient response.

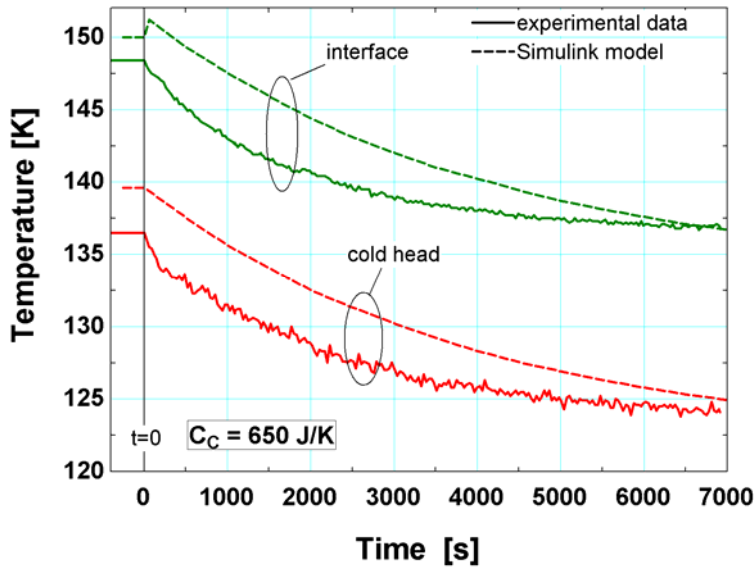

Figure 4-11: Comparison between the model and the experimental data for a step change in stroke (80% to 100%).

Next the model was compared with the experimental data for a step change in interface (distributed) load (7.95 W to 2.32 W), as shown in Figure 4-12. There is good agreement between the model and the experimental data for both the short term response (which is dominated by the interface behavior) as well as the long term response (which is dominated by the cold head behavior). The thermal capacitance values used in the model were also determined in order to provide a best match to the temperature rate of change; the best values of these capacitance for this set of data (i.e. a step change in interface load) were 800 J/K for the cold head and 15 J/K for the interface. The thermal capacitance values of the cold head that provide the best match the transient data for the step change in stroke and interface load are somewhat different; however, if an average cold head thermal capacitance is used, the model is still reasonably predictive for both types of step changes. The linearized operating point transient model developed in Chapter 5 (and subsequently used to optimize the controller in Chapter 6) uses an average of these two estimates of the cold head thermal capacitance (725 J/K).

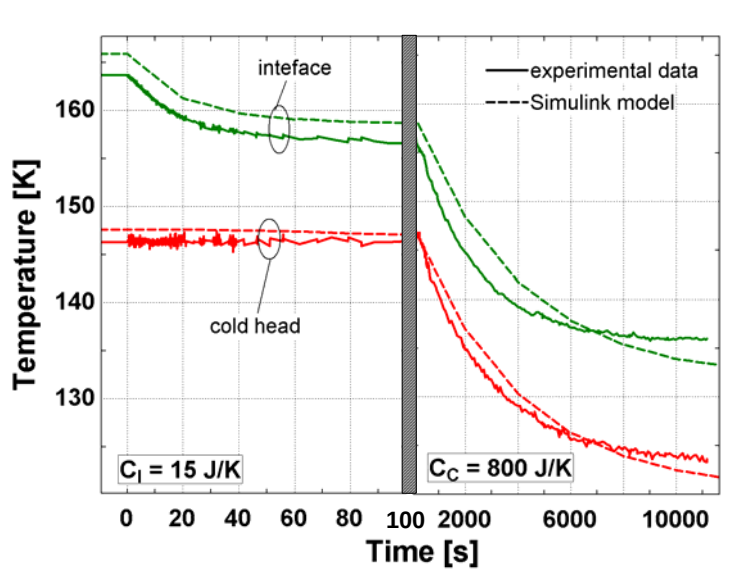

Figure 4-12: Comparison between the model and the experimental data of short long-term transient response to a step change in heat load (8-3 W).

Table 4-3: Nominal values of PT/RI parameters used in the transient thermal model.

Parameter	Value
Pulse tube refrigeration ($\dot{q}_{pt}$)	7.6 W
Interface thermal load ($\dot{q}_I$)	2.6 W
Parasitic load ($\dot{q}_p$)	5 W
Cold head temperature (T_C)	140 K
Interface temperature (T_I)	150 K
Compressor stroke (f)	80%
Cooling loop valve resistance (R_I)	2.70
Nominal cooling loop mass flow ($\dot{m}$)	0.145 g/s
Cold head thermal capacitance (C_C)	725 J/K
Interface thermal capacitance (C_I)	15 J/K
Helium specific heat in cooling loop (c_p)	5.202 kJ/kg-K

4.5 References

1. SIMULINK, The MathWorks, Inc., 39555 Orchard Hill Place Suite 280, Novi, MI 48375, 2005

5 Operating Point Linear PT/RI Thermal Model Development and Verification

A linear, operating point model of the Pulse Tube Rectifying Interface (PT/RI) system was developed based on the non-linear thermal model developed in Chapter 4. The linear model shown graphically in Figure 5-1 considers the transient behavior of the system, that is, the model predicts the temperature disturbance away from a nominal operating point that will occur in response to thermal load disturbances and manipulation of compressor stroke and cooling loop mass flow. The model is complete representation of the system and considers all of the transient, cross-coupled relationships between the state variables (i.e., temperatures), thermal disturbances (electric heat load, parasitic losses) and manipulated inputs (refrigeration power via stroke and cooling loop mass flow via cooling loop valve resistance). A simplified version of the complete linear model is used in Chapter 6 to develop the temperature control algorithms.

5.1 Interface and Cold Head Operating Point Thermal Models

The linear, operating point models of the cold head and the interface are developed based on the non-linear cold head and interface temperature state equations presented in Chapter 4. The state equations predict the transient temperature response to changes in distributed (interface) load, parasitic load, mass flow, pulse tube refrigeration. The interface and cold head governing differential equations developed in Chapter 4 are repeated below:

$$\frac{dT_I}{dt} = \frac{\dot{q}_I + 0.67\dot{q}_p - \dot{m}\,c_p(T_I - T_c)}{C_I} \tag{5.1}$$

$$\frac{dT_C}{dt} = \frac{\dot{m}\,c_p\,(T_I - T_C) + 0.33\dot{q}_p - \dot{q}_{pt}}{C_C} \tag{5.2}$$

The linear, operating point models of the interface and cold head are obtained using a Taylor series expansion of Eqs. (5.1) and (5.2) about a nominal, steady state operating condition. This approach is valid for any operating condition and any system; thus the methodology for determining an optimal control strategy discussed in Chapter 6 is broadly applicable. In order to demonstrate the technique, an experimental steady state operating condition is chosen; the characteristics of this operating point are summarized in Table 5-1.

Table 5-1: PT/RI parameters for a nominal operating point corresponding to an experimental data set. These parameter values are used in Section 5.3 to calculate time constants of the cold head and interface.

Parameter	Value	Parameter	Value
Interface temperature ($T_{I,0}$)	150 K	Non-dimensional interface valve resistance ($R_{I,0}$)	2.44
Cold head temperature ($T_{C,O}$)	140 K	Cooling loop mass flow ($\dot{m}_0$)	0.145 g/s
Interface load ($\dot{q}_{I,0}$)	2.64 W	Cold head thermal capacitance (C_C)	725 J/kg-K
Parasitic heat load ($\dot{q}_{p.0}$)	5 W	Interface thermal capacitance (C_I)	15 J/kg-K
Stroke (f_0)	80%	Helium specific heat (c_p)	5.2 kJ/kg-K

The state equations are linearized with respect to the important time-varying quantities including: mass flow rate, interface temperature, interface temperature time rate of change, cold head temperature, cold head temperature rate of change, interface heat load, pulse tube refrigeration and parasitic load. Note that the Taylor series terms with order greater than one are assumed to be negligible and not included in the linear equations. The operating point models are used to predict changes away from the nominal operating conditions; therefore, only the transient terms from the Taylor series expansion are retained. Additionally, the state variables are expressed in terms of a change from the operating point ($\Delta\dot{m}$,ΔT_I, $\frac{dT_I}{dt}$, ΔT_C, $\frac{dT_C}{dt}$, $\Delta\dot{q}_I$,$\Delta\dot{q}_p$, and $\Delta\dot{q}_{pt}$). The governing operating point model of the interface temperature is:

$$\frac{dT_I}{dt} = \left[\frac{\partial}{\partial \dot{m}}\frac{dT_I}{dt}\bigg|_0\right]\Delta\dot{m} + \left[\frac{\partial}{\partial T_I}\frac{dT_I}{dt}\bigg|_0\right]\Delta T_I + \left[\frac{\partial}{\partial T_C}\frac{dT_I}{dt}\bigg|_0\right]\Delta T_C + \left[\frac{\partial}{\partial \dot{q}_I}\frac{dT_I}{dt}\bigg|_0\right]\Delta\dot{q}_I + \left[\frac{\partial}{\partial \dot{q}_p}\frac{dT_I}{dt}\bigg|_0\right]\Delta\dot{q}_p + \cancel{H.O.T.}^{0} \quad (5.3)$$

Table 5-2 lists the coefficients from the Taylor expansion of the interface temperature state equation. The linear, operating point model of the interface including the coefficients from Table 5-2 is:

$$\frac{dT_I}{dt} = \frac{-c_p(T_{I,0} - T_{C,0})\,\Delta\dot{m} - c_p\dot{m}_0\,\Delta T_I + c_p\dot{m}_0\,\Delta T_C + \Delta\dot{q}_I + 0.67\Delta\dot{q}_p}{C_I} \quad (5.4)$$

Table 5-2: Summary of coefficients from the Taylor expansion of the interface temperature state equation.

$\frac{\partial}{\partial \dot{m}}\frac{dT_I}{dt}\bigg\vert_{\dot{m}_0,T_{I,0},T_{C,0},\dot{q}_{p,0},\dot{q}_{I,0}} = \frac{-c_p\left(T_{I,0} - T_{C,0}\right)}{C_I}$	$\frac{\partial}{\partial T_I}\frac{dT_I}{dt}\bigg\vert_{\dot{m}_0,T_{I,0},T_{C,0},\dot{q}_{p,0},\dot{q}_{I,0}} = \frac{-\dot{m}_0\,c_p}{C_I}$
$\frac{\partial}{\partial T_C}\frac{dT_I}{dt}\bigg\vert_{\dot{m}_0,T_{I,0},T_{C,0},\dot{q}_{p,0},\dot{q}_{I,0}} = \frac{\dot{m}_0 c_p}{C_I}$	$\frac{\partial}{\partial \dot{q}_I}\frac{dT_I}{dt}\bigg\vert_{\dot{m}_0,T_{I,0},T_{C,0},\dot{q}_{p,0},\dot{q}_{I,0}} = \frac{1}{C_I}$
$\frac{\partial}{\partial \dot{q}_p}\frac{dT_I}{dt}\bigg\vert_{\dot{m}_0,T_{I,0},T_{C,0},\dot{q}_{I,0},\dot{q}_{p,0}} = \frac{0.67}{C_I}$	

The operating point model of the cold head is formed using the same process as with the interface model. The Taylor expansion of Eq. (5.2) is:

$$\frac{dT_C}{dt} = \left[\frac{\partial}{\partial \dot{m}}\frac{dT_C}{dt}\bigg|_0\right]\Delta\dot{m} + \left[\frac{\partial}{\partial T_I}\frac{dT_C}{dt}\bigg|_0\right]\Delta T_I + \left[\frac{\partial}{\partial T_C}\frac{dT_C}{dt}\bigg|_0\right]\Delta T_C + \left[\frac{\partial}{\partial \dot{q}_p}\frac{dT_C}{dt}\bigg|_0\right]\Delta\dot{q}_p + \left[\frac{\partial}{\partial \dot{q}_{pt}}\frac{dT_I}{dt}\bigg|_0\right]\Delta\dot{q}_{pt} + \cancel{H.O.T.}^{0} \quad (5.5)$$

Table 5-3 lists the coefficients from the Taylor expansion of the interface temperature state equation. The linear, operating point model of the interface including the coefficients from Table 5-3 is:

$$\frac{dT_C}{dt} = \frac{c_p(T_{I,0} - T_{C,0})\Delta\dot{m} + c_p\dot{m}_0\,\Delta T_I - c_p\dot{m}_0\Delta T_C + 0.33\Delta\dot{q}_p - \Delta\dot{q}_{pt}}{C_C} \tag{5.6}$$

Table 5-3: Summary of coefficients from the Taylor expansion of the cold head temperature state equation.

$\frac{\partial}{\partial\dot{m}}\frac{dT_C}{dt}\Big\vert_{\dot{m}_0,T_{I,0},T_{C,0},\dot{q}_{p,0},\dot{q}_{pt,0}} = \frac{c_p\left(T_{I,0}-T_{C,0}\right)}{C_C}$	$\frac{\partial}{\partial\dot{q}_p}\frac{dT_I}{dt}\Big\vert_{\dot{m}_0,T_{I,0},T_{C,0},\dot{q}_{p,0},\dot{q}_{pt,0}} = \frac{0.33}{C_C}$
$\frac{\partial}{\partial T_I}\frac{dT_C}{dt}\Big\vert_{\dot{m}_0,T_{I,0},T_{C,0},\dot{q}_{p,0},\dot{q}_{pt,0}} = \frac{\dot{m}_0 c_p}{C_C}$	$\frac{\partial}{\partial\dot{q}_{pt}}\frac{dT_I}{dt}\Big\vert_{\dot{m}_0,T_{I,0},T_{C,0},\dot{q}_{p,0},\dot{q}_{pt,0}} = \frac{-1}{C_C}$
$\frac{\partial}{\partial T_C}\frac{dT_C}{dt}\Big\vert_{\dot{m}_0,T_{I,0},T_{C,0},\dot{q}_{p,0},\dot{q}_{pt,0}} = \frac{-\dot{m}_0 c_p}{C_C}$	

5.2 Pulse Tube Refrigeration and Mass Flow Operating Point Models

Operating point models for the pulse tube refrigeration and cooling loop mass flow are also developed from the non-linear, empirical-based equations discussed in Chapter 4. The linear models are formed using the same first order Taylor series expansion technique used to develop the linear interface and cold head governing equations. The non-linear pulse tube refrigeration potential model is:

$$\dot{q}_{pt} = a\left(R_I, f\right)T_C + b\left(R_I, f\right) + \dot{q}_p \tag{5.7}$$

The operating point models of the pulse tube refrigeration and cooling loop mass flow consider only the transient behavior away from a nominal operating point, and therefore the state variables are expressed in terms of a change from the operating point (ΔR_I, Δf, ΔT_C, $\Delta\dot{q}_p$). A

Taylor expansion (retaining only first order terms) of Eq. (5.7) yields the linear, operating point model of the pulse tube refrigeration.

$$\Delta\dot{q}_{pt} = \left[\left.\frac{\partial\dot{q}_{pt}}{\partial f}\right|_0\right]\Delta f + \left[\left.\frac{\partial\dot{q}_{pt}}{\partial R_I}\right|_0\right]\Delta R_I + \left[\left.\frac{\partial\dot{q}_{pt}}{\partial T_C}\right|_0\right]\Delta T_C + \left[\left.\frac{\partial\dot{q}_{pt}}{\partial\dot{q}_p}\right|_0\right]\Delta\dot{q}_p + \cancel{H.O.T}^{\,0} \qquad (5.8)$$

The coefficients in Eq. (5.8) for the linear pulse tube refrigeration model are listed in Table 5-4.

Table 5-4: Summary of coefficients from the Taylor expansion of the pulse tube refrigeration model.

$\left.\frac{\partial\dot{q}_{pt}}{\partial f}\right\|_{R_{I,0},f_0,T_{C,0},\dot{q}_{p,0}} = \frac{\left[(c_{100}-c_{80})R_{I,0}+d_{100}-d_{80}\right]T_{C,0}+(e_{100}-e_{80})R_{I,0}+n_{100}-n_{80}}{0.2}$
$\left.\frac{\partial\dot{q}_{pt}}{\partial R_I}\right\|_{R_{I,0},f_0,T_{C,0},\dot{q}_{p,0}} = \left[c_{80}+\frac{(c_{100}-c_{80})}{0.2}(f_0-0.8)\right]T_{C,0}+e_{80}+\left(\frac{e_{100}-e_{80}}{0.2}\right)(f_0-0.8)$
$\left.\frac{\partial\dot{q}_{pt}}{\partial T_C}\right\|_{R_{I,0},f_0,T_{C,0},\dot{q}_{p,0}} = c_{80}R_{I,0}+d_{80}+\frac{\left[(c_{100}-c_{80})R_{I,0}+d_{100}-d_{80}\right]}{0.2}(f_0-0.8)$
$\left.\frac{\partial\dot{q}_{pt}}{\partial\dot{q}_p}\right\|_{R_{I,0},f_0,T_{C,0},\dot{q}_{p,0}} = 1$

The non-linear, empirically based equation governing the cooling loop mass flow in the transient model developed in Chapter 4 is:

$$\dot{m} = e(f)R_I + n(f) \qquad (5.9)$$

The Taylor expansion of Eq. (5.9) yields the linear, operating point model of the cooling loop mass flow.

$$\Delta\dot{m} = \left[\left.\frac{\partial\dot{m}}{\partial f}\right|_0\right]\Delta f + \left[\left.\frac{\partial\dot{m}}{\partial R_I}\right|_0\right]\Delta R_I + \cancel{H.O.T}^{\,0} \qquad (5.10)$$

Including the coefficients listed in Table 5-5, the operating point model of the cooling loop mass flow is:

$$\Delta\dot{m} = \left[\frac{\left(g_{100} - g_{80}\right)R_{I,0} + h_{100} - h_{80}}{0.2}\right]\Delta f + \left[g_{80} + \frac{g_{100} - g_{80}}{0.2}\left(f_0 - 0.8\right)\right]\Delta R_I \qquad (5.11)$$

Table 5-5: Summary of coefficients from the Taylor expansion of the cooling loop mass flow model.

$\left.\frac{\partial\dot{m}}{\partial f}\right\|_{R_{I,0},f_0} = \frac{\left(g_{100} - g_{80}\right)R_{I,0} + h_{100} - h_{80}}{0.2}$	$\left.\frac{\partial\dot{m}}{\partial R_I}\right\|_{R_{I,0},f_0} = g_{80} + \frac{g_{100} - g_{80}}{0.2}\left(f_0 - 0.8\right)$

5.3 State Block Diagram of Complete Operating Point PT/RI Thermal Model and Discussion of Time Constants

The State Block Diagram (SBD) of the operating point, transient thermal PT/RI model is shown in Figure 5-1. The SBD is a graphical representation of the linear state equations developed in Sections 5.1 and 5.2, and shows the relationships between the state variables (temperatures), thermal disturbances (electric heat load, parasitic losses) and manipulated inputs (refrigeration power via stroke and mass flow via cooling loop valve resistance). An effective interface refrigeration term ($\Delta\dot{q}_{I,r\text{-}eff,\dot{m}}$) is shown in Figure 5-1 and represents the additional cooling power provided by adjusting the mass flow rate; this cooling power is defined as:

$$\Delta\dot{q}_{I,r\text{-}eff,\dot{m}} = \Delta\dot{m}\,c_p\left(T_{I,0} - T_{C,0}\right) \qquad (5.12)$$

Section 3.5 showed that the interface temperature (ΔT_I) fluctuates rapidly in response to thermal disturbances because of its relatively small thermal capacitance. The cooling loop mass flow ($\Delta\dot{m}$) and subsequent effective interface refrigeration ($\Delta\dot{q}_{I,r\text{-}eff,\dot{m}}$) can be adjusted rapidly via the

cooling loop valve; the effective interface refrigeration is therefore used as the controlled parameter for minimizing the relatively fast interface temperature fluctuations.

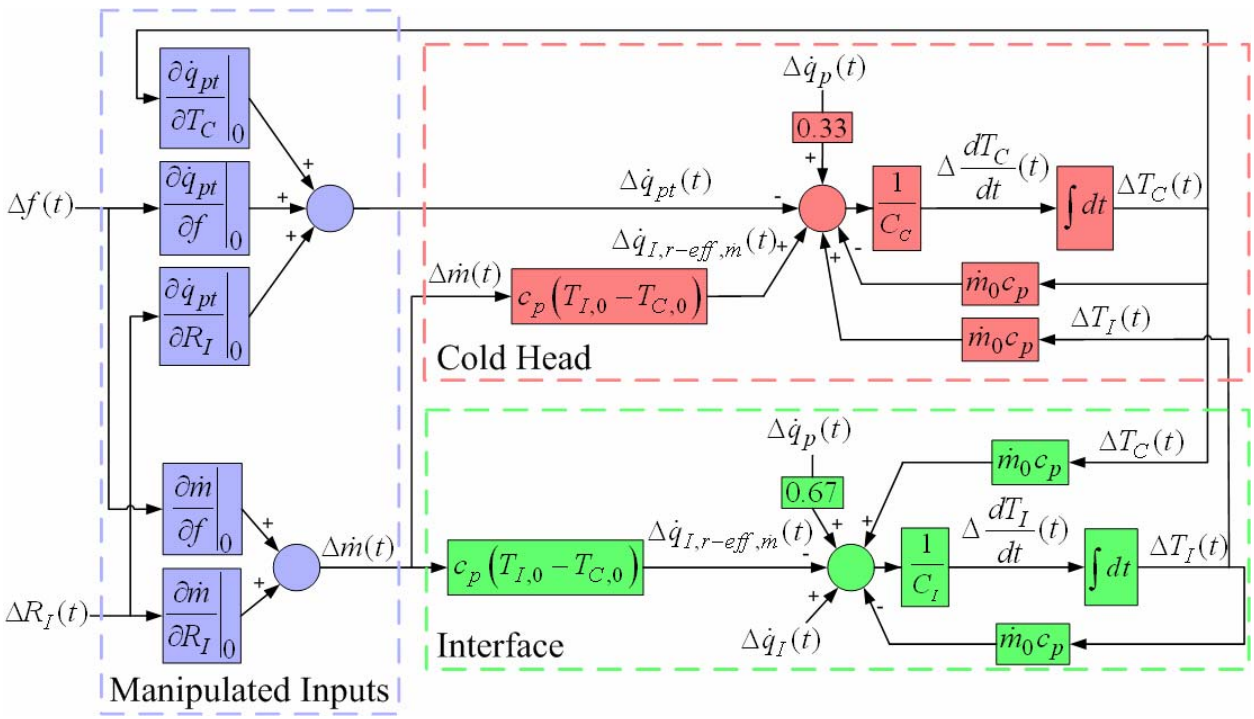

Figure 5-1: State block diagram of the complete operating point, transient thermal model of the PT/RI system.

It is convenient to describe the system in the Laplace domain rather than the time domain in order to develop linear control algorithms and generalize the system transient dynamics. The Laplace transforms of Eqs. (5.4) and (5.6), respectively, yield:

$$\Delta T_I(\mathrm{s}) = \frac{-c_p\left(T_{I,0}-T_{C,0}\right)\Delta\dot{m} + c_p\dot{m}_0\Delta T_C + \Delta\dot{q}_I + 0.67\Delta\dot{q}_p}{C_I\left(s+\dfrac{c_p\dot{m}_0}{C_I}\right)} \tag{5.13}$$

and:

$$\Delta T_C(\mathrm{s}) = \frac{c_p\left(T_{I,0}-T_{C,0}\right)\Delta\dot{m} + c_p\dot{m}_0\Delta T_I + 0.33\Delta\dot{q}_p - \Delta\dot{q}_{pt}}{C_C\left(s+\dfrac{c_p\dot{m}_0}{C_C}\right)} \tag{5.14}$$

where s is the Laplace operator. Equations (5.13) and (5.14) show that the cold head and interface can be characterized as first order thermal systems with time constants:

$$\tau_C = \frac{C_C}{c_p \dot{m}_0} \tag{5.15}$$

$$\tau_I = \frac{C_I}{c_p \dot{m}_0} \tag{5.16}$$

where τ_C and τ_I are the cold head and interface time constants, respectively; the value of these time constants for the system and operating point considered here are 960 s and 20 s according to the nominal parameter values listed in Table 5-1. The methodology for modeling the system remains valid provided that the cold head time constant is substantially greater than the interface time constant.

6 Automatic Temperature Control Law Development

A simplified version of the complete Pulse Tube Rectified Interface (PT/RI) thermal linear model developed in Chapter 5 (Figure 5-1) is used in this section to develop temperature control algorithms for the cold head and the interface. The simplified model shown in Figure 6-1 facilitates the development of a closed form solution for selecting controller gains in terms of desired thermal response, specifically, settling time (t_s) and maximum temperature fluctuation (ΔT_{max}). Only the dominant transient relationships from the complete model are considered; for example, the effect of cold head temperature fluctuations on the interface temperature is neglected. Section 5.3 shows that the time constant associated with thermal disturbances at the cold head is 960 s, whereas the interface time constant is 20 s and so this simplification is justified. The validity of the simplified model is demonstrated in Figure 6-6 by a comparison of the controlled temperature response predicted by the simplified linear model, and the complete non-linear model.

The control scheme developed in this section is physically implemented using a digital controller, so a digital model of the interface system was created based on the simplified linear model. The performance predicted using a digital model is compared with the analog model. The agreement of these two models demonstrates the validity of using the somewhat simpler analog control theory to select the controller gains. The digital model is also used to show that the maximum controller sample period allows for a stable, controlled system.

6.1 Simplified Operating Point PT/RI Thermal Model

The State Block Diagram (SBD) of the complete thermal model in Figure 5-1 shows that the PT/RI has relatively complicated and cross linked relationships between the system parameters

including the manipulated inputs, state variables, and disturbances. However, many of these system parameters have a strong dependence on only one of the other parameters. Therefore, a simplified model shown in Figure 6-1 is created using reasonable assumptions which neglects several of these weaker parameter relationships; the simplified model reduces the overall complexity of the model. The simplified model facilitates the development of a closed form selection of feedback gains to meet the temperature control specifications, such as maximum temperature fluctuation to a sudden change (step) in thermal load. The assumptions used to build the simplified model are verified in Section 6.2.1 by examining the agreement between the thermal behavior predicted by the simplified, linear model with the behavior predicted by the complete, non-linear model in cases where both of these models employ the same temperature control algorithms.

The simplifying assumptions include:

1. The cold head temperature can be assumed constant when considering the interface thermal behavior.

2. The interface temperature can be assumed constant when considering the cold head thermal behavior, as the controlled interface temperature will fluctuate on the order of 50 seconds while the controlled cold head temperature will fluctuate on the order of 500 seconds. These time scales are determined by the controllers develops later in this chapter.

3. The dependence of cooling loop mass flow on compressor stroke is neglected.

4. An effective cold head thermal load disturbance $\Delta\dot{q}_{C,d\text{-}eff}$ is defined which combines the dependence of pulse tube refrigeration on cooling loop valve resistance and cold head temperature, as well as the effective thermal load resulting from changing the cooling loop mass flow (i.e. the $\Delta\dot{q}_{I,r\text{-}eff,\dot{m}}$ term which acts on the cold head).

5. The cold head and interface parasitic loads fluctuate on a very long time scale and therefore are assumed constant; the parasitic loads are subsequently not considered in the simplified transient model.

Explanation of Assumptions:

1. The cold head temperature is assumed to be constant when considering the interface thermal behavior because the time constants associated with temperature fluctuations at the interface and the cold head differ by a factor of nearly twenty, as shown by Section 5.3 It is anticipated that this type of time constant separation will exist for most systems that would employ a distributed cooling system for precise temperature control. The separation of the time constants is further supported by experimental data; for example, Figure 3-8 shows that the interface responds to interface load changes over 10's of seconds, while the cold head temperature remains essentially constant until nearly 500 seconds have passed.

2. The interface temperature is assumed to be constant when considering the cold head, as the controller developed in Chapter 6 is designed to regulate the interface temperature and bring it back under control very quickly; a target settling time is 50-100 seconds (i.e. the interface temperature returns to within 2% of its original values within 50-100 seconds). The time period of the controlled interface temperature fluctuations is much smaller than the 500's of

seconds associated with cold head temperature changes, and therefore the interface temperature is assumed constant relative to the cold head.

3. The dependence of cooling loop mass flow on compressor stroke is neglected because the compressor stroke will be adjusted over a very long time scale (500's of seconds) as the primary input used to control the temperature of the cold head. Again, because the cold head temperature varies slowly, this control input will vary slowly relative to the time scale associated with the interface temperature (approximately 50-100 seconds). Further discussion of the controlled cold head and interface temperature time scales is included in the section describing the control algorithm development in sections 6.2.1 and 6.2.2.

4. The effective cold head thermal load disturbance, $\Delta\dot{q}_{C,d\text{-}eff}$, is a simplification of the combined effect of the dependence of pulse tube refrigeration on cold head temperature and interface valve resistance as well as the effective cold head thermal load resulting from a change in the cooling loop mass flow. It is possible to decouple the effect that these parameters have on the cold head with. However, that process is beyond the scope of this research project and these cross coupled relationships are instead lumped together as one thermal disturbance at the cold head. Additionally, the focus of this research is to control the interface temperature, which can be readily accomplished with reasonable cold head temperature control as shown by the experimental results in Chapter 7.

5. The cold head and interface parasitic load are shown as fractions of the total parasitic load ($\dot{q}_p$) in Figure 5-1. Note that the parasitic loads are different than the disturbance loads (i.e. distributed interface load). The parasitic load is different from the distributed load in that the parasitic load is assumed to be a relatively steady state phenomenon, and therefore does not

affect the transient behavior of the system. The disturbance loads can fluctuate rapidly; therefore it is the disturbance response to changes in distributed load, not parasitic load, which is the important metric for characterizing the performance of the temperature controller.

The resulting simplified time domain governing equations derived from from Eqs. (5.1) and (5.2) are:

$$\Delta \frac{dT_C}{dt} = \frac{-c_p \dot{m}_0 \Delta T_C - \Delta \dot{q}_{pt} + \Delta \dot{q}_{C,d-eff}}{C_C} \tag{6.1}$$

$$\Delta \frac{dT_I}{dt} = \frac{-c_p (T_{I,0} - T_{C,0})\, \Delta \dot{m} - c_p \dot{m}_0\, \Delta T_I + \Delta \dot{q}_I}{C_I} \tag{6.2}$$

The simplified Laplace domain governing equations are:

$$\Delta T_I(s) = \frac{-\Delta \dot{q}_{I,r-eff,\dot{m}}(s) + \Delta \dot{q}_I(s)}{C_I \left(s + \dfrac{c_p \dot{m}_0}{C_I} \right)} \tag{6.3}$$

$$\Delta T_C(s) = \frac{-\Delta \dot{q}_{pt}(s) + \Delta \dot{q}_{C,d-eff}(s)}{C_C \left(s + \dfrac{c_p \dot{m}_0}{C_C} \right)} \tag{6.4}$$

The assumptions used to build the simplified thermal model are verified by agreement of the complete, non-linear and simplified, linear models of the controlled PT/RI system. The controlled transient response to a step change in thermal load predicted by the two models is compared, where the models use the same feedback control gains. The two models predict a maximum temperature fluctuation that agrees to within 4% and exhibit nearly equal settling time as shown in Figure 6-6.

Figure 6-1 graphically represents the simplified Laplace domain governing equations in SBD form. Note that, unlike the complete model shown in Figure 5-1 , the simplified model treats the cold head and interface as non-interacting thermal systems, which are each controlled by a single manipulated input.

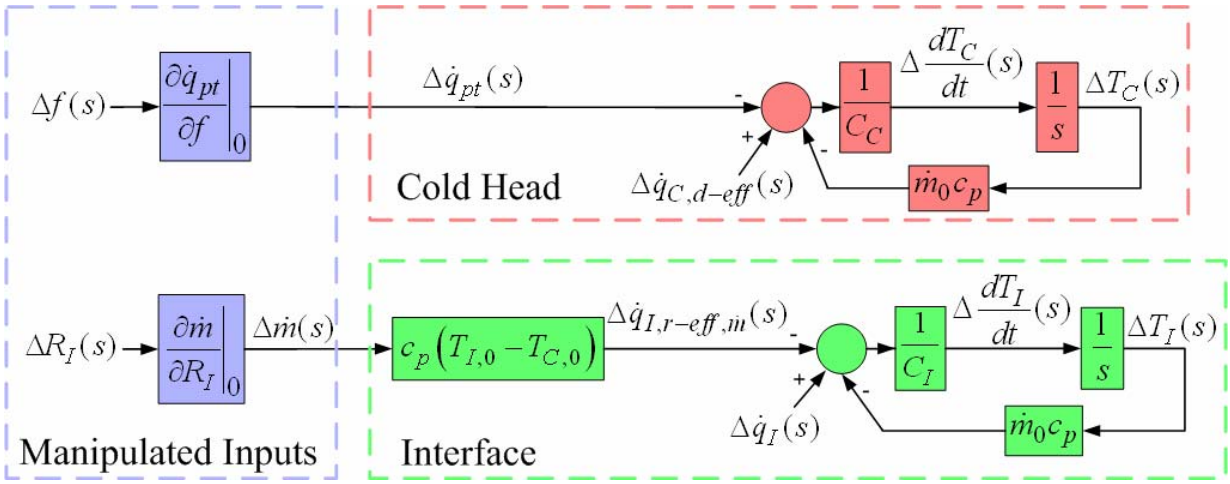

Figure 6-1: State block diagram for the simplified transient thermal model for PT/RI system.

6.2 Analog Temperature Control Algorithm Development

Temperature control algorithms for the cold head and interface are developed using analog control theory. A Proportional-Integral (PI) controller is selected for controlling the PT\RI temperatures; most thermal and fluid systems naturally exhibit stable first order transient behavior and therefore do not require derivative control in order to prevent the error from becoming large [1]. This section describes the development of a closed form solution for the controller gains given a desired damping ratio, settling time, and maximum temperature fluctuation in response to a step change in thermal load.

Section 3.5 showed that changes made to the interface valve and the interface load affect the interface temperature on approximately the same time scale. Therefore, the interface valve can be used to modulate the flow rate in the distribution loop in order to minimize the interface

temperature fluctuations. The PI controller regulates the interface valve resistance using a feedback control signal which sums the proportional and integral values of error (in this case the deviation of the interface temperature from the desired temperature). A similar PI control algorithm is developed for the cold head; this PI controller adjusts the refrigeration power (via compressor stroke) based on the cold head temperature fluctuations.

6.2.1 Interface temperature control

The interface controller adjusts the effective interface refrigeration ($\Delta\dot{q}_{I,r-eff}$) based on the interface temperature deviation (ΔT_I) away from the desired temperature deviation ($\Delta T_{I,des}$), which is zero. Using a PI controller, the change in the effective interface refrigeration is calculated by:

$$\Delta\dot{q}_{I,r-eff} = k_{p,I}\, e_{T,I} + \int_0^t k_{i,I}\, e_{T,I}\, dt \tag{6.5}$$

where $e_{T,I}$ is the interface temperature error defined as.

$$e_{T,I} = \Delta T_{I,des} - \Delta T_I \tag{6.6}$$

and $k_{p,I}$ and $k_{i,I}$ are the proportional and integral gains for the interface controller. The controller transfer function in the Laplace domain is:

$$C_{PI,I}(s) = k_{p,I} + \frac{k_{i,I}}{s} \tag{6.7}$$

The controller gains shown in Figure 6-2 for the interface are selected assuming that the system provides an effective refrigeration ($\Delta\dot{q}_{I,r-eff,\dot{m}}$) that is approximately equal to the commanded effective refrigeration ($\Delta\dot{q}_{I,r-eff,\dot{m}}$*). The complete SBD of the interface control system which

includes the physical relationships of the interface hardware, such as effective refrigeration dependence on mass flow, and mass flow dependence on cooling loop valve position, is shown in Figure 6-11.

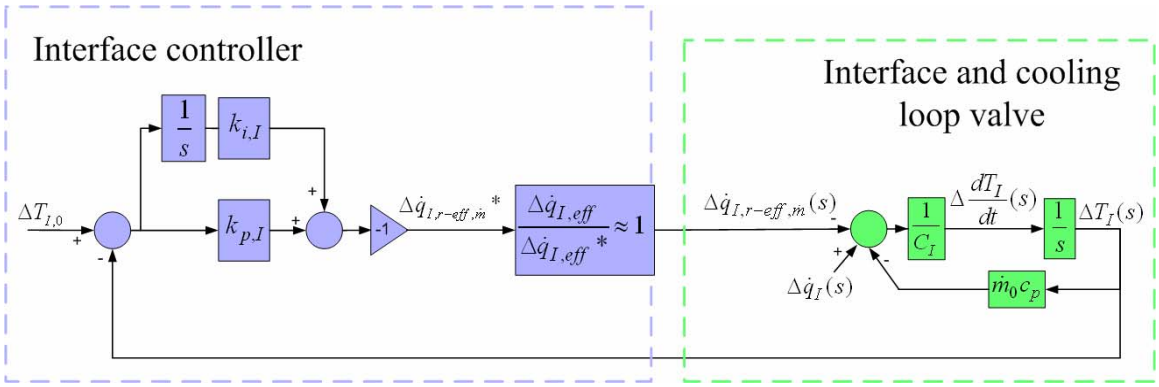

Figure 6-2: State block diagram for the interface with a PI controller. The effective interface refrigeration is assumed to be equal to the commanded effective refrigeration for the controller gain selection process.

The transfer function describing the interface temperature response to changes in interface load is:

$$\frac{\Delta T_I(s)}{\Delta\dot{q}_I(s)} = \frac{1}{C_I}\frac{s}{s^2 + \frac{\dot{m}_0 c_p + k_p}{C_I}s + \frac{k_{i,I}}{C_I}} \tag{6.8}$$

The controlled interface temperature response to a step change in interface load ($\frac{\Delta\dot{q}_I}{s}$) is therefore:

$$\Delta T_I(s) = \frac{1}{C_I}\frac{\Delta\dot{q}_I}{s^2 + \frac{\dot{m}_0 c_p + k_p}{C_I}s + \frac{k_{i,I}}{C_I}} \tag{6.9}$$

The temperature response can be converted to the time domain using an inverse Laplace transform. The standard form of Eq. (6.9) is:

$$\Delta T_I(s) = \frac{\Delta \dot{q}_I}{C_I\, \omega_{n,I}{}^2} \frac{\omega_{n,I}{}^2}{s^2 + 2\,\zeta_I\, \omega_{n,I}\, s + \omega_{n,I}{}^2} \tag{6.10}$$

where $\omega_{n,I}$ is the interface controlled natural frequency:

$$\omega_{n,I} = \sqrt{\frac{k_{i,I}}{C_I}} \tag{6.11}$$

and ζ_I is the controlled interface damping ratio:

$$\zeta_I = \frac{\dot{m}_0\, c_p + k_{p,I}}{2\sqrt{k_{i,I}\, C_I}} \tag{6.12}$$

Figure 6-3 shows a controlled transient response and is referred to in order to clarify the transient response parameters discussed subsequently in this section. Note that the controller parameters used to generate Figure 6-3 were selected so that the damping ratio is low (0.2) in order to highlight the oscillatory response.

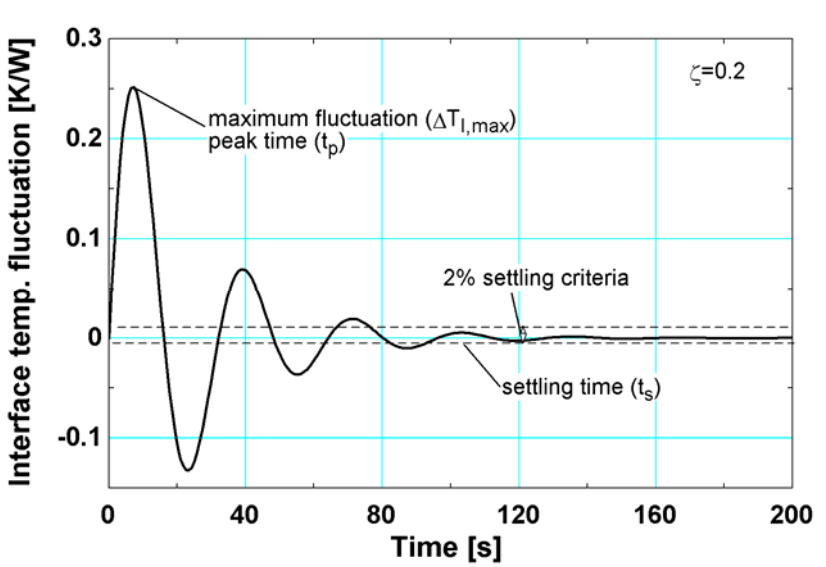

Figure 6-3: Thermal response of interface to step increase in thermal load which shows the important transient response parameters. The damping ratio is set relatively low to highlight the oscillatory behavior.

The maximum interface temperature fluctuation is determined by finding the first peak of the temperature response. The first peak, which is the maximum peak, can be identified by setting the derivative of the temperature response equal to zero. The derivative of the temperature response in Eq. (6.10) is:

$$\frac{d}{dt}T_I(s) = \frac{1}{C_I}\frac{s}{s^2 + 2\zeta_I\,\omega_{n,I}\,s + \omega_{n,I}{}^2} \tag{6.13}$$

The inverse Laplace transform of Eq. (6.13) yields the derivative of the interface temperature response in the time domain.

$$\frac{dT_I}{dt} = \frac{-1}{C_I\beta_I}e^{\zeta_I\,\omega_{n,I}\,t}\sin\left(\omega_n\,\beta_I\,t - \phi_I\right) \tag{6.14}$$

where:

$$\beta_I = \sqrt{1-\zeta_I{}^2} \tag{6.15}$$

and

$$\phi_I = \tan^{-1}\left(\frac{\beta_I}{\zeta_I}\right) \tag{6.16}$$

and t is time. The first peak of the oscillatory temperature response occurs when the derivative of the temperature change first becomes zero and is associated with the first zero of the sinusoidal term in Eq. (6.14); this occurs when the time is:

$$t_{p,I} = \frac{\phi_I}{\omega_n \beta_I} \tag{6.17}$$

where $t_{p,I}$ is the peak time. The peak interface temperature is then calculated by substituting the peak time into the time-domain representation of the interface temperature response. The interface temperature in the time domain is calculated using the inverse Laplace transform of Eq. (6.10).

$$\Delta T_I = \frac{\exp\left(-\zeta_I\, \omega_{n,I}\, t\right)\sin\left(\omega_{n,I}\, \beta_I\, t\right)}{C_I\, \omega_n\, \beta_I} \tag{6.18}$$

The maximum interface temperature change normalized by the magnitude of the thermal disturbance ($\Delta\dot{q}_I$) is formulated by substituting the peak time into the transient interface temperature response from Eq. (6.18).

$$\frac{\Delta T_{I,\max}}{\Delta\dot{q}_I} = \frac{1}{C_I \beta_I \omega_{n,I}} \exp\left(\frac{-\zeta_I\, \phi_I}{\beta_I}\right)\sin\left(\phi_I\right) \tag{6.19}$$

The controlled interface system is 2nd order; the settling time (t_s) for a 2nd order system with a 2% settling criteria is [2]:

$$t_{s,I} = \frac{4}{\zeta_I \, \omega_{n,I}} \tag{6.20}$$

The maximum interface temperature change expressed in terms of the damping ratio and settling time is therefore:

$$\frac{\Delta T_{I,\max}}{\Delta \dot{q}_I} = \frac{t_{s,I} \, \zeta_I}{4 C_I \beta_I} \exp\left(\frac{-\zeta_I \, \phi_I}{\beta_I} \right) \sin\left(\phi_I \right) \tag{6.21}$$

Note that the maximum interface temperature fluctuation is fixed for a given damping ratio (ζ_I) (ϕ_I and β_I are functions of ζ_I according to Eqs. (6.15) and (6.16)) and interface settling time ($t_{s,I}$). Equation (6.19) shows that the temperature response scales linearly with the change in the load. Also, a larger interface heat capacity will tend to reduce the temperature fluctuation as will a more tightly controlled system, represented by a smaller settling time. Equation (6.19) and Figure 6-4 (a) also shows that the maximum temperature fluctuation decreases as damping ratio is reduced. However, decreasing the damping ratio also decreases the system stability. Therefore, a damping ratio of $1/\sqrt{2}$ (0.707) is chosen for the interface controller in order to balance the maximum temperature fluctuation and the stability. The maximum temperature fluctuation as a function of settling time with fixed damping ratio (0.707) is shown in Figure 6-4 (b).

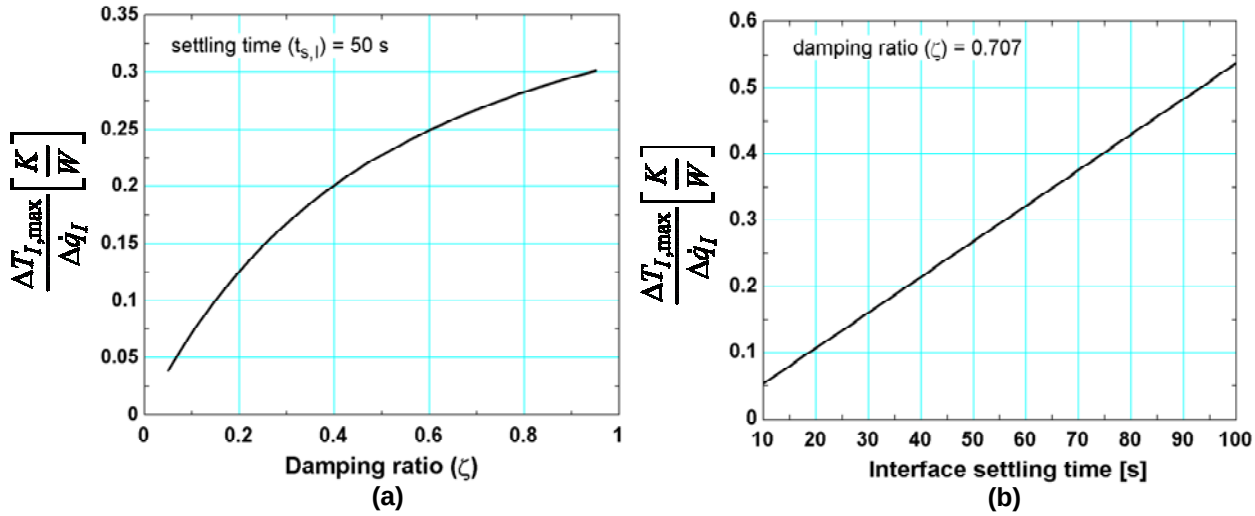

Figure 6-4: Maximum interface temperature fluctuation as a function of settling time with a fixed damping ratio of 0.707.

Figure 6-4 (b) or Eq. (6.21) can be used to select the settling time (and subsequently the controller gains) which yields the desired maximum interface temperature fluctuation. Clearly a smaller settling time leads to a more tightly controlled system; however, the settling time selection must consider the limits of the physical system. A very small settling time could yield an overly sensitive control scheme that is very responsive to noise and therefore less stable. Additionally, the torque and speed limits of the motor and other hardware used to physically affect the control must be considered when choosing the settling time. The settling time selected for experimental testing was 50 s; this settling time selection is discussed further is section 6.4

Selecting the damping ratio and settling time leads to a unique set of controller gains; combining Eqs., (6.11),(6.12), (6.19), and (6.20) yields a closed form solution for the controller gains in terms of the damping ratio (ζ_I), settling time ($t_{s,I}$).

$$k_{i,I} = \frac{16 C_I}{t_{s,I}^{\ 2}\, \zeta_I^{\ 2}} \tag{6.22}$$

and:

$$k_{p,I} = \frac{8\,C_I - t_{s,I}\,\dot{m}_0 c_p}{t_{s,I}} \tag{6.23}$$

Nominal controller gain values used for experimental testing were calculated using a damping ratio of $1/\sqrt{2}$ and a settling time of 50 seconds. Table 6-1 summarizes the nominal interface controller parameters.

It is useful to describe the maximum temperature rise in terms of a dimensionless temperature fluctuation. The dimensionless temperature relation is defined naturally from Eq. (6.21) and is, effectively, the temperature fluctuation normalized by the temperature change that would be experienced by the interface heat capacity (C_I) if it were subjected to the load disturbance for the settling time ($t_{s,I}$). The dimensionless interface temperature fluctuation is only a function of the damping ratio; the dimensionless temperature rise for a damping ratio of 0.707 is 0.081 and is shown in Table 6-1. The dimensionless interface temperature fluctuation is shown as a function of the damping ratio in Figure 6-5.

$$\left(\frac{\Delta T_I\,C_I}{\Delta \dot{q}_I\,t_{s,I}}\right)_{\max} = \frac{\zeta_I \exp\left(\dfrac{-\zeta_I\,\phi_I}{\beta_I}\right)\sin\left(\phi_I\right)}{4\,\beta_I} \tag{6.24}$$

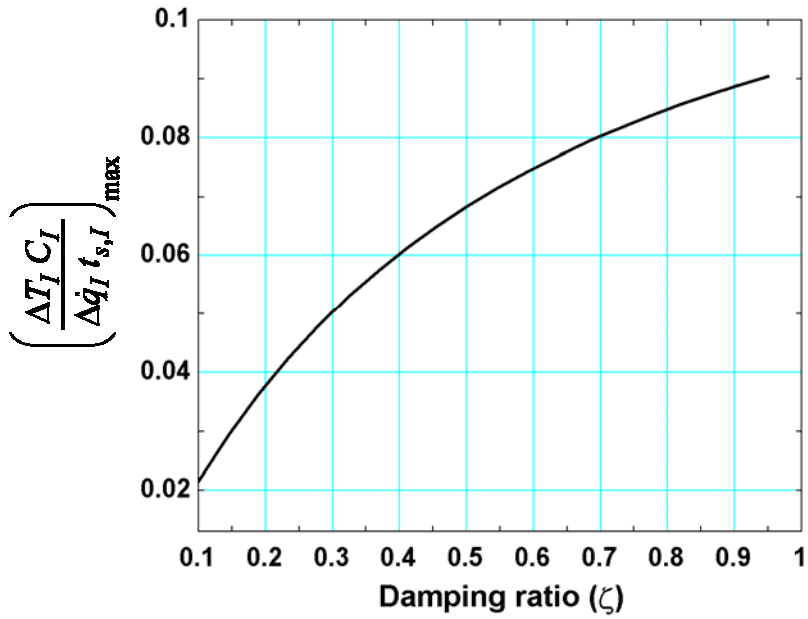

Figure 6-5: Dimensionless interface temperature fluctuation as a function of the damping ratio.

The analytic calculation of maximum temperature in response to a step load increase is verified by comparing with the simplified, linear operating point model (Figure 6-2) with the complete, non-linear model (Chapter 4). The linear model is implemented in MATLAB, the model script is in Appendix B. Both models employ the same control algorithm and gains, as well as the same step change in interface load. The temperature response for a 50 s settling time and damping ratio of 0.707 is shown in Figure 6-6. The predicted maximum temperature rise exactly matches the operating model peak temperature rise (as it should, both are based on the same linear equations), and is very close to the non-linear model peak (agreement is not exact because the nonlinear and weak terms were neglected for the linear model). The agreement between the models in Figure 6-6 also demonstrates the validity of using the simplified, linear model to choose the controller gains that yield the desired performance characteristics.

Table 6-1: Nominal interface controller parameters used in the experimental tests.

Parameter	Nominal Value
Cooling loop mass flow ($\dot{m}_0$)	0.146 g/s
Interface thermal capacitance (C_I)	15 J/kg-K
Helium specific heat (c_p)	5.2 kJ/kg-K
Damping Ratio (ζ_I)	0.707
Interface settling time ($t_{s,I}$)	50 s
Maximum interface temperature fluctuation ($\Delta T_{I,max}$)	0.269 K/W
Dimensionless maximum interface temperature fluctuation $\left(\frac{\Delta T_I\, C_I}{\Delta \dot{q}_I\, t_{s,I}}\right)_{\max}$	0.081
Interface proportional gain ($k_{p,I}$)	1.64 W/K
Interface integral gain ($k_{i,I}$)	0.192 W/k-s

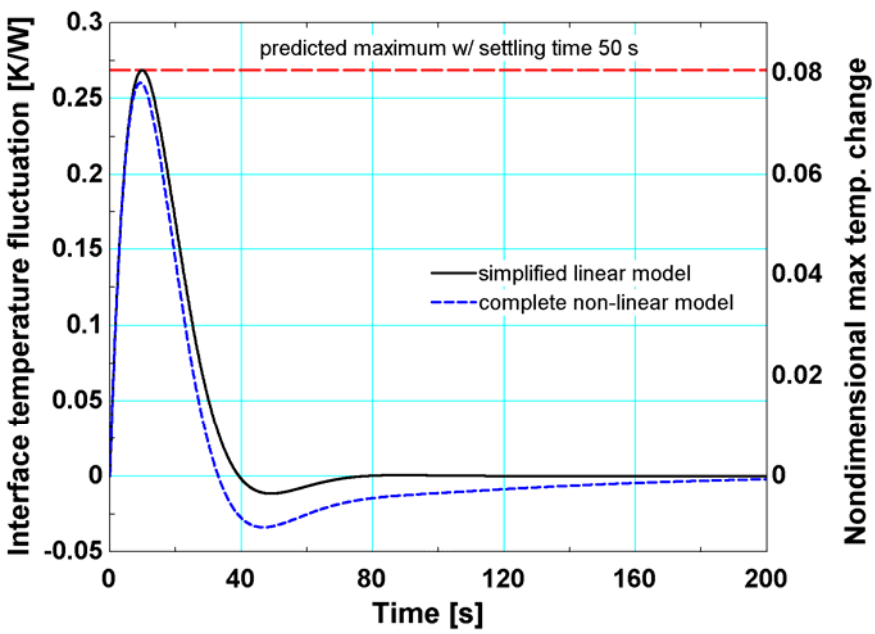

Figure 6-6: Linear and non-linear model prediction of the controlled interface temperature response for a step increase in interface load.

6.2.2 Cold head temperature control

The cold head controller uses a PI control algorithm to adjust the pulse tube refrigeration ($\Delta \dot{q}_{pt}$) based cold head temperature (ΔT_C) fluctuations away from the desired set point. Figure 6-7 shows the controlled cold head topology; note that for the controller design, the commanded

pulse tube refrigeration ($\Delta\dot{q}_{pt}*$) is assumed to be equal to the actual pulse tube refrigeration ($\Delta\dot{q}_{pt}$). A more complete diagram which shows the physical relationships of the cold head hardware, such as pulse tube refrigeration dependence on compressor stroke, and compressor stroke dependence on Variac voltage is shown in Figure 6-12.

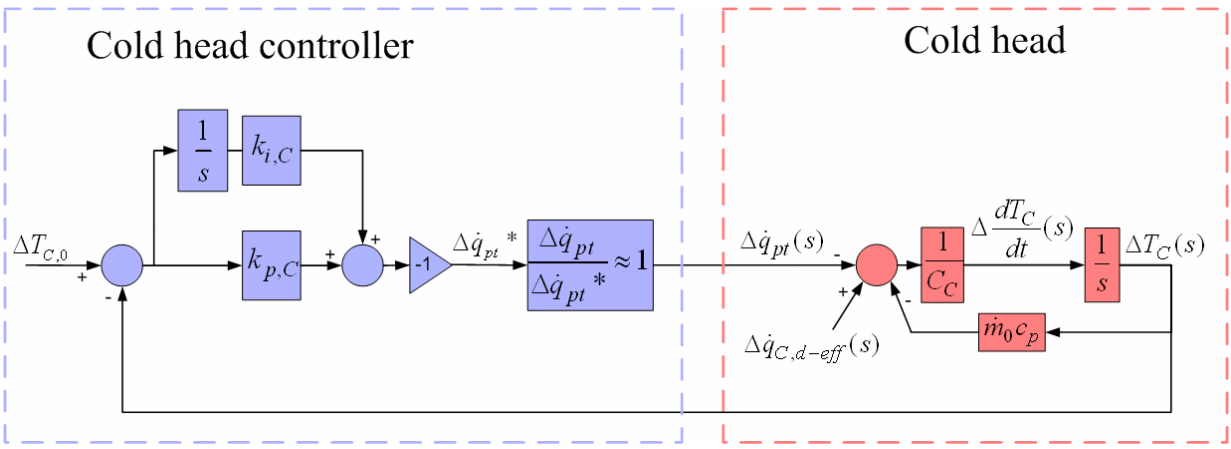

Figure 6-7: State block diagram for the cold head with a PI controller. The pulse tube refrigeration is assumed to be equal to the commanded refrigeration for the controller gain selection process.

The cold head controller gains are selected using the same method as was described for the interface; the gains are selected to achieve a desired transient response to a step change in thermal load. The cold head thermal dynamics are very similar to that of the interface as shown by comparing Figure 6-7 and Figure 6-2. Therefore, the design process described by Eqs. (6.5) through (6.21) for the interface is also used to select the cold head gains (making the appropriate changes to reflect the cold head vs distributed load characteristics). After making the appropriate cold head parameter substitutions (e.g., cold head thermal mass and temperature), the controller gains are set according to:

$$k_{i,C} = \frac{16 C_C}{t_{s,C}^{\ 2}\, \zeta_C^{\ 2}} \tag{6.25}$$

and:

$$k_{p,C} = \frac{8\,C_C - t_{s,C}\,\dot{m}_0 c_p}{t_{s,C}} \tag{6.26}$$

and the maximum cold head temperature fluctuation is:

$$\frac{\Delta T_{C,\max}}{\Delta \dot{q}_{C,d-eff}} = \frac{t_{s,C}\,\zeta_C}{4\,C_C \beta_C} \exp\left(\frac{-\zeta_C\,\phi_C}{\beta_C}\right) \sin\left(\phi_C\right) \tag{6.27}$$

The cold head controller differs from the interface controller in the selection of the damping ratio and settling time. The cold head damping ratio is chosen to be 0.9 to achieve a more damped response. The settling time is a characteristic of the eigenvalue that describes the cold head; therefore, in order to separate the cold head and interface eigenvalues, the cold head settling time is chosen to be 10x the interface settling time (500 s as compared to 50 s). Separating the eigenvalues ensures the controller won't result in a resonance between the cold head and the interface. The maximum cold head temperature fluctuation to a step load change is 0.061 K/W, as calculated by Eq. (6.27) using a settling time of 500 s and a damping ratio of 0.9. Table 6-2 summarizes the cold head controller parameters with nominal performance specifications used in the experimental verification section. The control of the cold head temperature is less important than the control of the interface temperature; therefore a comparison of the linear and non-linear behavior of the cold head is not presented here. The cold head controller developed in this section adequately controls the cold head temperature, as shown in the controlled experimental results section (Chapter 7).

Table 6-2: Nominal cold head controller parameters used in the experimental tests.

Parameter	Nominal Value
Cooling loop mass flow ($\dot{m}_0$)	0.146 g/s
Cold head thermal capacitance (C_C)	725 J/kg-K
Helium specific heat (c_p)	5.2 kJ/kg-K
Damping Ratio (ζ_C)	0.9
Cold head settling time ($t_{s,C}$)	500 s
Maximum cold head temperature fluctuation ($\Delta T_{C,max}$)	0.061 K/W
Dimensionless maximum cold head temperature fluctuation $\left(\frac{\Delta T_C\, C_C}{\Delta \dot{q}_I\, t_{s,C}}\right)_{\max}$	0.081
Cold head proportional gain ($k_{p,C}$)	10.84 W/K
Cold head integral gain ($k_{i,C}$)	0.0573 W/k-s

6.3 Interface digital model development and comparison with analog model

The control algorithms presented in Section 6.2 was analyzed using an analog model but eventually implemented with a digital control system created in the LabVIEW™ software. A digital model of the controlled interface was therefore created and the predicted results are compared with the analog model developed in Section 6.2 in order to ensure that the analog model can be used to select the controller gains. Figure 6-9 shows that the response predicted by the digital model nearly exactly matches the analog model when using the 3.3 Hz sampling rate that is chosen for the experiment. Additionally, the digital model is used to show the minimum sampling rate required to maintain stability is about 0.1 Hz (i.e., one data point every 10 seconds). A digital model of the cold head was not created; it was assumed that the cold head analog model sufficiently predicts the digital implementation given that the cold head has a much longer time scale than the interface. That is, if the sampling rate is acceptable for the analog interface model approximation then the sampling rate it will also be acceptable for the cold head.

The simplified linear analog model of the interface shown in Figure 6-2 is converted to the digital model shown in Figure 6-8. The interface model is converted to the digital domain by including the Zero Order Hold (ZOH) or latch which represents the digital controller's inability to make adjustments to the refrigeration in periods of time that lie between the sample periods.

The interface model in the Z-domain is formulated using a Z-transform of Eq (6.3) including the latched interface:

$$\Delta T_I(z) = \left(1 - z^{-1}\right) \mathbf{Z}\left(\frac{1}{s} \frac{-\Delta \dot{q}_{I,r-eff,\dot{m}}(s) + \Delta \dot{q}_I(s)}{C_I\left(s + \frac{c_p \dot{m}_0}{C_I}\right)} \right) \tag{6.28}$$

which simplifies to:

$$\Delta T_I(z) = \frac{1}{c_p \dot{m}_0} \frac{1 - e^{aT}}{z - e^{aT}} \tag{6.29}$$

where T is the sampling rate, z is the z-transform operator and:

$$a = \frac{1}{\tau_I} = \frac{c_p \dot{m}_0}{C_I} \tag{6.30}$$

The PI controller is defined as:

$$C_{PI,I}(z) = e_{T,I}(z)\left(k_{p,I} + \frac{k_{i,I} T}{1 - z^{-1}}\right) \tag{6.31}$$

Where $e_{T,I}$ is the interface temperature error.

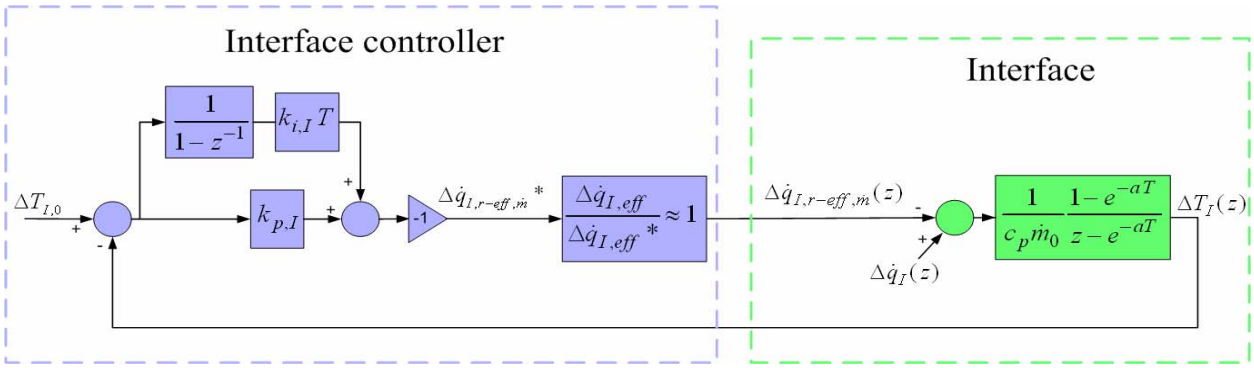

Figure 6-8: State block diagram of the interface with digital control implementation.

The simplified interface digital model was implemented using MATLAB (Script in Appendix B) and it is compared to the analog model in Figure 6-9. The digital model uses a 3.3 Hz sample rate; the analog and digital models both use the controller gains listed in Table 6-1 and are run for a step increase in interface load. The models exhibit nearly identical temperature response which demonstrates the validity of using the analog model to select the controller gains for a digital implementation.

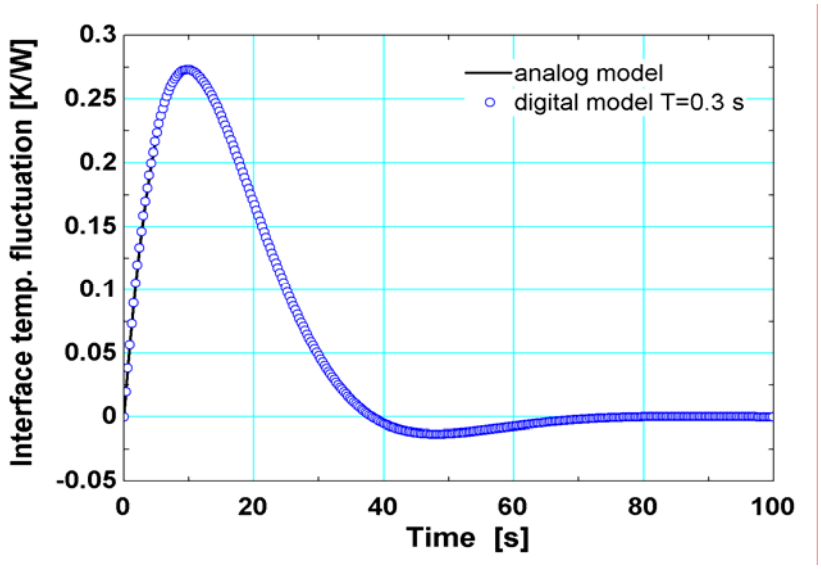

Figure 6-9: **Comparison of the controlled interface temperature response using the digital and analog models. Both models use the controller gains listed in Table 6-1 and a step increase in interface load. The digital model uses a 0.3 s sample period.**

A parametric analysis of the digital model sample period was performed to characterize the maximum allowable sample period required for stability. Short sample periods generally yield stable systems as the controller makes adjustments on a time scale that is faster than the dynamics of the controlled system. However, controller cost (monetary and computational) is inversely related to sample period; therefore the sample period study seeks to find a sample period which balances stability and controller cost. The effect of varying the sample period on the controlled interface temperature is shown in Figure 6-10. The sample period analysis was performed for the interface using the control gains listed in Table 6-1. Figure 6-10 shows the 0.3 s sample period selected for experimental testing is well below the unstable sample period of 12 s, and is a reasonable sample rate for a relatively inexpensive controller.

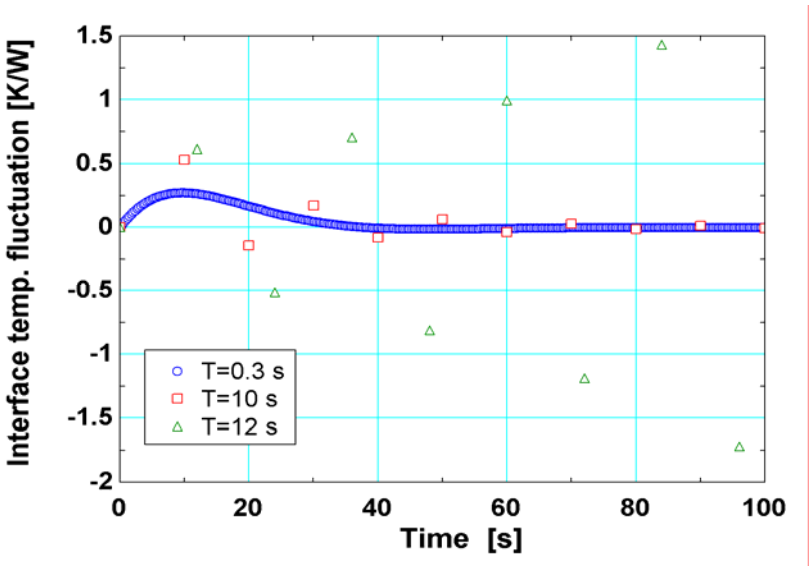

Figure 6-10: **Comparison of the digital controlled interface temperature response using varied controller sample period where model uses the controller gains listed in Table 6-1 and a step increase in interface load. The 0.3 s sample period was chosen for the experimental tests. A 12 s sample period yields an unstable system.**

6.4 Interface settling time selection

The interface settling time was chosen as 50 s as discussed in section 6.2.1. The maximum temperature fluctuation increases with settling time, as shown by Eq.(6.21); therefore, in general, it is desirable to minimize the settling time. However, the control algorithm must also consider the physical limits of the control system. For example the commanded response of the valve required to achieve a small settling time may be unrealistic if the torque or speed required exceeds the maximum performance that can be obtained from the valve stepper motor. Additionally, a robust control scheme must consider the system response to noise; an overly aggressive control scheme will cause the system to continually and significantly respond to noise (e.g., noisy temperature measurements), which can lead to instability and unnecessary wear on the control hardware. For this specific system it is assumed that the motorized valve has very fast dynamics compared to the transient temperature behavior, therefore, the system sensitivity to noise is the primary physical limit that should be considered when selecting the settling time.

A LabVIEW program which simulates the transient behavior of the interface and includes the physical parameters such as valve rotation was used to study the noise system limitation. The LabVIEW program is included with the accompanying CD. Note that the program requires LabVIEW v8.0 or later, the motion control toolkit, and the signal express toolkit. The interface temperature is filtered using both a low-pass 15 Hz analog filter and a low-pass 100 Hz 5th order Bessel Infinite Impulse Response (IIR) digital filter. The filtered signal exhibits noise in the 0.005 to 0.03 K range; 0.03 K noise is used in the model to determine upper limit of the effect signal noise.

Figure 6-11 (a) shows the interface valve response to a random 0.03 K noise with the controller gains listed in Table 6-1. Figure 6-11 (b) shows the corresponding change in interface temperature. The valve rotates by ± 20° which causes the interface temperature to fluctuate by ±0.002 K. In this case, the wear on the valve could be significant and is more important than the relatively small temperature fluctuations. The valve rotation and interface change for 100 and 20 second settling times are ± 5° and ± 60° and 0.001 K and 0.01K. The 50 second settling time chosen for experimental testing nominally balances maximum temperature fluctuation and noise sensitivity.

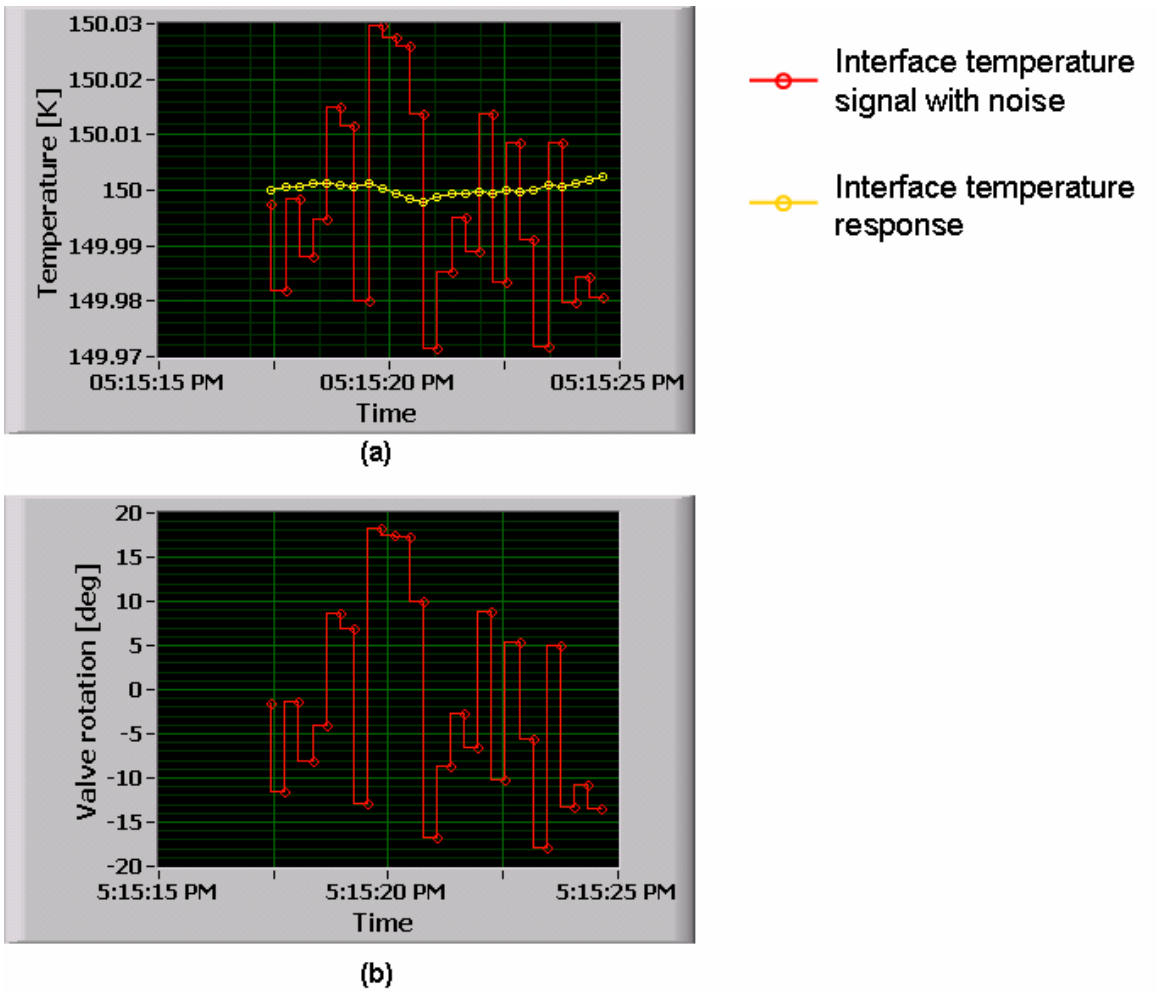

Figure 6-11: **Interface response to signal noise with a settling time of 50 s. The interface valve (a) and interface temperature response (b) are shown.**

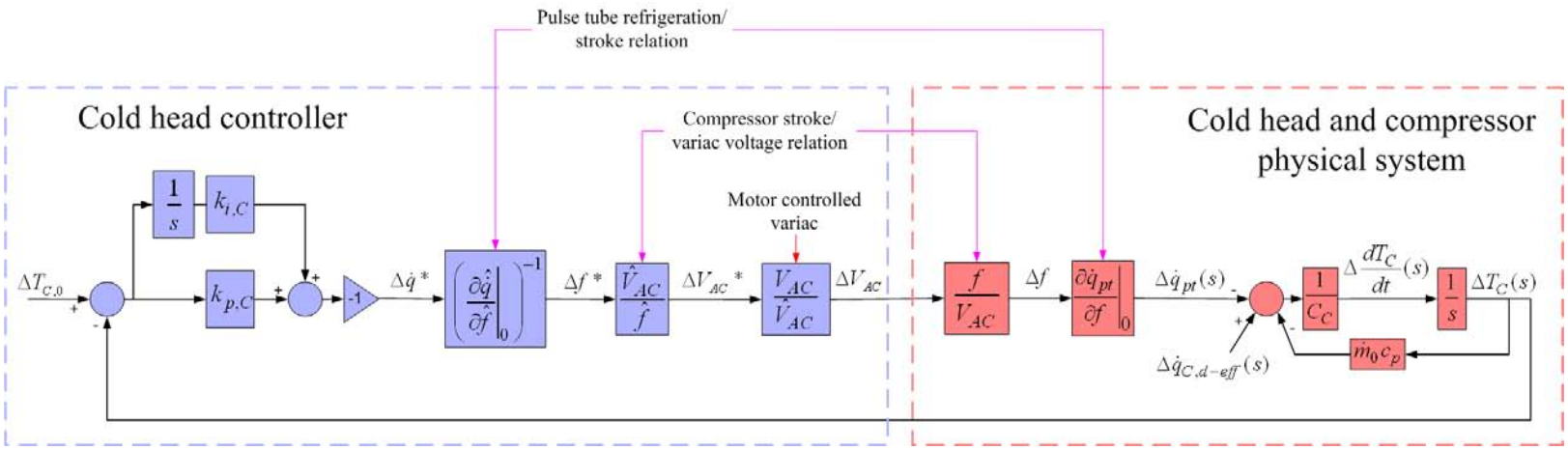

(a)

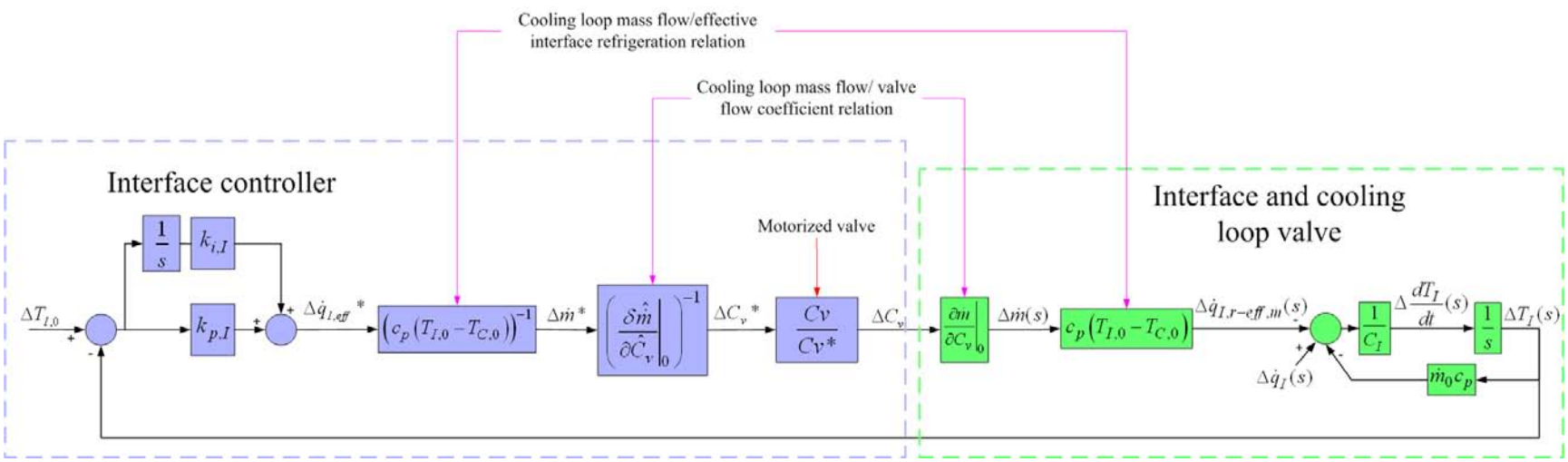

(b)

Figure 6-12: **State block diagrams for the (a) cold head and (b) interface showing the detailed relationships between the hardware physical parameters such as effective interface refrigeration, mass flow, and valve flow coefficient for the interface, and pulse tube refrigeration, compressor stroke, and variac voltage for the cold head.**

6.5 References

1. Munro, N., "The Systematic Design of PID Controllers", in *proceedings of the IEE Colloquium on Symbolic Computation for Control (Ref. No. 1999/088),* pp.10/1-10/9, June 1999

2. Dorf, R.C., Bishop, R.H., *Modern Control Systems, 9th Edition*, Prentice Hall, Inc., New Jersey 07458 p. 228-231 and 367, (2001).

7 Comparison of Modeled and Experimental Controlled Temperature Response

The control algorithms for the cold head and interface developed in Chapter 6 are implemented using LabVIEW software interfaced with the control hardware discussed in Chapter 2. The controlled system performance is studied using step changes in interface load that are applied by the resistance heater connected to the cooling loop. Figure 7-6 shows that with a 0.5 W interface load step increase, the maximum interface temperature fluctuation with no control, pulse tube refrigeration control using cold head temperature feedback (controller 1), pulse tube refrigeration control using interface temperature feedback (controller 2), and both pulse tube refrigeration control using cold head temperature feedback and interface valve control using interface temperature feedback (controller 3) was 1.8 K, 0.35 K, 0.15 K and 0.08 K, respectively. The additional temperature control afforded by the interface valve is discussed in this chapter.

The predicted and measured interface temperature response is compared in Figure 7-9 for a step increase and a step decrease in the interface load. The model predicts the maximum temperature fluctuation to within 40% for the step increase in interface load and to within 7% for a step decrease in interface load. The settling times were 100 s and 70 s for the increase and decrease in load, respectively, as compared to 50 s predicted by the model. Note that the results in this chapter show steady operating temperatures near 215 K, while the results from Chapter 3 show temperatures near 140 K. The pulse tube developed a leak and had to be repaired; the pulse tube performance significantly decreased after the repair. The cause of the decreased performance has not been identified. Fortunately, the temperature control concept presented here is valid at any temperature, so the results at higher temperature are valid for predicting lower temperature operation.

7.1 Uncontrolled and Baseline Control Experimental Results

Figure 7-1 shows the experimental cold head and interface temperature response to a 0.5 W step increase in interface load with no control system. The uncontrolled response is similar to the response studied in Chapter 4; the interface temperature increases by 0.35 K on the short time scale associated with its own thermal mass (~20 s) and the cold head temperature increases by 1.8 K according to its own time scale of ~1000 s. On the longer time scale, the interface temperature response follows the cold head.

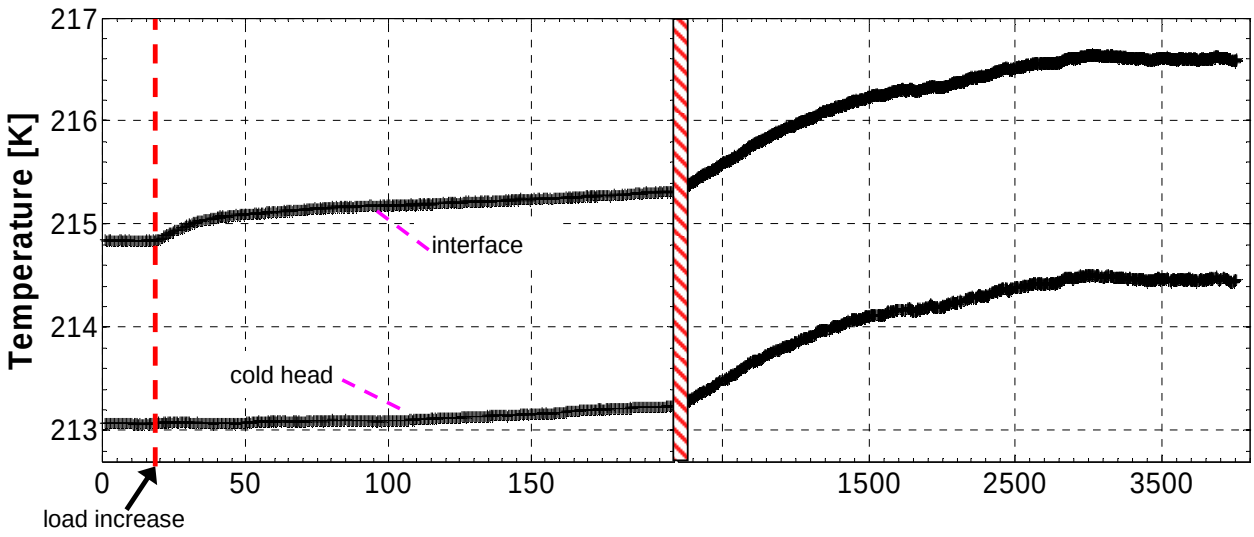

Figure 7-1: Interface and cold head temperature response to a 0.5 W step increase in interface load with no temperature control

The transient response of the system to a step increase in distributed load with the cold head temperature controlled via feedback that regulated the pulse tube refrigeration (i.e., control of the variac voltage) was studied. Figure 7-8 (a) shows the State Block Diagram (SBD) of the system in this configuration. The response of the interface with cold head control only is used as a baseline to demonstrate the additional temperature control that is available with the interface valve that would not be available in a conventional system. Figure 7-2 shows the interface (a) and cold head (b) temperature response to a 0.5 W step increase in interface load. The interface

temperature rapidly rises 0.35 K, as it did in the completely uncontrolled case; the thermal mass of the cold head requires 100's of seconds to respond and therefore the control algorithm computed based on cold head temperature fluctuation will not respond quickly enough to regulate the interface temperature during its initial, rapid temperature increase. However, the interface temperature does not increase beyond the initial 0.35 K deviation over the long term as the cold head refrigeration is adjusted to maintain a constant cold head temperature. Note that the interface exhibits steady state error as the interface temperature is not explicitly controlled. Additionally, the experimental test with cold head control only is much shorter than the uncontrolled test as the system reaches steady state more rapidly.

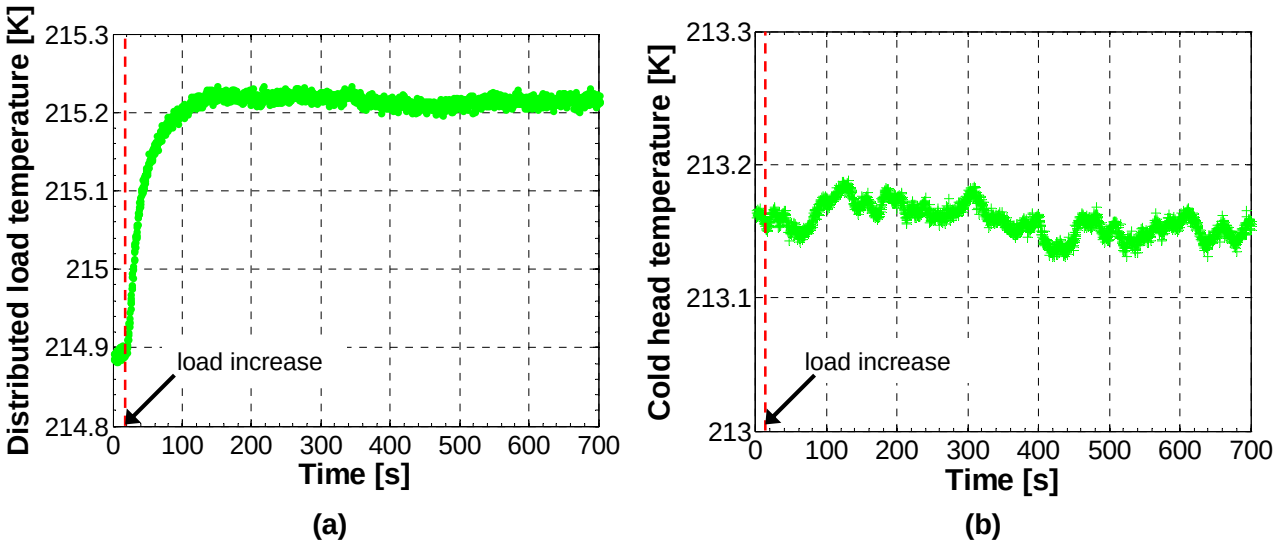

Figure 7-2: **Interface (a) and cold head (b) temperature response to a 0.5 W step increase in interface load with pulse tube refrigeration control using cold head temperature feedback.**

Another baseline test was performed where the pulse tube refrigeration was regulated based on the interface temperature error. Figure 7-8 (b) shows the SBD of the system in this configuration. The performance of the system based on the interface temperature fluctuation is significantly improved, as shown in Figure 7-3. The maximum interface temperature fluctuation

is 0.15 K and the settling time is about 200 s. The interface temperature is controlled by the decreasing cold head temperature, which provides an effective interface refrigeration defined as:

$$\Delta\dot{q}_{I,r-eff,T_C} = \dot{m}_0\, c_p\, \Delta T_C \tag{7.1}$$

where $\Delta\dot{q}_{I,r-eff,T_C}$ is the effective caused by a change in cold head temperature (ΔT_C), $\dot{m}_0$ is the nominal cooling loop mass flow rate, and c_p is the specific heat of Helium listed in Table 5-1. A pictorial representation of $\Delta\dot{q}_{I,r-eff,T_C}$ is shown in Figure 7-8.

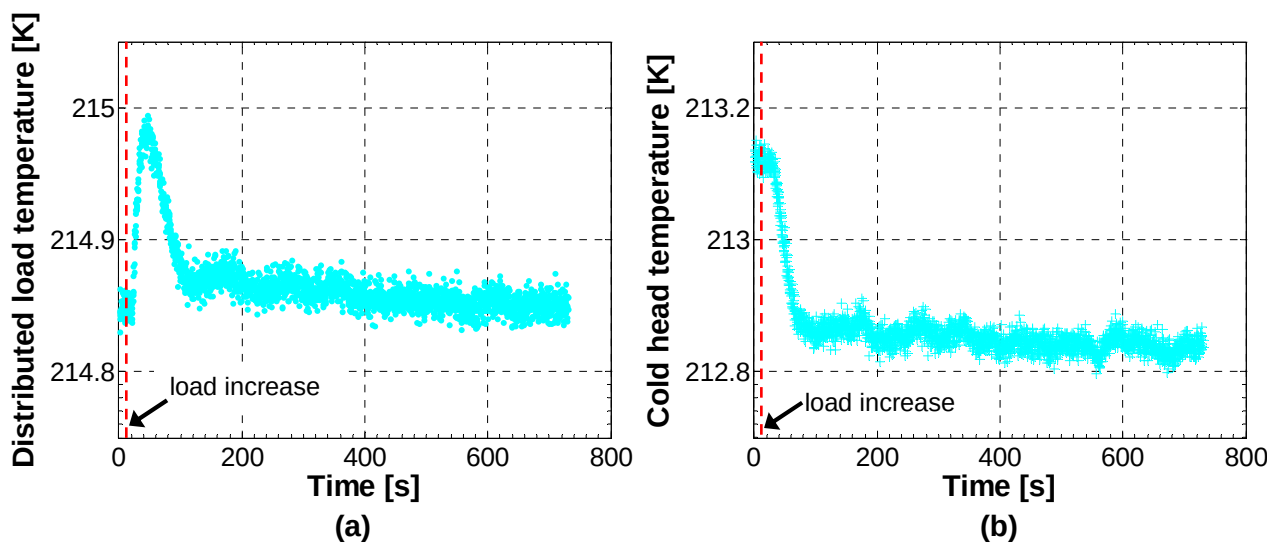

Figure 7-3: Interface (a) and cold head (b) temperature response to a 0.5 W step increase in interface load with pulse tube refrigeration control using interface temperature feedback.

The physical model shown in Figure 7-8 highlights the assumption that the dominant interface cooling, when control is provided adjusting the pulse tube refrigeration, is provided by the change in cold head temperature ($\Delta\dot{q}_{I,r-eff,T_C}$), and not the change in cooling loop mass flow ($\Delta\dot{q}_{I,r-eff,\dot{m}}$). The pulse tube refrigeration is adjusted via compressor stroke, which affects the pressure differential driving the helium through the distribution loop. However, Figure 7-4

shows that experimentally, the effective interface refrigeration from the changing mass flow is small compared to the refrigeration from the changing cold head temperature.

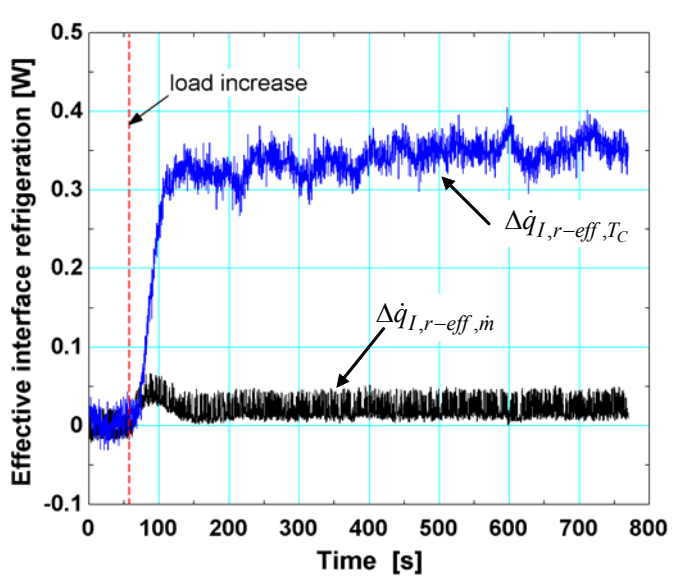

Figure 7-4: **Effective interface refrigeration for the controlled 0.5 W step response shown in Figure 7-3 where the pulse tube refrigeration is adjusted using the interface temperature feedback.**

7.2 Full Control Experimental Results

The interface temperature response is more tightly controlled when both the cold head and interface control are employed as shown in Figure 7-5. The maximum interface temperature fluctuation is reduced by a factor of 4 (compared with ΔT_C feedback control of $\Delta\dot{q}_{pt}$: Figure 7-2) and a factor of 2 (compared with ΔT_C feedback control of $\Delta\dot{q}_{pt}$: Figure 7-3). The settling time is reduced to about 100 s. Note that the interface temperature has no steady state error as it is explicitly integral controlled. Additionally, the maximum temperature fluctuation here is limited by hardware specific to this demonstration of the PT/RI concept. Tighter temperature control could be achieved, for example, with a more aggressive control strategy (i.e. larger interface controller gains), which would require feedback signals with less noise. This

improvement could be accomplished with better wire shielding, additional filtering efforts, or use of an observer [1] with observer temperature feedback.

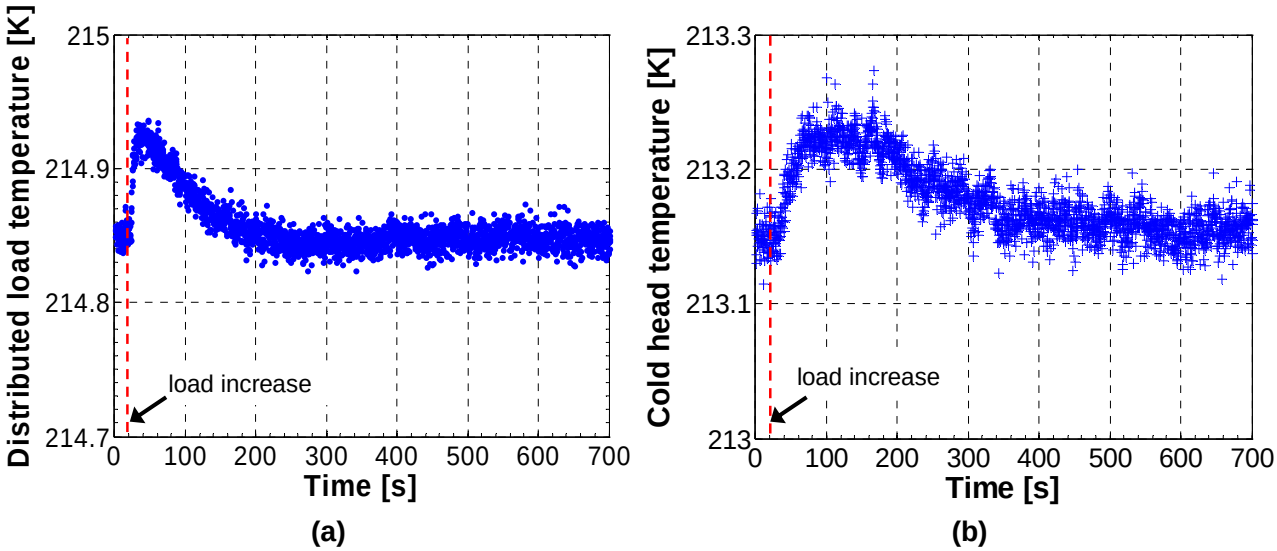

Figure 7-5: Interface (a) and cold head (b) temperature response to a 0.5 W step increase in interface load with a cold head and interface temperature control.

7.3 Comparison of Experimental Results

The transient responses to a 0.5 W step increase in interface load with the four controller implantations: no control, pulse tube refrigeration control using cold head temperature feedback (referred to as controller 1), pulse tube refrigeration control using interface temperature feedback (referred to as controller 2), and both cold head and interface control (referred to as controller 3) are compared in Figure 7-6(a). Clearly, the responses with control have reduced temperature fluctuation compared with the uncontrolled test. Figure 7-6(b) show same data displayed in Figure 7-6(a), but it focuses on the interface temperature data with control.

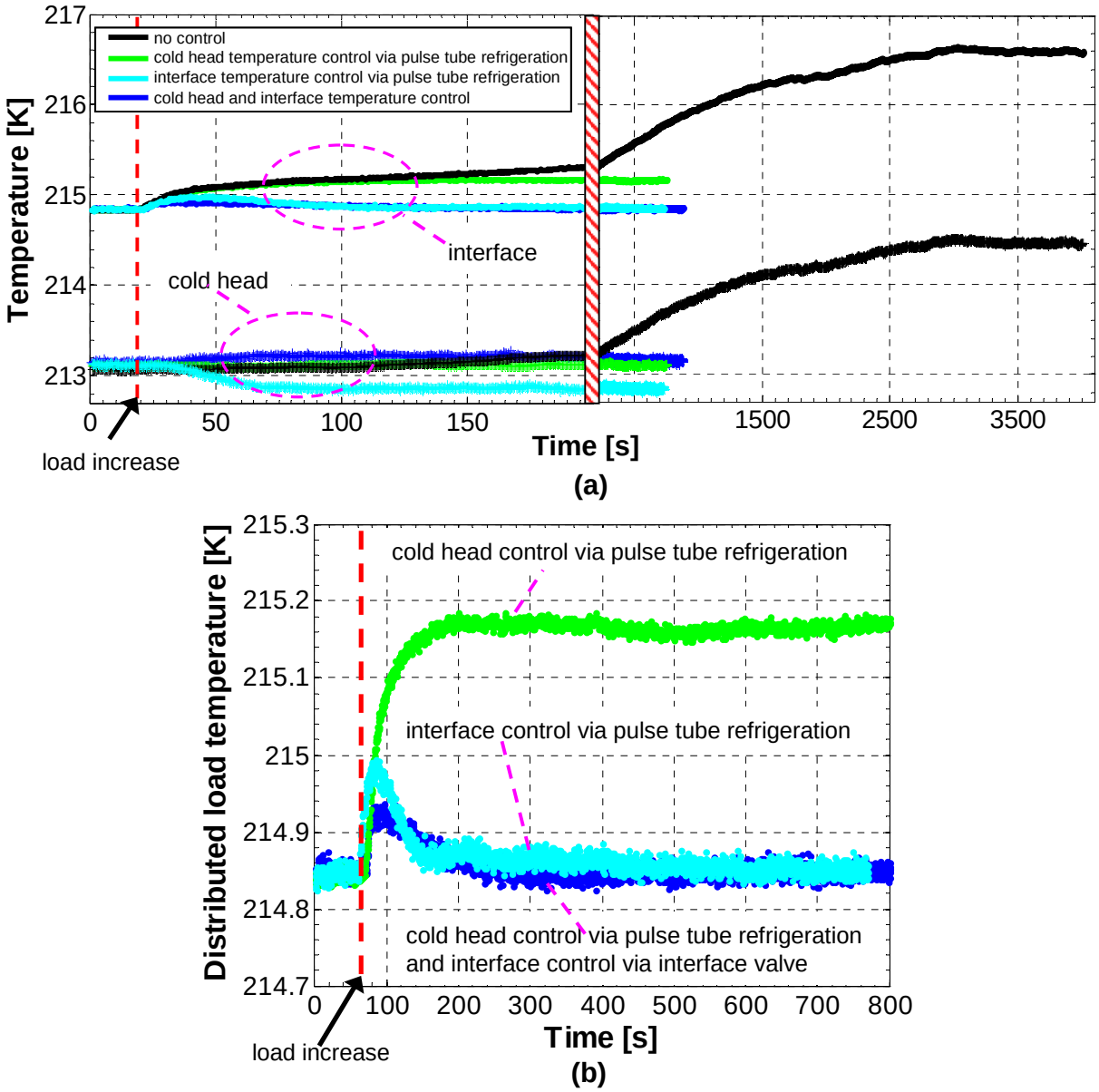

Figure 7-6: **Interface temperature response to a 0.5 W step increase in interface load with: (a) no control, pulse tube refrigeration control using the cold head temperature feedback or interface temperature feedback, and both cold head and interface control and (b) cold head control only and both cold head and interface control.**

Figure 7-6 shows the system experiences a smaller temperature fluctuation when the interface temperature is explicitly controlled using either the interface valve (controller 3) or the pulse tube refrigeration (controller 2). Additionally, the system disturbance rejection, characterized by the maximum temperature fluctuation and settling time, is only marginally better using controller

3 compared to controller 2. This result was somewhat unexpected as controller 2 must change a high energy state to regulate the interface temperature, where controller 3 changes a low energy state to regulate the interface temperature. The cold head thermal mass requires a relatively large amount of energy to change and is therefore considered a high energy state, whereas the cooling loop mass flow can be adjusted quickly with little energy and is a low energy state. Therefore, it was expected that controller 3 would show a significantly better disturbance rejection than controller 2 as controller 3 can adjust the effective interface refrigeration with less energy.

The unexpected performance of controller 2 is explained by Figure 7-7 which shows the cooling rate related to the manipulated state (i.e. pulse tube refrigeration $\Delta\dot{q}_{pt}$ for controllers 1 & 2 and $\Delta\dot{q}_{I,r-eff,\dot{m}}$ for controller 3). Controller 2 requires 2.5 times the change in pulse tube cooling power required for steady state, while controller 3 only requires 1.2 times the change in effective refrigeration for steady state. The maximum temperature fluctuation with controller 2 is nominally double as that with controller 3. Controller 2 therefore requires about 4 times more manipulated cooling rate change capacity than is needed for controller 3. Therefore, the fundamental advantage of using the interface valve is the reduction in cooling rate capacity required to regulate the interface temperature. For a given pulse tube, the interface valve extends the range of distributed loads for which the system can achieve a desired temperature control.

Unfortunately, this range extension was not plainly demonstrated with these tests, as the pulse tube refrigeration did not reach its saturation limit in the test shown in Figure 7-3 and Figure 7-7. Additionally, the performance with controller 3 could have been improved with more aggressive controller gains while controller 2 would quickly reach hardware limitations if its gains were

increased. Controller 3 gains were limited for testing because of noise related issues discussed in Chapter 6.

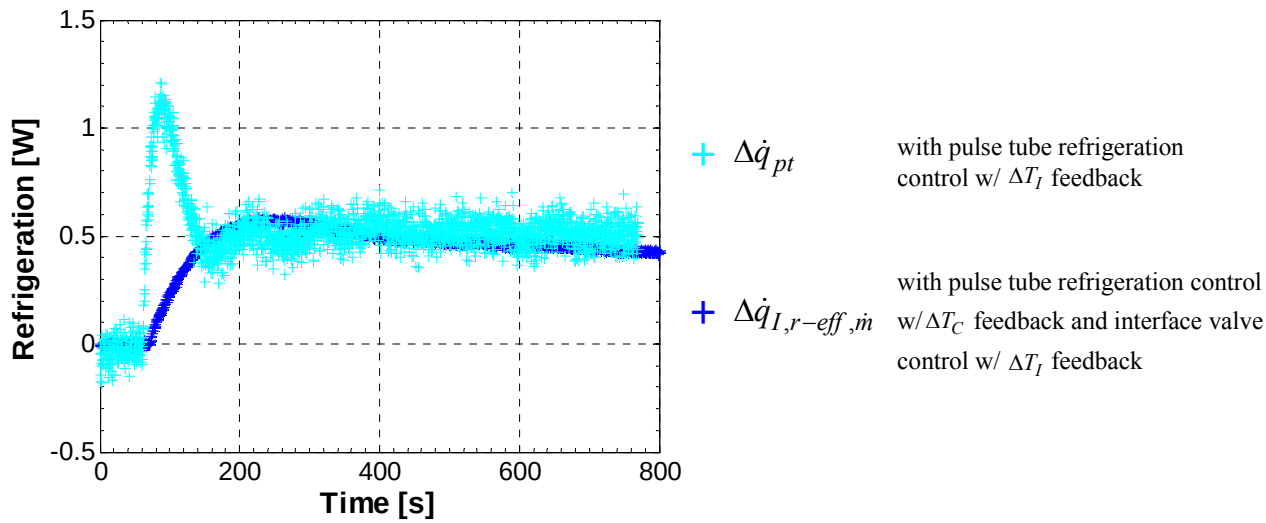

Figure 7-7: Manipulated cooling rate for the controller 2 (pulse tube refrigeration control using interface temperature feedback), and controller 3 (pulse tube refrigeration control using cold head temperature feedback and cooling loop mass flow control using interface temperature feedback).

A current typical method for controlling distributed loads is via a conductive strap (e.g., a copper bus bar), which thermally links the cold head and the interface. In this configuration, the pulse tube refrigeration is adjusted using the interface temperature as feedback; this control method is referred subsequently as controller 0. The PT/RI system with controller 2 offers two main advantages compared with controller 0. First, the conductive straps are large and inflexible compared to the tubing used to distribute the cooled Helium with the PT/RI system. The tubing is therefore much more convenient than conductive straps to distribute over long or complex pathways. The second advantage with controller 2 is that the time scale with which pulse tube refrigeration adjustments are applied to the to the interface is shorter than the corresponding time scale for controller 0. The rate at which controller 2 can change effective interface refrigeration is limited by the cold head thermal mass and the time required for the helium to leave the cold

head and reach the distributed load. The rate at which controller 0 can change the effective interface refrigeration is limited by the cold head thermal mass and the thermal resistance of the conductive strap. For any considerable distance, the conductive strap will either be resistive or massive and therefore controller 2 can change the interface refrigeration more rapidly than controller 0.

Controllers 2 and 3 can provide nominally equivalent performance (within a factor of 2) with regard to control authority under certain circumstances, as shown by the controlled temperature response in Figure 7-6 (b). However, controller 2 has two main hardware restrictions that can be avoided using controller 3. The first limitation with controller 2 is related to the relatively large amount additional pulse tube cooling capacity required to adjust the effective interface refrigeration for this configuration, as previously shown in Figure 7-7. The second limitation with controller 2 is related to its off-design performance. If the steady state load changes significantly, the required pulse tube performance relative to cold head temperature and cooling loop mass flow will be unbalanced and may fall outside the available performance map. For example, with controller 2 if the load is significantly increased, the cooling loop mass flow is fixed and only by significantly reducing the cold head temperature can the system control the load change. However, it may not be possible to achieve the required cold head temperature reduction even at full stroke due to limitations in the steady state performance shown in Figure 3-5. Controller 3 adjusts the mass flow and therefore does not require the cold head temperature to change; the pulse tube performance map constraint will therefore be satisfied over a wider range of distributed loads.

The choice of whether to include cooling loop valve control must consider the required temperature control performance as well as the expected range of distributed loads. If the

temperature control achievable with the controller 2 configuration is acceptable, and if the distributed load is relatively static, it is likely not worth the additional complexity of implementing the cooling loop valve control. The valve can be adjusted statically to achieve the desired nominal operating point manually, but would not be dynamically controlled. Automatic interface valve control and controller algorithm 3 can be implemented for: tighter temperature control, a larger envelope of manageable distributed loads, or for systems with multiple distributed loads and interface loops connected to a single cold head, which require the ability to individually adjust the effective interface refrigeration for each loop.

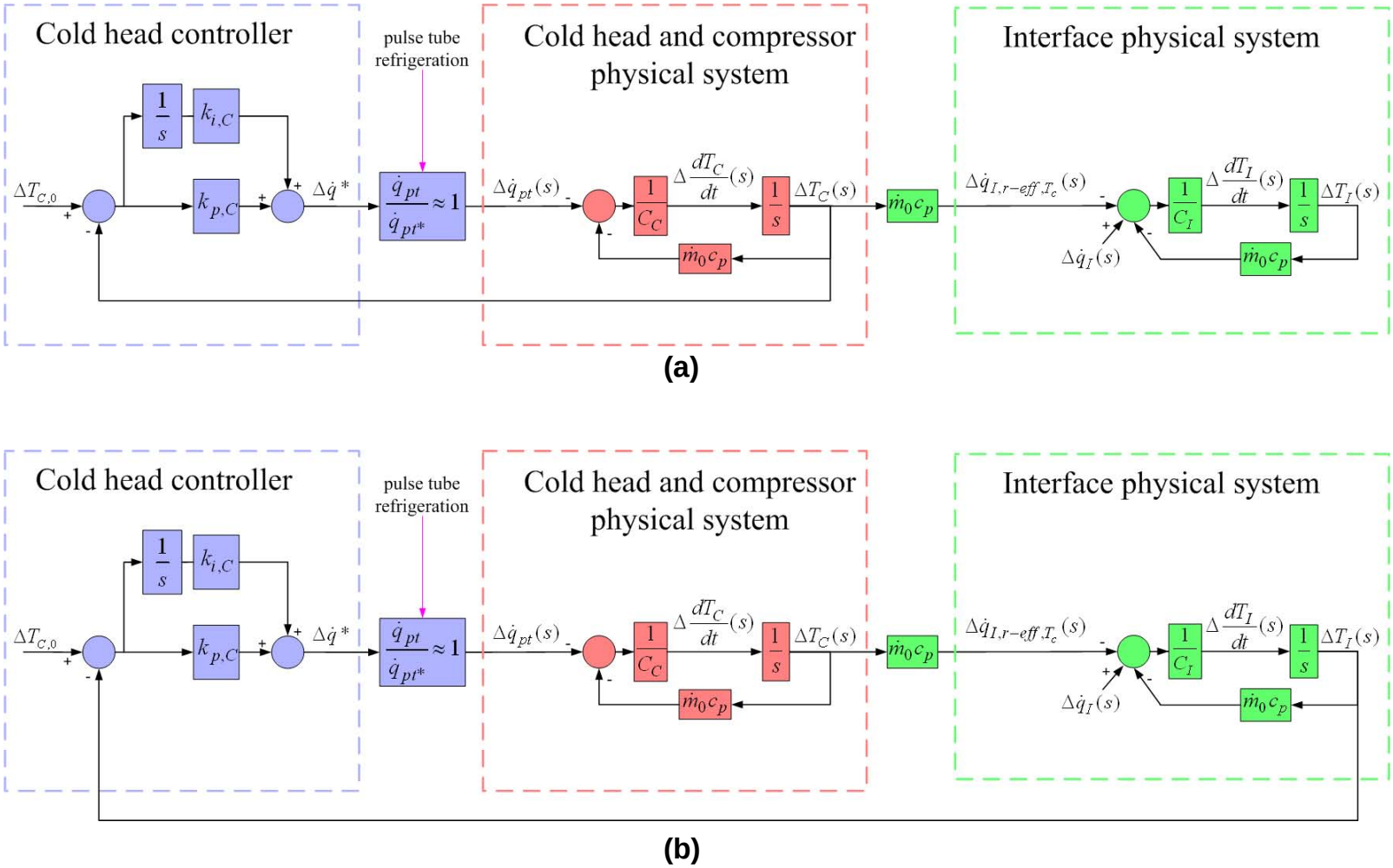

Figure 7-8: **State block diagrams for the baseline control case where the pulse tube refrigeration is regulated using (a) the cold head temperature feedback and (b) interface temperature feedback.**

7.4 Comparison of Predicted and Experimentally Measured Controlled Temperature Response

Figure 7-9 shows the comparison of the predicted and measured interface temperature response with both cold head and interface control (controller 3). The model is compared with the experimental results for both a step increase and step decrease in the interface load in order to demonstrate that the control algorithm and modeling efforts are valid for both positive and negative load fluctuations. The model predicts the maximum temperature fluctuation to within 40% for the step increase in interface load and to within 7% for a step decrease in interface load. The settling times were 100 s and 70 s for the increase and decrease in load, respectively, as compared to 50 s predicted by the model. The differing absolute responses between the increase and decreased interface load suggests that the commanded and actual effective interface refrigeration ($\Delta\dot{q}_{I,r-eff}*$) and ($\Delta\dot{q}_{I,r-eff}$) are not equal.

The primary uncertainty in the model relative to the discrepancy in commanded and provided effective refrigeration is the relationship between the mass flow rate and valve position; this relationship is based entirely on the theoretical equation provided by the valve manufacturer and has no in-situ empirical validation. Note that Chapter 3 does discuss an empirical model for mass flow rate; however, the interface valve used to develop this model was different than the valve used to implement the control strategy. Suggestions for further work in this regard include experimental validation of the valve position/mass flow relationship using the same method discussed in Chapter 3. Additional systems identification efforts beyond the scope of this project including frequency response methods which could be used to further increase the accuracy of the model.

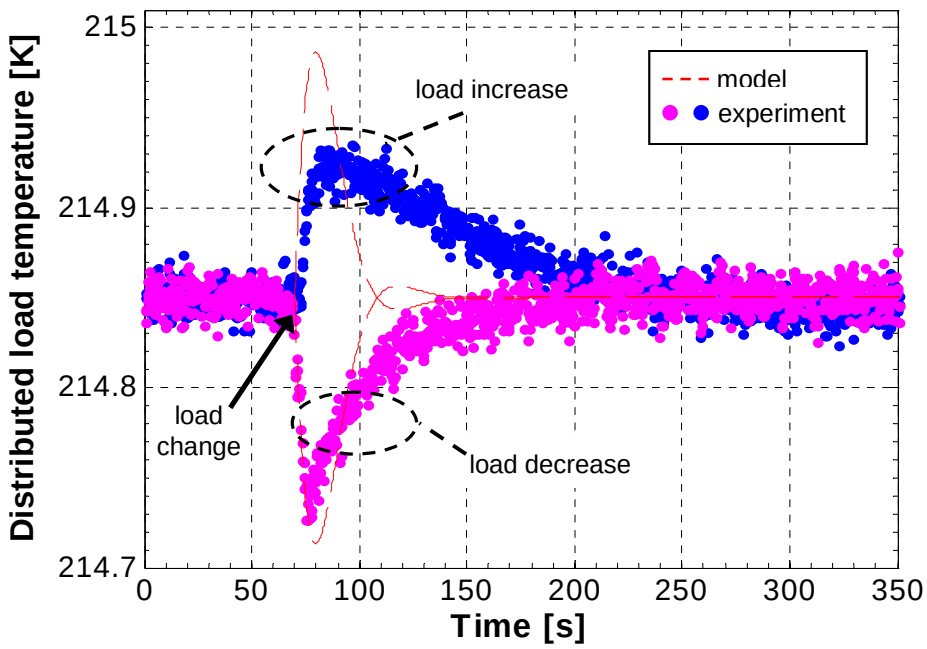

Figure 7-9: **Comparison of the predicted and measured interface temperature response to a 0.5 W step change in interface load.**

7.5 References

1. Lorenz, R.D, “Observers and State Filters in Drives and Power Electronics”, in the Journal of Electrical Engineering, Volume 2, Issue 2, 2002

8 Conclusions

8.1 Experimental Verification of Pulse Tube Rectified Interface Concept

The two primary purposes of this research were to demonstrate Pulse Tube Rectifying Interface (PT/RI) concept as a means to cool distributed loads and to investigate the use of the interface valve to provide additional temperature control. The transient responses with no control and with three different control algorithms were compared experimentally; the results are used to discuss the extension of distributed load management that is available by controlling the interface valve due to the reduction in the required controlled cooling capacity (Section 7.3). For this specific system, the amount of additional dynamic cooling capacity required for a desired interface control was reduced by a factor of 4 when the interface valve was used to regulate the interface temperature as opposed to the pulse tube compressor. The fundamental dynamic advantage associated with the valve is the ability to adjust the effective interface refrigeration by manipulating a low energy state which can be rapidly changed with minimal power (i.e. interface mass flow), rather than manipulating than the high energy state which requires significantly more power to adjust (i.e. cold head temperature). Additionally, the valve control extends the steady state operation map available with the PT/RI system.

The additional complexity associated with including the interface valve with the PT/RI system is not warranted for all distributed loading situations; when large temperature fluctuations are acceptable, the pulse tube refrigeration capacity is large relative to the distributed load fluctuations, and the distributed load is not expected to change significantly from a nominal operation point, then controlling the interface temperature using the pulse tube compressor is sufficient (i.e., a fixed orifice can be used to regulate the flow through the cooling loop). The

interface valve should be implemented if tighter temperature control is desired, a large envelope of distributed loads is expected, or the system has multiple distribution loops which require individual adjustment of refrigeration.

8.2 Controller Design Process

The controller development process discussed in this report is meant to be a guide for the development of control strategies for PT/RI systems. The following numbered list is a summary of the controller design process used in this research, which was ultimately used to determine the controller gains in a closed form solution. Note that many of these steps are not absolutely required but these steps provide a guidance relative to the important design considerations and at least one method of addressing these considerations. The design process assumes that: the cryocooler system incorporates the rectifying interface with the pulse tube, the system uses both pulse tube refrigeration and cooling loop mass flow control (controller 3 in chapter 7), the system uses Proportional-Integral (PI) control for both the interface and cold head, the pulse tube and interface valve have been sized correctly relative to the expected magnitude of the distributed load, and the nominal operating conditions such as pressures, temperature, cooling loop mass flow, and thermal capacities are known.

1. Perform steady and uncontrolled transient performance experimental tests similar to those shown in chapter 3.

2. Create a non-linear model using experimental data which captures steady state and transient behavior, as shown in chapter 4.

3. Create a linear model which captures the dominant relationships within the system, as shown in chapter 5, verify linear model through comparison with the complete, non-linear model.

4. Select a damping ratio that is appropriate for the interface; for example, a damping ratio of $1/\sqrt{2}$ generally yields a system that balances stability and performance (i.e., the maximum temperature fluctuation shown in Figure 6-4 (a).

5. Use the desired maximum temperature fluctuation to a step change in interface load and the damping ratio to calculate the required settling time as shown in Figure 6-4 (b).

6. Controller gains can be calculated in closed form using the settling time and damping ratio with the analog control model as shown in Chapter 6.2.1

7. Select the cold head damping ratio; a damping ratio of 0.9 was chosen for this experiment to ensure the stability of the cold head temperature.

8. Select the cold head settling time to be 10x greater than the interface settling time. This ensures eigenvalue separation and avoids the possibility of a resonance.

9. Calculate the cold head control gains using the cold head damping ratio and settling time, as shown in Chapter 6.2.2

10. The controller must compute the physical hardware change that is required to provide the desired refrigeration. For example, as shown in Figure 6-12, the interface refrigeration is adjusted via the cooling loop mass flow which is a function of the cooling loop valve rotational position and corresponding flow coefficient (C_v).

11. Create a digital model of the interface to study the effect of control loop sample rate on performance. Ensure that the analog model sufficiently predicts the digital implementation and that the control loop sample rate is well above the sample rate associated with instability.

12. Implement the control strategies in hardware, verify and tune system to achieve desired temperature control.

8.3 Future Recommendations

The PT/RI system tested here was relatively simple and primarily used to demonstrate the additional control available using the rectified interface system. It would be possible further extend the ability of the system to control interface temperatures using both software and hardware modifications.

1. The pulse tube refrigeration performance dependence on valve position could be decoupled to further regulate the cold head temperature. Figure 7-5 shows that the cold head temperature fluctuates 0.3 K for a 0.5 W step load with control algorithm 3 (Chapter 7 describes this controller). The cold head temperature fluctuation is partially related to the decrease in pulse tube refrigeration when the cooling loop mass flow is increased as shown in Chapter 3. If the pulse tube refrigeration was simultaneously increased when the cooling loop mass flow was increased (i.e. a feedforward command to the pulse tube compressor based on the empirical relationship pulse tube performance and interface mass flow), the cold head temperature fluctuation would decrease, subsequently providing better interface temperature control.

2. The interface valve control was limited by the noise in the interface temperature feedback signal. A cleaner signal could be achieved in hardware by better wire shielding, or in software using an observer [1] where the observer interface temperature is used as the interface feedback signal.

3. The range of dynamic distributed loads that could be managed by the PT/RI system, and the maximum temperature fluctuation performance of the system could be improved by using a parallel system of valves for each distributed loads which provides partitioned state feedback [2]. A large valve driven by the integral control signal (I in the PI controller) could be used to control the long term, steady mass flow changes which may be relatively large. A smaller valve driven by the proportional signal (P in the PI controller) would then be used to regulate the short term smaller mass flow changes. This cascaded system would have fine enough resolution to make rapid small mass flow adjustments which is useful at the beginning of a step response or for small changes in interface load. Additionally the system could provide large changes in mass flow which is used for the remainder of the step response and large changes in the steady distributed load magnitude.

4. Additional systems identification efforts could be used to tune the control system. Frequency response methods or ARMAX modeling [3] could be used to create a better model of the uncontrolled and controlled system behavior. These models would be used to make changes to the control algorithm to optimize the performance with a given set of hardware.

8.4 References

1. Lorenz, R.D, "Observers and State Filters in Drives and Power Electronics", in the Journal of Electrical Engineering, Volume 2, Issue 2, 2002
2. Lorenz, R.D., "Combining Drives of Differing Bandwidths to Meet Process Objectives", *Proceedings of the Controls Engineering Conf.*, May 23-25, 1989, Chicago.
3. Lennart, Ljung, "Systems Identification – Theory for the User", 2nd Ed, PTR Prentice Hall, Upper Saddle River, N.J., 1999

Appendix A – Mass Flow Data Point Omission

Chapter 3.7 mentions the omission of the mass flow data point for 80% stroke and ¼ open valve setting. A decrease in stroke reduces the pressure difference between the high and low pressure buffers and therefore should reduce the mass flow through the cooling loop. Additionally, a decrease in cooling loop valve opening should reduce the cooling loop mass flow. The mass flow data in for all stroke and valve settings follows this trend, except for the 80% stroke, ¼ open valve setting (with all data points the mass flow is 0.17 g/s). It was noted that the no-load data point for this particular control combination was taken on a different day than the rest of the data in the set and this measurement was a clear outlier relative to the load curve shown in Figure 3-10. When this no-load data point is excluded from the calculation, the mass flow calculated for the 80% stroke, ¼ open valve setting fits the expected trend for mass flow.

Figure A-1 and Table A-1 summarize the mass flow and parasitic load with the exclusion of the no load data point from the 80% stroke, ¼ open valve setting. The omission of the no-load operating point reduces the calculated mass flow rate from 0.17 g/s to 0.14 g/s, which follows the expected trend for a decrease in valve opening. For modeling purposes, the no-load data point is subsequently left out of the mass flow calculation.

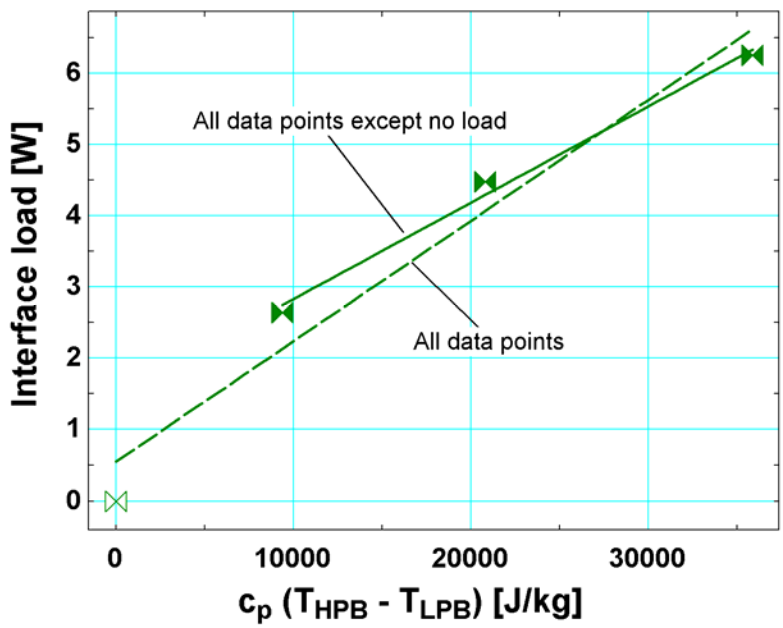

Figure A-1: **Load curve for 80% stroke, valve ¼ open highlighting the change of excluding the no load data point from the mass flow and parasitic load calculation.**

Table A-1: **Mass flow and parasitic load data for 80% stroke, ¼ open valve setting showing the difference when the no load data point is cut out.**

	Stroke	**Valve setting**	**Slope ($\dot{m}$)**	**Parasitic ($\dot{q}_p$)**
with no load data point	80%	¼ open	0.17 g/s	10.1 W
without no load data point	80%	¼ open	0.14 g/s	7.0 W

Appendix B - Matlab Script for Digital and Analog Simplified Linear Interface Model

```
%linear digital and analog thermal model for PT/RI system - interface

clc;
clear all;
close all;

%"""""""""""""""""""""""""""""""""""""""""""""""
% System parameters
%"""""""""""""""""""""""""""""""""""""""""""""""
kp = 1.64;              %[W/K] proportional gain
ki = 0.192;             %[W/K-s]integral gain
cp=5.2e3;               %[J/kg-K] helium specific heat
C_I=15;                 %[J/K]interface thermal mass
m_dot_0=0.145e-3;       %[kg/s]nominal mass flow
T_desired=0;            %[K] desired temperature fluctuation
zeta=(m_dot_0*cp+kp)/(2*sqrt(ki*C_I));          %damping ratio
T_settling=4*sqrt(ki*C_I)/(ki*zeta);            %[s] settling time
Ts = [0.01 0.3 10 12];                          %[s] sampling period vector
T_end = 100;                                    %[s] simulation total time

Tau_I = C_I/(m_dot_0*cp);                  %interface thermal time constant
a = 1/Tau_I;
q_I_mag = 1;                               %[W] interface load step magnitude


%"""""""""""""""""""""""""""""""""""""""""""""""
%Digital Model - begin
%"""""""""""""""""""""""""""""""""""""""""""""""

%create place holders for Temperature matrix
T_dr=zeros(T_end/Ts(1)+1,length(Ts));
%create place holders for Time matrix
time_dr = zeros(T_end/Ts(1)+1,length(Ts));


%"""""""""""""""""""""""""""""""""""""""""""""""
%create closed loop dynamics for varying sample time
%"""""""""""""""""""""""""""""""""""""""""""""""
for i=1:length(Ts)
    fs(i) = 1/Ts(i);                            %[Hz] sampling frequency
    time = 0:Ts(i):T_end;                       %simulation time space
    z=tf('z',Ts(i)); %makes expressions with "z" in them z-transfer functions
    step = ones(length(time),1);                %step heat input
    G_c = -(1/(1-z^(-1))*ki*Ts(i) + kp);        %Digital PI controller
    Gp1 = -1;

%2nd part of parsed model
    Gp2 = 1/(cp*m_dot_0)*(1-exp(-a*Ts(i)))/(z - exp(-a*Ts(i)));
```

```
    G_loop = G_c*Gp1*Gp2;                        %loop gain
    G_dr_cl = Gp2/(1+G_loop); %closed loop disturbance response
    %simulate a step heat input
[T_dr_1 time_dr_1]=lsim(q_I_mag*G_dr_cl,step);

    %insert temperature and time values into matrix
    for j=1:length(time)
        T_dr(j,i)=T_dr_1(j);
        time_dr(j,i)=time_dr_1(j);
    end
end

%Calculate effective refrigeration in Digital model
    for j=1:length(time)
           T_error(j,i)=T_dr(j,i)-T_desired;    %interface temperature error
           q_I_eff_p(j,i)=kp*T_error(j,i);      %proportional control
                if j==1
                    %integral control for first step
                    q_I_eff_I(j,i)=ki*Ts(i)*T_error(j,i);
                else
                    %integral control
                    q_I_eff_I(j,i)=q_I_eff_I(j-1,i) + ki*Ts(i)*T_error(j,i);
                end
            %total refrigeration - negate to make signs for control work
           q_I_eff_tot(j,i)=-(q_I_eff_I(j,i)+q_I_eff_p(j,i));
end

%"""""""""""""""""""""""""""""""""""""""""""""""
%Digital Model - end
%"""""""""""""""""""""""""""""""""""""""""""""""


%*************************************************************
%Analog model
%*************************************************************
time_a=0:0.1:T_end;                          %Analog time vector
step_a = ones(length(time_a),1);             %step heat input
s=tf('s'); %makes expressions with "s" in them continuous transfer functions
G_c_a=(kp + ki/s);                           %analog PI controller
Sys_a=1/C_I*1/(s + cp*m_dot_0/C_I);          %interface thermal system

G_loop_a=G_c_a*Sys_a;                        %controlled interface loop gain
G_dr_c_a=Sys_a/(1+G_loop_a);     %closed loop disturbance response transfer
function

[T_a time_a]=lsim(q_I_mag*G_dr_c_a,step_a,time_a); %simulates step heat input

%*************************************************************
%plots
%*************************************************************

figure(1) %disturbance response comparing analog and digital models
plot(time_a,T_a,'b.',time_dr(:,2),T_dr(:,2),'g+'),...
    axis([0 100 -0.05 0.3]),grid,...
    xlabel('Time [s]','FontSize',16,'FontWeight','bold'),...
```

```
    ylabel('Distributed load temperature
[K/W]','FontSize',16,'FontWeight','bold'),...
    set(gca,'FontSize',14,'XTick',[0:20:100],'YTick',[-0.1:0.1:0.3],...
              'XMinorTick','on','YMinorTick','on')

figure(2) %disturbance response using digital model - demonstrates unstable
control sample rate
plot(time_dr(:,2),T_dr(:,2),'g+',time_dr(:,3),T_dr(:,3),'r*',...
    time_dr(:,4),T_dr(:,4),'ko'),axis([0 100 -2 2]),grid,...
    xlabel('Time [s]','FontSize',16,'FontWeight','bold'),...
    ylabel('Distributed load temperature
[K/W]','FontSize',16,'FontWeight','bold'),...
    set(gca,'FontSize',14,'XTick',[0:20:100],'YTick',[-3:1:4],...
              'XMinorTick','on','YMinorTick','on')
```